# Synthesis, Characterization and Properties of Ti-Zr-Cu-Ni Based Metallic Glasses and Their Use as Filler Materials for Brazing Joints

A thesis

Submitted by

**P. Rama Rao**

*In partial fulfilment of the requirement for the award of the degree of*

**Doctor of Philosophy**

In

**Materials Engineering**

**School of Engineering Sciences and Technology**
**University of Hyderabad, INDIA.**
**2018**

**DEDICATED TO MY PARENTS AND TEACHERS**

# DECLARATION

I hereby declare that the work reported in this thesis is original and was carried out by me during my tenure as a PhD student at University of Hyderabad, India. This thesis has not formed the basis for the award of any degree, diploma, Associateship, membership or similar title of any university or institution.

P. Rama Rao
Reg. No.: 09MMET03
School of Engineering Sciences and Technology
University of Hyderabad


# CERTIFICATE FROM THE SUPERVISORS

This is to certify that the thesis work entitled **"Synthesis, Characterization and Properties of Ti-Zr-Cu-Ni Based Metallic Glasses and Their Use as Filler Materials for Brazing Joints"** submitted by Rama Rao Panugothu under our supervision has been carried out at the University of Hyderabad, Hyderabad, India, and this has not been submitted for any degree or diploma at this or any other University.

**Dr. Koteswararao V Rajulapati**
Associate Professor
School of Engineering Sciences and Technology,
University of Hyderabad, India.

**Prof. A. K. Bhatnagar**
School of Engineering Sciences and Technology,
University of Hyderabad, India.

**Approved by**

**Prof. M. Ghanashyam Krishna**
Dean,
School of Engineering Sciences and Technology,
University of Hyderabad, India.


# CERTIFICATE

This is to certify that the thesis entitled **Synthesis, Characterization and Properties of Ti Zr-Cu-Ni Based Metallic Glasses and Their Use as Filler Materials for Brazing Joints** submitted by **P. Rama Rao** bearing registration number **09ETMM03** in partial fulfilment of the requirements for award of **Doctor of Philosophy** in the **School of Engineering Sciences and Technology** is a bonafide work carried out by him under our supervision and guidance.

This thesis is free from plagiarism and has not been submitted previously in part or in full to this or any other University or Institution for award of any degree or diploma.

Parts of this thesis have been:

**A. Published in the following publications:**

1. Material Research Express 5 (2018) 065205

**B. Presented in the following conferences:**

1. EMSI, 2016 (International)
2. EMSI, 2017 (International)
3. MRSI, 2017 (International)
4. SICE-DMRL, 2018 (International)

Further, the student has passed the following courses towards fulfillment of coursework requirement for PhD and was exempted from doing coursework (recommended by Doctoral Committee) on the basis of the following courses passed during his M.Tech program and the M.Tech degree was awarded:

| Course | Course Name | Credits | Pass/Fail |
|---|---|---|---|
| MT703 | Thermodynamics of Materials | 4 | Pass |
| MT710 | Concepts of Materials Science | 4 | Pass |
| MT715 | Characterization of Materials | 4 | Pass |
| MT720 | Synthesis and processing of Advanced | 4 | Pass |
| MT724 | Seminar | 2 | Pass |
| MT730 | Design and Selection of Engineering Materials | 4 | Pass |
| MT735 | Materials processing & Characterization Laboratory | 4 | Pass |
| MT725 | Diffusion and Kinetics | 4 | Pass |
| MT726 | Modelling and Simulation in Materials Engineering | 4 | Pass |
| MT727 | Materials Processing & Characterization Lab - II | 4 | Pass |
| MT728 | Nano Materials and Technologies | 4 | Pass |
| MT729 | Surface Engineering | 2 | Pass |
| MT730 | Nuclear Materials | 4 | Pass |
| MT731 | Ceramic: Science and Technology | 4 | Pass |
| MT732 | Seminar | 2 | Pass |
| MT780 | Dissertation | 18 | Pass |
| MT801 | Research Methodology | 4 | Pass |

**(Supervisor)** **(Co-Supervisor)** **(Dean of School)**

# Acknowledgements

It has been a wonderful journey of in my life with lot of surprise and pleasure. This Ph.D tenure not only taught me science through various experiments but also provided me an opportunity to learn. It provided me an essence of research and life through various concepts and interesting people. So it is my duty to thank each and every one, who is influences in this pivotal period of my life.

At the onset, I express my sincere thanks to my supervisor, Prof. A. K.Bhatnagar, National Academy of Sciences', India (Allahabad) Senior Scientist Platinum jubilee Fellow, University of Hyderabad, Hyderabad for giving me the opportunity to work on the present problem and for his invaluable guidance. I would like to thank him particularly for giving me the freedom to explore the areas that excited me most.

The constant enthusiasm and leadership of Prof. A. K.Bhatnagar not only provided almost an infinite source of encouragements every morning during the entire period of my work but also kept me moving in the most stressful times. He always acted as a philosopher and friend besides providing the scientific guidance.

I also would like to record my gratitude to Dr. Koteswararao for supervising my work at SEST and assisting me when I was in need. I would not have been able to finish this project without his help. I am also very thankful to all other faculties in SEST department. In particular I would like to record my gratitude to Dr. Dibakar Das and Dr. Bhaskar Majumdar for their constant encouragement and support during my doctoral report and coursework. I am thankful for the advice and guidance of Prof. Ghanashyam Krishna, Dean and to Prof. K. Bhanu Sankara Rao (Former Dean), SEST.

I also would like to record my gratitude to Dr. Bhaskar Majumdar for supervising my work at DRDO-DMRL, Hyderabad and assisting me when I was in need. I would not have been able to finish this project without his help. I am also grateful to him for making me aware about the potential application of brazing studies and mechanical characterization that was totally unknown to me, and for providing me a wonderful opportunity for independent, He took a lot of pain and spent patiently a lot of his valuable time in teaching me all the related subject matters and instrumental details. I am also really thankful to him for the scientific inputs and guidance from the ceramic subject areas.

I express my deep sense of gratitude to Dr. K. Muraleedharan (Director, CSIR-CGCRI) for allowing me to pursue my PhD work for his constant support. Though his idea and approach towards problems have been phenomenal, who helped me to understand concepts in TEM.

I am also very thankful to Director of DMRL-RDRO and scientist in the department of AMG. Also very thankful to A.V. Phani Kiran and Richard Danny for their helping to made the alloys and melt-spun ribbons.

I would like to record my gratitude to Dr. Sandip Bysakh, Principal Scientist, CSIR-CGCRI, Kolkata. For his constant help in Electron microscopy studies and discussing on brazing related topic. His positive critic on my research problem helped me to grow as a researcher and stimulated me to learn new concepts in science.

I would like to thank Prof. Dr. Asit Baran Mandal. FASc, FRSC (U.K), FNAE, FSAB (Hony), INAE Distinguished Professor, for all his help to correction of my thesis. CSIR - Central Glass and Ceramic Research Institute**,** Kolkata**.**

I thank all research scholars from School of Physics. I would like to thank my colleagues (Dr. Raj Kumar, Dr. Senthel, Chandrasekhar, Mohan, Harish and Ramya) and friends in the neighboring research lab (Dr. Ramakanth and Dr.Tirupati) Medam Bapuji, Praveen Kumar, Raj Kumar, Venkata Sai and to all other friends whom i have met in my PhD carrier.

Finally, I'd like to thank my family. My parents introduced me to science and have always encouraged me. I'm very grateful for all their love, support, and interest in my work.

I heartily acknowledge the financial supports (UGC-JRF) sponsored by UGC, India. Without these deep supports it would not have been possible at all to complete this thesis work.

**P. Rama Rao**

## LIST OF PUBLICATIONS

1. **P. Rama Rao**, Anil K. Bhatnagar, Bhaskar Majumdar and K. Muraleedharan, "Structural Properties of brazed Ti-joint using $Ti_{20}Zr_{20}Cu_{40}Ni_{20}$ metallic glass ribbon as filler", **Material Research Express 5** (2018) 065205.
2. **P. Rama Rao,** Anil. K. Bhatnagar, and Bhaskar Majumdar "Microstructural characterization of brazed Ti joint using $Ti_{20}Zr_{20}Cu_{50}Ni_{10}$ metallic glass ribbon as filler", **Journal of Engineering Physics**, 2(2018) 6-10.
3. **P. Rama Rao**, Anil K. Bhatnagar and Bhaskar Majumdar "Thermal Stability of $Ti_{20}Zr_{20}Cu_{10}Ni_{50}$ Metallic Glass" **International Journal of Recent Scientific Research**. 9(2018) 24301-24304.
4. **P. Rama Rao**, Anil K. Bhatnagar, B. Majumdar, K. Muraleedharan, "Microstructural evolution of brazed Ti joint using $Ti_{20}Zr_{20}Cu_{50}Ni_{10}$ metallic glass ribbon as filler"**. Elsevier Open Access Journal i.e. " Procedia Structural Integrity",** (2018).
5. **P. Rama Rao**, Anil K. Bhatnagar and Bhaskar Majumdar, "Crystallization and kinetics of Ti-Zr-Cu-Ni Based Metallic Glasses", in **Bulletin of materials science,** (2018) under review.
6. **P. Rama Rao**, A.K. Bhatnagar and Bhaskar Majumdar "Mechanical Properties of Ti-alloy joint with $Ti_{20}Zr_{20}Cu_{60-x}Ni_x$ (x = 10, 20, 30, 40 and 50) filler metal", (**Journal of materials science**), (2018) under review. .
7. **P. Rama Rao**, Anil K. Bhatnagar and Bhaskar Majumdar, "Brazing studies of Ti- joint using $Ti_{20}Zr_{20}Cu_{60-x}Ni_x$ (x = 30, 40, and 50) metallic glass ribbon as filler metal", **in** (**Bulletin of materials science**), (2018) under review.
8. **P. Rama Rao** and A. K. Bhatnagar, "Thermal Stability of Three Ni-based Metallic Glasses", in **Journal of Transactions of the Indian Ceramic Society, Taylor & Francis** (2018) under review.

1. **P. Rama Rao**, Anil K. Bhatnagar and Bhaskar Majumdar, "Study of Kinetics and Crystallization of $Ti_{20}Zr_{20}Cu_{50}Ni_{10}$ Metallic Glass", (2018); **AIP Conf. Proc.** 1953, 090007-1-090007-5.
2. **P. Rama Rao,** A. K. Bhatnagar, Ravinder Reddy K. and Venkateswara Rao M. "Thermal Stability and other properties of Ni-Cr based Metallic glasses", 55$^{th}$ DAE Solid State physics Symposium 2010. **AIP Conf. Proc.** 1349, 553-554 (2011).

**CONFERENCE/WORKSHOP/PRESENTED/ATTENDED**

**1.** P. Rama Rao, Anil K. Bhatnagar, Bhaskar Majumdar, K. Muraleedharan, "Microstructural evolution of brazed Ti joint using $Ti_{20}Zr_{20}Cu_{50}Ni_{10}$ metallic glass ribbon as filler". **Oral presentation** " Procedia Structural Integrity" at DMRL (Hyderabad) and Indian Structural Integrity Society (In SIS) are pleased to convene the Second International Conference on Structural Integrity and Exhibition (SICE) on 25-27 July, 2018 India.

**2.** **P. Rama Rao**, Anil K. Bhatnagar, B. Majumdar, K. Muraleedharan, and S. Bysakh, "Microstructural characterization of brazed Ti-joint using $Ti_{20}Zr_{20}Cu_{50}Ni_{10}$ metallic glass ribbon as filler", the **Young Scientists Colloquium** 2017 (YSC 2017) Materials Research Society of India (MRSI) - Kolkata Chapter &Indian Institute of Engineering Science and Technology IIEST, Shibpur, Kolkata, India.

**3.** **P. Rama Rao**, Anil K. Bhatnagar and Bhaskar Majumdar "Thermal Stability of $Ti_{20}Zr_{20}Cu_{10}Ni_{50}$ Metallic Glass" poster presented in 62$^{nd}$ DAE Solid State Physics Symposium to be held at DAE Convention Centre, Bhabha Atomic Research Centre, Mumbai between 26$^{th}$ -30$^{th}$ December, 2017 India.

4. **P. Rama Rao**, Anil K. Bhatnagar and Bhaskar Majumdar "Study of Kinetics and Crystallization of $Ti_{20}Zr_{20}Cu_{50}Ni_{10}$ Metallic Glass" poster presented in 2nd International Conference on Condensed Matter & Applied Physics (ICC 2017) will be held at Govt. Engineering College, Bikaner, and Rajasthan during November 24-25, 2017.
5. **P. Rama Rao**, Anil K. Bhatnagar, B. Majumdar, K. Muraleedharan, and S. Bysakh, "Microstructural characterization of brazed Ti-joint using $Ti_{20}Zr_{20}Cu_{50}Ni_{10}$ metallic glass ribbon as filler", **Invited Talk** in International Conference on Electron Microscopy Society of India (EMSI) jointly organized by Indira Gandhi Centre for Atomic Research, Kalpakkam and the Indian Institute of Technology Madras, during July 17-19, 2017 at Chennai.
6. **P. Rama Rao**, Anil K. Bhatnagar, B. Majumdar, K. Muraleedharan, and Sandeep Bysakh,"Characterization of $Ti_{20}Zr_{20}Cu_{10}Ni_{50}$ metallic glass as a brazing filler for Titanium joints", presented in International Conference on Electron Microscopy Society of India (EMSI) jointly organized by Department of Metallurgical Engineering during June 2-4, 2016 at Varanasi.
7. **P. Rama Rao**, Anil. K. Bhatnagar "Thermal Stability and other properties of Ni-Cr based Metallic glasses", presented in 55th DAE Solid State Physics Symposium", Organized by Bhabha Atomic Research Centre & Manipal University, Karnataka, December 26th -30th, 2010.
8. **P. Rama Rao** and Anil. K. Bhatnagar "Thermal Stability and other properties of Ni-Cr based Metallic glasses", poster presented in 55th DAE Solid State Physics Symposium", Organized by Bhabha Atomic Research Centre & Manipal University, Karnataka, December 26th -30th, 2010.

9. **Attended** Indian Institute of Metals, Kolakata Chapter International Seminar on "Advances in Metal and Mineral Processing Industries of India in National Policy Perspective" Hotel Taj Bengal, Kolkata December 15, 2017.
10. **Attended** "International Pre-Conference and workshop on Electron Microscopy", organized by Department of Metallurgical Engineering (IIT-BHU) workshop on 30$^{th}$ May-1$^{st}$ June, 2016 at Varanasi.
11. **Attended** "Advanced Tools for Nanoscopic Materials Characterization" at S.N. Bose National Centre for Basic Sciences, Kolkata, during 5-6$^{th}$ Nov 2015. Skills related knowledge was imparted by various expertises' of the respective fields.
12. **Attended** "Indo-UK Joint seminar on Functional and Energy Materials, Manufacturing & Structures", Organized by University of Hyderabad, 25-26$^{th}$ March, 2013.
13. **Attended** "Frontiers in Physics (FIP-2013)" September-30, 2013, held at University of Hyderabad, Hyderabad.
14. **Attended** "National Conference on New Materials & Processes for Improving Quality of Infrastructure''(NEMPIQI-2012), October19-20$^{th}$, 2012, held at University of Hyderabad, Hyderabad.
15. **Attended** "Indian-Singapore Joint Physics Symposium, Organized by School of Physics'' held at University of Hyderabad, Hyderabad, February19-21$^{st}$, 2010.

# Contents

# List of Figures

## Chapter 1



## Chapter 2



## Chapter 3

## Chapter 4



## Chapter 5

## Chapter 6

# List of Tables

## Chapter 1



## Chapter 2



## Chapter 3

## Chapter 4



## Chapter 5

## Chapter 6

# Abstract

Development of brazing materials for joining titanium based alloy is a current topic of interest due to the expanding use of these alloys in aerospace, chemical apparatuses, heat exchangers etc. The Ti based brazing alloys as filler materials are generally brittle and are used in the form of powders, pastes, sprays which will be spread prior to the joining operation. This may lead to porous joint because of the entrapped air in the powder. The main problem in the brazing of titanium is the formation of brittle intermetallic compounds between titanium and filler metal elements at the base metal-filler metal interface resulting in brittle joints and high galvanic corrosion. The above problem can be overcome by using amorphous titanium-zirconium-based alloys in the form of ribbons produced through melt spinning technique. They possess several advantages over the conventional crystalline filler materials such as better diffusivity of elements in amorphous state, good ductility, compositional homogeneity, accelerated interfacial reaction by improving wetting conditions etc. Therefore, the usage of fluxes (which modify the wetting properties) can be avoided and cleaner joints can be achieved.

Amorphous alloys/metallic glasses have attracted considerable interest during the past few decades because of their unique combination of properties and also fundamental research interest. Glass formation is favored in multicomponent alloy systems consisting of at least three components with difference in atomic size above 12% and very high negative enthalpy of mixing among the constituent elements. The compositions of the alloys are chosen in such a way that the high solid/liquid interfacial energy and viscosity of liquid alloys suppress the nucleation and growth of crystalline phase resulting in the formation of amorphous phase. The driving force for the formation of the non-equilibrium structure in these multicomponent alloys through solidification technique is the undercooling of the melt below equilibrium

transition temperature. The liquid is undercooled when the kinetic constraints suppress the nucleation and growth of the stable phases. Ultimately, in some alloy systems exhibiting deep eutectic in equilibrium phase diagram, the sufficiently undercooled melts retain the liquid structure below the glass transition temperature (Tg) and are transformed into amorphous phase.

The amorphous brazing ribbons as filler materials are produced by rapid solidification technique such as planar flow melt spinning by which thin, wide and continuous quality amorphous ribbons can be produced in one step directly from the melt. They also possess superior chemical and microstructural homogeneity during brazing. Amorphous brazing filler helps in accelerating the atomic diffusion in high-temperature brazing processes and therefore, the temperature required to achieve a good bonding can potentially be lowered. This results in reducing the residual stresses in the joints and thereby increasing the joints strength.

Another challenge in titanium brazing technology is to develop low-temperature fillers materials with brazing temperatures less than the α-β transformation temperature to preserve the original microstructure and mechanical properties of the base metal. Zr based alloys provide a good compatibility with Ti base metal because the Zr is completely miscible with Ti in both liquid and solid phases. Amorphous forming ability of the alloys is significantly enhanced by the simultaneous addition of Ni and Cu elements, which act as melting point depressants. It is known that Cu and Ni are located in the same family in the periodic table with infinite mutual solubility; the same is valid for the case of Ti and Zr. The presence of Ni and Cu converts Ti-Zr system into eutectic alloys having (Ti,Zr)x(Cu,Ni)y intermetallic phases. This leads to induce high brittleness in the alloy and limits the processibility by producing through conventional melting–ingot-casting-deformation technology route. Initial usage of these materials was carried out by a clad strip consisting of separate metallic layers

of Ti, Zr, Ni, and Cu. Such strips structures seriously impairs brazability and quality of joints. Hence usage of novel techniques such as planar flow melt spinning techniques is preferred. This technique has the dual advantage of rapid solidification and its ability to produce the ribbons directly from the melt. This saves the laborious process involved in the conventional processes such as rolling. Also the ribbons are ideal in thickness and are near-net shaped for brazing applications.

To date, the data available on the properties of joints obtained with these advanced filler metals are still limited. Hence development of new brazing alloy with higher glass forming ability, strength and low melting temperature is a challenging task to reduce the distortion in the microstructure of the base metal and joint. It can be observed from the literature that glass forming ability of Ti-Zr-Cu-Ni systems have not been explored extensively. Effect of different alloying elements has also not been studied in details. Moreover, limited information is available on the mechanical behavior with respect to the composition variation.

The PhD research work aims at understanding the glass forming ability (GFA) of $(Ti_{0.5}Zr_{0.5})_{40}(Cu_xNi\ (1\text{-}x)_{60}$ systems and the evolution of structures during rapid solidification. Attempts will be made to braze Ti metal using the ribbon and evaluate the brazability of the ribbons. Initially, calculations will be carried out to evaluate the theoretical GFA of Ti-Zr-Cu-Ni based metallic glass alloy. Alloys with nominal compositions $(Ti_{0.5}Zr_{0.5})_{40}(Cu_x\ Ni\ (1\text{-}x)_{60,}$ where x 0.1, 0.2, 0.3, 0.4 and 0.5 will be prepared from the mixture of pure elements in a vacuum arc melting furnace. All these alloys will then be rapidly solidified using vacuum planar flow melt spinning process for obtaining wide and continuous amorphous ribbons. Subsequently, structures and morphological characterizations will be carried out using XRD, SEM and TEM.

Detailed thermal stability, undercooled liquid regime of amorphous phase and kinetics of

crystallization will be studied using DSC/DTA. Fixture will be designed for brazing experiments. Two Ti plates will be brazed by inserting the rapidly solidified ribbons as filler materials using vacuum furnace varying different process parameters such as braze temperature and time of holding. Detailed cross sectional microscopic analyses will be carried out to evaluate extend of diffusion of all elements within the joints. Finally the mechanical properties will be evaluated and correlated with the composition of the brazing alloy.

# Chapter 1 Introduction and Literature Review

The research work presented in this thesis is on Ti-Zr-Ni-Cu metallic glasses and their use in brazing of titanium joints. Therefore, this chapter gives an introduction to metallic glasses, some of their relevant properties and certain aspects of brazing of metallic joints. Metallic glasses have become important industrial materials. Histories of metallic glasses along with some recent developments are given and their various applications and the relevant technologies are also included.

## 1. The Present Study of Thesis

In the present investigation, the Ti-Cu joints were brazed using a $Ti_{20}Zr_{20}Cu_{60-x}Ni_x$ (x= 10,20,30,40 and 50) (at. %) alloy as a filler and characterized them. In the first place, the microstructural evolution of the joints was comprehensively investigated in view of the formation behaviour of the produced intermetallic and the time dependent interfacial reactions during brazing process. Furthermore, in order to clarify the relations between the microstructure and joint performance, the tensile strength of the brazed joints was studied.

The question of the need of the present study is from the academic stand point where the continued development of the so-called high technology industries with a view to understand the material characteristics and their utility to improve our life style. The material properties of any solid can be best understood with the understanding of its atomic structure. The X-ray or neutron diffraction measurements can give detailed information of the atomic structure in crystalline materials. In order to obtain adequate information, the additional structural may be needed. The metallic glasses or amorphous metals are the important class of materials where the diffraction experiments give incomplete information on the atomic structure. The investigation of the glass forming

ability (GFA) of $(Ti_{0.5}Zr_{0.5})_{40}$ $(Cu_xNi\ (1\text{-}x)\ _{60}$ systems and the evolution of structures during rapid solidification, attempts will be made to braze Ti metal using the ribbon and evaluate the brazability of the ribbons. Initially, calculations will be carried out to evaluate the theoretical GFA of Ti-Zr-Cu-Ni based metallic glass alloy. To date, the data available on the properties of joints obtained with these advanced filler metals are still limited. Hence, development of new brazing alloy with higher glass forming ability, strength and low melting temperature is a challenging task to reduce the distortion in the microstructure of the base metal and joint. It can be observed from the literature that glass forming ability of Ti-Zr-Cu-Ni systems have not been explored extensively. Effect of different alloying elements has also not been studied in details. Moreover, limited information is available on the mechanical behaviour with respect to the composition variation. Development of brazing materials for joining titanium based alloy is a current topic of interest due to the expanding use of these alloys in aerospace, chemical apparatuses, heat exchangers, etc. The Ti based brazing alloys as filler materials are generally brittle and used in the form of powders, pastes, sprays, which will be spread prior to the joining operation. This may lead to porous joint because of the entrapped air in the powder. The main problem in the brazing of titanium is the formation of brittle intermetallic compounds between titanium and filler metal elements at the base metal-filler metal interface resulting in brittle joints and high galvanic corrosion. The above problem can be overcome by using amorphous titanium-zirconium-based alloys in the form of ribbons produced through melt spinning technique. They possess several advantages over the conventional crystalline filler materials such as better diffusivity of elements in amorphous state, good ductility, compositional homogeneity, accelerated interfacial reaction by improving wetting conditions, etc. Therefore, the usage of fluxes (which modify the wetting properties)

can be avoided and cleaner joints can be achieved. The thesis is divided into following seven chapters:

## 1.2. Metallic Glasses

### 1.2.1 The metallic glasses and disordered materials

The elemental metals are normally crystalline solids exhibiting long range atomic order and form a stable state. Crystalline solids are characterized by periodic lattice in which arrays of atoms or molecules are aligned in a periodic manner so that their positions and orientations have perfect translational symmetry [1]. On the other hand disordered solids are the solids exhibiting large departures from this kind of orderly arrangement of atoms/molecules.

A perfect disordered solid will be the one in which atoms/molecules are totally randomly arranged which is usually termed as an "amorphous solid" [2-5]. One can also have highly disordered solids which may have some short range order in atomic arrangements like the one which exists in liquids. An extremely disordered solid, produced by a rapid quenching technique of a melt, does have such a short range order and is normally called "glass". A glass does not exhibit the long-range periodicity of atomic arrangements found in crystalline materials hence it is 'amorphous' in that sense but, as said before, it may have frozen liquid-like atomic structure that is, the correlation between the positions of the atoms gets completely lost over distances of more than about 3-5 atomic spacing's. While insulating glasses (e.g., window glasses) have been known since historic times, whereas, semi-conducting glasses and metallic glasses have been produced only during the last century. Extensive studies on the various types of glasses also started seriously in the last century after the work of many scientists like Mott [2, 7], Anderson [8] and others [9]. They showed that a highly disordered arrangement of atoms in a solid leads to different interesting physical behaviour which needs to be studied and exploited for practical applications.

In order to freeze liquid like structure while the solidification process is taking place, it is necessary that the quenching rate must be high enough to arrest the atomic movement in a melt/liquid suddenly and restrict nucleation and growth of micro-crystallites [4-6]. Oxide and semiconducting glasses are not difficult to produce as the quenching rate of the melt in question need not be very high in most cases. In general, most glasses are prepared by quenching a melt of mixtures of compounds which are predominately covalent in nature like for example window glass, which is a mixture of various oxides, and semiconducting glasses like Se, Se-As, Si-Te-Ge etc.

As mentioned above, it is possible to produce solids under special circumstances in a so called amorphous or glassy state in which atoms are randomly arranged and, therefore do not exhibit crystalline long range atomic order. The glassy state is usually obtained by rapid quenching of a liquid therefore; the short-range order of liquid gets frozen, as mentioned before. The amorphous or glassy state is a metastable state which can be transformed into the crystalline state if given enough energy by way of heat or some other form.

In general, many metallic alloys can be synthesized in a glassy state when cooled at rapid rate of ~$10^6$ K/sec. Upon rapid solidification of a liquid metallic melt at such a high cooling rate suppresses formation of crystalline phases by inhibiting nucleation and growth of crystallites which results in production of a metallic glass. The first Au-Si based metallic glass was synthesized in 1960 at Cal Tech [2] by rapid quenching of the melt. Since then, a number of metallic alloys have been synthesized in the glassy form and the process to obtain new metallic glasses continues due to their scientific interest and applicability in various spheres. Owing to their metallic and amorphous/glassy structure, these glassy materials have some good, chemical, physical and mechanical properties [3-6]. Many of these glasses exhibit high hardness, high

magnetism, high fracture and tensile strengths, resistance to corrosion and good ductility depending on their constituent elements [3-6]. Because of their novel properties, the interest of researchers in metallic glasses continues extensively.

### 1.2.2 The Processing Challenges for Metallic Glass Synthesis

On the other hand, it is very difficult to produce pure metals having amorphous or glassy structure. In 1940-50s amorphous metals were produced in thin film form when the substrate was cooled to liquid helium temperatures (< 10 K) or in some cases to liquid nitrogen temperatures (< 80 K). Glover [10] showed that Bi can be produced in amorphous form when its thin film is deposited on a substrate kept at liquid helium temperatures. Bi is not a superconducting material in bulk form but amorphous Bi film turned out to be superconducting, thus confirming that the disorder can produce large property changes. Further, it also showed that one requires really very high quenching rates to produce a metal in amorphous form. A rough estimate gives the quenching rate to be ~$10^6$K/s. As mentioned before, higher covalence leads to glass formation easier. Thus, if one has a mixture of materials which is metallic and covalent, one may expect the quenching rate to go lower. Therefore, depending on the mixture of materials, one may be able to produce amorphous or glassy metallic solids if quenching rates are of the order of ~$10^4$ to $10^6$ K/sec. Thus, this was possibly why until 1960, metallic glasses could not be prepared which would be stable at room temperature and above.

### 1.2.3 The Journey of Metallic Glasses Really Begins

In 1960, Klement, Willens and Duwez [11] discovered that a melt of an alloy of gold and silicon ($Au_{80}Si_{20}$) when rapidly quenched at a rate of ~ $10^6$ K/sec turned out to be amorphous (showed no crystallinity and X-ray diffraction showed no peaks) and was stable at room temperature. In this alloy, Si provided the needed covalent bonding. Since this discovery, intense research programmes in the field of metallic glasses have

resulted in vast number of publications, understanding of underlying disordered metallic behaviour and resulting in practical applications. Devices, based on metallic glasses, are already in market. In the last two decades or so several books, review articles and conference proceedings have been published in this vast area of research. A list of some of these is given in [12-13], which obviously is not an exhaustive one.

### 1.2.4 Early Industrial Initiative

Inoue and his co-workers have investigated rare-earth materials of Al and ferrous during late 1980s. They found exceptional glass-forming ability in La-Al-Ni and La-Al-Cu alloys [14] upon rapid solidification. Upon casting even up to 9 mm thick $La_{55}Al_{25}$ $Ni_{20}$ (later $La_{55}Al_{25}Ni_{10}Cu_{10}$) into Cu mold, cylindrical samples with diameters up to 5 mm or similar thicknesses sheets were made fully glassy. Inoue et.al [15], have also developed glassy Mg-Cu-Y and Mg-Ni-Y alloys with largest glass-forming ability in $Mg_{65}Cu_{25}Y_{10}$ in 1991. The group Inoue [16] developed a family of Zr-based Zr-Al-Ni-Cu alloys with high glass forming ability and thermal stability at the same time. For the alloy $Zr_{65}$ $Al_{7.5}$ $Ni_{10}$ $Cu_{17.5}$, the critical casting thickness ranged up to 15 mm and super cooled liquid region was extended to 127 K. It has been clearly demonstrated that the development of these alloys in bulk metallic glass compositions were not merely a laboratory curiosity, however quite interesting for applications in engineering.

### 1.2.5 The genesis and journey of vitreloy-1

Johnson and others have recognized quickly the significance of Inoue's work [16], in early 1990. Peker and Johnson have developed [17], quinary alloy $Zr_{41.2}Ti_{13.8}Cu_{12.5}Ni_{10}Be_{22.5}$ (called as Vitreloy 1(Vit 1)) in 1993. The critical casting thickness of several centimetres was archived in this work and this work together with the work of Inoue group [16] can be taken as the starting material for the use of bulk glassy materials in structural applications. The properties of the alloy Vit 1 were

investigated thoroughly in the next 10 years. After replacing 30% Ni by Cu, Inoue group re-visited the$Pd_{40}Ni_{40}P_{20}$ alloy in 1997. They have developed an alloy with a critical casting thickness of as high as ~ 72 mm [18].

### 1.2.6 The development of casting thickness of Metallic Glasses with time: Towards the Future

It is well known to date that the Pd-Cu-Ni-P family possesses the metallic system with the highest glass-forming ability. The critical casting thickness as a function of the year the corresponding alloy was developed is shown in Figure 1.1.The critical casting thickness increased by more than three orders of magnitude in the last 40 years. After showing a fit to the data, it tends to increase by one order of magnitude every 12 years (approx.).According to Moores's law, if such a trend is true; the bulk metallic glass compositions may be obtained in the next 10 to 20 years that are similar to oxide glasses, difficult to crystallize. The research in the area of bulk metallic glasses is growing enormously recently. Attempts have been made for searching new alloy compositions by many researchers to investigate the mechanical, structural, thermo-physical and magnetic properties of the above mentioned alloys.

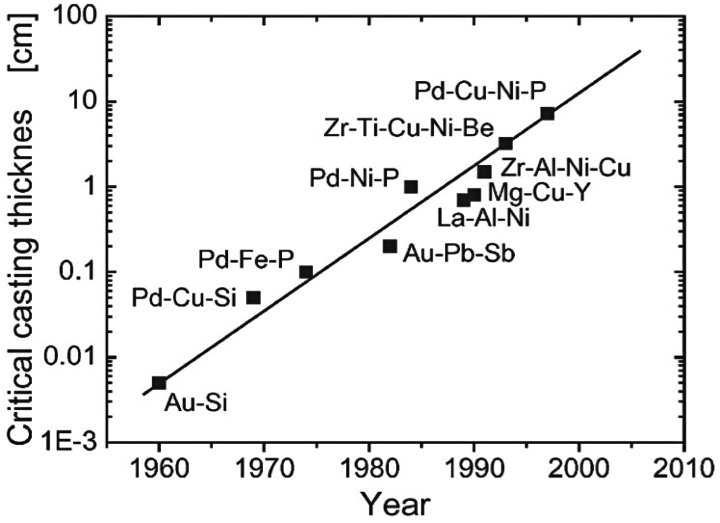


Fig.1.1The critical casting thickness for glass formation was shown as function of the year [19].

### 1.2.7 Global Scientific Interest about BMGs on the Surge

Regarding metallic glasses, it has been reported recently [20-23].DARPA of USA has taken initiative in launching "scaling-up" bulk metallic glass, which is useful for engineering applications. They are more or less similar to the projects exist in Japan and Europe viz., Inoue super-cooled Liquid Glass and European Network on Bulk Metallic glass, etc. The bulk metallic glass products manufactured by the Liquid Metal Technology for sporting goods, electronic product cases including cell phones, high performance springs and medical devices [24]. In near future; we can expect further major applications of bulk metallic glasses based on the present developments.

### 1.2.8 The earlier development of Ti-Based Alloys

Initially, the Ti-based metallic glasses had been developed extensively for their potential as high specific strength materials and subsequently for their ability to carry plastic deformation. The $Ti_{50}Ni_{40}Be_{10}$ had the highest specific strength among metallic glasses with yield strength of 2261MPa and a density of 4.13g/cm$^3$, reported earlier [25]. The development of $Ti_{40}Ni_{40}Si_{20}$ in 1978 represented one of the hardness metallic glasses produced with a Vickers hardness of 1070.However, similar to Fe-based glasses, producing bulk Ti-based glasses requires the use of at least three solute alloying components. The GFA of selected Ti-based alloys is shown in Table 1.1. Through the use of either Zr or Be, the $D_{max}$, of Ti-based metals has been substantially increased up to 8mm.The development of bulk Ti-based glasses has unlocked their potential as both strong and ductile alloys, for example, $Ti_{40}Zr_{25}Ni_9Cu_9Be_{18}$ [26], which contains a $D_{max}$ of 8mm, exhibits a plastic elongation of 4% under quasi-static compression. This is in striking contrast to the majority of metallic glasses, which generally exhibit no observable plastic deformation. The specific cause for this increase in ductility has not yet been fully explained. However, increased ductility has been

linked to the development of icosahedra-type short range order as seen in HRTEM images [27]. The high yield strength, enhanced ductility and sufficiently large critical thickness made the Ti-based glasses materials the good candidate for the application in high specific strength materials. A compilation of all Ti-based glasses showing ductile compressive behavior is shown in Figure 1.1. With the exception of $Ti_{40}Zr_{10}Cu_{36}Pd_{14}$, plastic elongation is at least 4%. Ti-based glasses have also been developed as a potential biomedical material due to the combination of a low elastic modulus (more comparable to bone than current crystalline Ti alloy implants), their increased strength, and their corrosion resistance. However, the toxic elements Ni and Be must be removed, such as in the $Ti_{40}Zr_{10}Cu_{36}Pd_{14}$ alloy [28]. A list of the mechanical properties for selected Ti-based glasses is given in Table 1.1. While all Ti-based glasses generally contain high hardness and high yield strength, the exceptional ductility is only realized in bulk glass forming alloys.

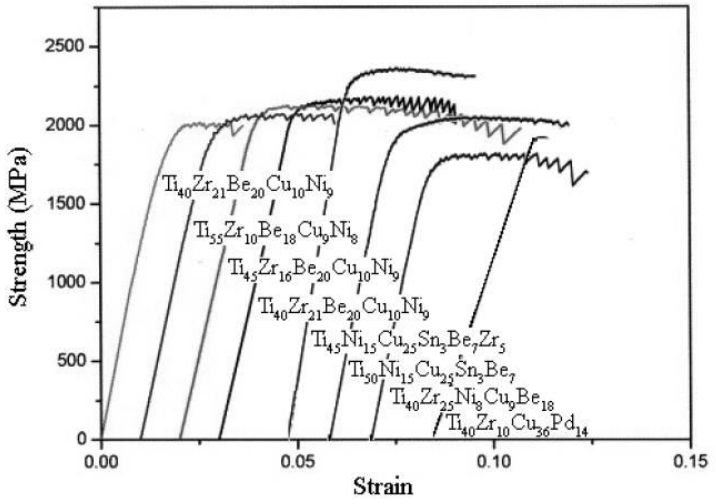


Fig.1.2 Stress-strain curves of Ti-based glasses showing significant ductility [27, 26 and 28].

**Table 1.1** The thermos physical properties viz., the glass transition temperature (Tg), crystallization temperature ($T_x$),liquid *vs.* temperature ($T_l$), super cooled liquid width region ($\Delta T_x$), reduced glass transition temperature ($T_{rg}$),etc. of Ti-based alloys. Critical thickness ($\gamma$) and $D_{max,}$ determined experimentally. (MS denotes alloy was melt spun, critical diameter is below 1 mm).

| Alloy | Tg(k) | Tx(k) | $T_l$(k) | $\Delta T_x$ | $T_{rg}$ | $\gamma$ | $D_{max}$ (mm) | Ref. |
|---|---|---|---|---|---|---|---|---|
| $Ti_{50}Ni_{25}Cu_{25}$ | 707 | 762 | - | 55 | - | - | MS | [29] |
| $Ti_{50}Ni_{10}Cu_{40}$ | 621 | 668 | - | 47 | - | - | MS | [30] |
| $Ti_{60}Ni_{30}Cu_{10}$ | 621 | 673 | - | 52 | - | - | MS | [30] |
| $Ti_{60}$ $Zr_{10}$ $Cu_{10}$ $Ni_{20}$ | --- | 671 | - | - | - | - | MS | [30] |
| $Ti_{50}$ $Zr_{20}$ $Cu_{10}$ $Ni_{20}$ | --- | 716 | - | - | - | - | MS | [30] |
| $Ti_{50}$ $Zr_{10}$ $Cu_{20}$ $Ni_{20}$ | --- | 630 | - | - | - | - | MS | [30] |
| $Ti_{50}$ $Ni_{15}$ $Cu_{32}$ $Sn_3$ | 686 | 759 | 1283 | 73 | 0.57 | 0.385 | 1 | [26] |
| $Ti_{50}Ni_{15}$ $Cu_{25}$ $Sn_3Be_7$ | 688 | 733 | 1207 | 45 | 0.57 | 0.387 | 2 | [26] |
| $Ti_{45}Ni_{15}$ $Cu_{25}Sn_3Be_7Zr_5$ | 680 | 741 | 1142 | 61 | 0.60 | 0.407 | 5 | [26] |
| $Ti_{40}$ $Zr_{25}Ni_8Cu_8Be_{18}$ | 621 | 668 | 1009 | 47 | 0.63 | 0.410 | 8 | [26] |
| $Ti_{50}$ $Zr_{25}Ni_{15}Sn_3Be_7$ | 688 | 733 | 1207 | 45 | 0.57 | - | 2 | [31] |
| $Ti_{45}Cu_{25}Ni_{15}$ $Sn_3Be_7Zr_5$ | 685 | 741 | 1142 | 56 | 0.60 | - | 5 | [31] |
| $Ti_{40}$ $Zr_{10}$ $Cu_{30}$ $Pd_{20}$ | 687 | 747 | 1184 | 60 | 0.537 | 0.380 | 3 | [31] |
| $Ti_{40}$ $Zr_{10}$ $Cu_{36}$ $Pd_{14}$ | 669 | 718 | 1191 | 49 | 0.562 | 0.386 | 6 | [31] |

Structural experimentation has been performed on Ti-Ni-Zr and Ti-Ni-Cu metallic glasses, and is a useful in understanding the structure and resulting glass forming behavior of the more complex alloys. In the evaluation of the neutron scattering results of $(Ti,Zr)_{83}Si_{17}$, the local order has been described as a random distribution of Ti and Zr atoms with Si preferentially bonding with Zr atoms [32]. This is not surprising due to the stronger chemical affinity between Zr and Si (-67 kJ/mol) than Ti and Si (-49 kJ/mol).The tendency for strong Zr-solute interaction was also seen in the $(Ti,Zr)_{50}Cu_{50}$ alloy [33]. This alloy is in contrast to the Ti-Ni-Cu alloy system, which contains stronger bonding between Ti and the constituent solutes, Ni and Cu. A neutron

scattering study has revealed the complex short range order that can occur in the transition from a binary to a ternary metallic glass. The pair distribution function in $Ti_{60}Cu_{40}$ reveals strong Cu-Cu and Cu-Ti correlations. However, with the introduction of Ni, the $Ti_{60}Cu_{26.8}Ni_{13.2}$ alloy indicates the presence of only Ti-Ni and Ti-Cu nearest neighbours. Furthermore, the Ti-(Ni,Cu) interatomic distance is much shorter, 2.6 Å, than that computed from the averaged the diameters of both species, 2.71 Å [34]. The development of this short range order within ternary alloys was termed 'chemical frustration', and linked to increased viscosity and improved glass forming ability.

**Table** 1.2 Summary of Ti-based glasses represented in literature detailing critical properties such as critical thickness, Dmax, fracture stress (MS = melt spun, critical diameter is below 1mm), $\sigma_f$, elastic modulus, E, Vickers hardness, HV, fracture strain under tension ,$\varepsilon_{t,f}$, fracture strain under tension, fracture strain under compression, εt,c, and plastic strain, εp.

| Alloy | $D_{max}$ (mm) | $\sigma_f$ (MPa) | E (GPa) | Hv | $\varepsilon_{t,f}$ | εt,c | εp | Ref. |
|---|---|---|---|---|---|---|---|---|
| $Ti_{50}Ni_{25}Cu_{25}$ | MS | 760 | 80 | 567 | 2.2 | - | 0 | [29] |
| $Ti_{40}Ni_{40}Si_{10}$ | MS | - | - | 1070 | - | - | 0 | [34] |
| $Ti_{50}Zr_{10}Cu_{40}$ | MS | 1483 | 474 | - | 2.6 | 2.4 | 0 | [30] |
| $Ti_{60}Cu_{30}Ni_{10}$ | MS | 1583 | 528 | | 2.6 | 2.7 | 0 | [30] |
| $Ti_{60}$ $Zr_{10}$ $Cu_{10}$ $Ni_{20}$ | MS | 1360 | 528 | - | 2.5 | 2.7 | 0 | [30] |
| $Ti_{50}$ $Zr_{20}$ $Cu_{10}$ $Ni_{20}$ | MS | 1497 | 627 | - | 2.0 | 2.4 | 0 | [30] |
| $Ti_{50}$ $Zr_{10}$ $Cu_{20}$ $Ni_{20}$ | MS | 1660 | 552 | - | 2.6 | 2.6 | 0 | [30] |
| $Ti_{50}$ $Ni_{15}$ $Cu_{32}$ $Sn_3$ | 1 | - | - | - | - | 5.8 | 4 | [26] |
| $Ti_{50}Ni_{15}$ $Cu_{25}$ $Sn_3Be_7$ | 2 | 2170 | - | - | - | 5.8 | 4 | [26] |
| $Ti_{45}Ni_{15}$ $Cu_{25}Sn_3Be_7Zr_5$ | 5 | 2480 | - | - | - | 5.8 | 4 | [26] |
| $Ti_{40}$ $Zr_{25}Ni_8Cu_8Be_{18}$ | 8 | 1810 | - | - | - | 5.8 | 4 | [26] |
| $Ti_{50}$ $Zr_{25}Ni_{15}Sn_3Be_7$ | 2 | 2170 | - | 670 | - | 5.8 | 4 | [26] |
| $Ti_{45}Cu_{25}Ni_{15}$ $Sn_3Be_7Zr_5$ | 5 | 2480 | - | 715 | - | 5.8 | 4 | [31] |
| $Ti_{40}$ $Zr_{10}$ $Cu_{30}$ $Pd_{20}$ | 3 | - | - | - | - | 2.8 | .5 | [28] |
| $Ti_{40}$ $Zr_{10}$ $Cu_{36}$ $Pd_{14}$ | 6 | 1950 | 82 | - | - | 2.8 | .5 | [28] |
| $Ti_{55}$ $Zr_{10}Be_{14}Cu_7$ $Ni_6$ | 2 | 1753 | - | - | - | 3.2 | 1.2 | [27] |
| $Ti_{40}$ $Zr_{10}Be_{14}Cu_7$ $Ni_6$ | 2 | 1978 | - | - | - | 9.3 | 7.4 | [27] |
| $Ti_{40}$ $Zr_{21}Be_{20}Cu_7$ $Ni_9$ | 10 | 2176 | - | - | - | 6.0 | 4.0 | [27] |

### 1.2.9 Unique Advantage of the MG ribbons in Brazing Technology: The Requirement of Low Brazing Temperature.

It is always necessary that the fillers should have low temperature brazing viz., ~800$^{o}$C in Ti brazing technology [39].The undesirable changes in the microstructure and properties of both the base metal and joint are responsible for the temperature limit of

the brazing thermal cycles. Preferably, the brazing temperature of Ti should not exceed the α-β transformation temperature (800$^{o}$C) in order to retain the original microstructure and mechanical properties of the Ti base metal [39]. It would be worthwhile to mention here that Ti-based fillers viz., Ti-Ni-Cu or Ti-Zr-Ni-Cu systems, which provide the performance of the joints with high order has shown the shortcoming of their high brazing temperatures (above 900$^{o}$C) [49, 51, 52].The unwanted formation of brittle intermetallic compounds like $Ti_xCu_y$ and $Ti_xNi_y$ is caused by the limited solubility of Ti with other elements from molten filler [49, 53]. As a matter of fact, the more intensively the reaction occurs between the molten filler and base metal with the formation of thicker intermetallic layers upon increasing brazing temperature. It is also necessary to consider the metallurgical factor like the susceptibility to the erosion of the Ti base metal in contact with the molten filler. It is well known that the significant erosion of Ti takes place when the brazing temperature is low as possible [54].The previously developed fillers like Al and Ag-based systems have produced mixed results as the low-temperature fillers despite the requirements in Ti brazing [55, 56]. Although Al-based fillers provide a brazing temperature substantially below the α-β transformation temperature, the Ti joints brazed with the fillers are brittle and thereby exhibit a low strength and fatigue resistance [49, 57].The followings are the drawbacks for Ag-based fillers: their low resistance to chloride ion induced corrosion and low strength at high temperatures [49, 58]. Since the focus of the present thesis is on use of metallic glasses in brazing, the basic principles of brazing and the related issues are discussed in details below.

## 1.3 Principles of Brazing

### 1.3.1 Definition of Brazing

Brazing can be defined as the metal piecing together procedure, which usages temperature and a braze alloy, often called filler metal in order to obtain a metallurgical bond between two or more separate pieces without melting or substantial modification of the materials structure. The base materials can be called as the materials being joined and positioned in away such that they leaves single a slight gap between the fragments. The braze alloy is placed near to the gap and with melting it is strained in to the gap upon tube action, which techniques a solids joints on cooling. The braze alloy melting temperature should be below the melting point of the base material, however overhead 450$^{o}$C (842$^{o}$F). Brazing, welding and soldering are the commonly used joining processes.

### 1.3.2 The Joining process and its characteristics

It is generally known that brazing compounds multiple structures of slices, different metals and non-metals of non-uniform thickness to be joined where other joining systems cannot be used wastefully. Brazing is most commonly carried out on metals including those are wrought (sheet, bar, tubing, and extrusions), cast (sand, die, shell and pipe) and powdered metal products. Metal-metal joining *viz,*. The joining of ceramics and metallic glasses is sustainable with the advent of the following brazing methods: torch, furnace, induction, and dip and resistance brazing. However, in the present thesis, only the vacuum furnace brazing has been described. The advantages of the furnace brazing process are the following [60]: There is economical fabrication for the complicated assemblies with many joints, the relatively low distortion and war page, high production rates could be easily achieved by using commercially available apparatus and method know-how, the combinations of different materials could be

joined, the materials of different thickness and cross sectional area can be accommodated, the multi-step joining procedures with complex geometries could be designed, the high quality results with reproducibility can be obtained, in the same cycle the brazing can be combined with temperature behaviour and over all, the development is well familiar and standard in handbooks of design.

### 1.3.3 The wetting and spreading phenomena

When the braze alloy (filler metal) is drawn into the space between two close and parallel surfaces, a braze joint is formed. The nature of this movement is due to capillary action and it actually occurs in the following three steps: adhesion, wetting and spreading of the braze alloy. The surface tension acting on a drop of braze alloy and described in figure .1.3.

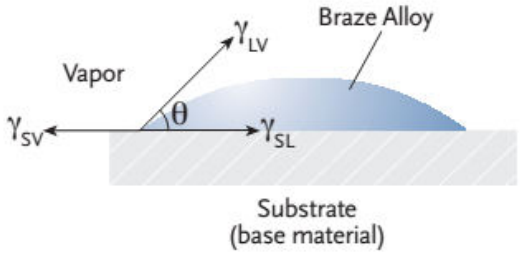


$\gamma_{SV}$ – Surface tension at the solid/vapor interface

$\gamma_{LV}$ – Surface tension at the liquid/vapor interface

$\gamma_{SL}$ – Surface tension at the solid/liquid interface

Fig.1.3 The surface tensions on a drop of braze alloy [61].

The wetting can be estimated by analysing the mathematical balance between the horizontal components of the surface tensions, which is commonly known as Young' s equation.

$$\gamma_{SV} - \gamma_{SL} = \gamma_{LV} \cos \theta \qquad \text{(Eq. 1)}$$

The contact angle (θ) is a measure of the quality of wetting. For good wetting, θ must be smaller than $90^o$. In fact, for good wetting and proper joint to form, $\theta<60^o$ is essential in real practice.

The above equation 1 shows that $\theta<90^o$ corresponds to the condition ($\gamma_{SV}>\gamma_{SL}$). The improved wetting with low contact angle (θ) can be achieved by increasing $\gamma_{sv}$, decreasing $\gamma_{SL}$ and decreasing $\gamma_{Lv}$. Fig .1.3 describes the specific application to brazing. When $\theta<90^o$, there is a wetting, however, for $\theta>90^o$, there no wetting. The alloying occurs when the reaction between filler and base metals takes place and accordingly, the change of Free Energy contributes to the wetting due to that reaction.

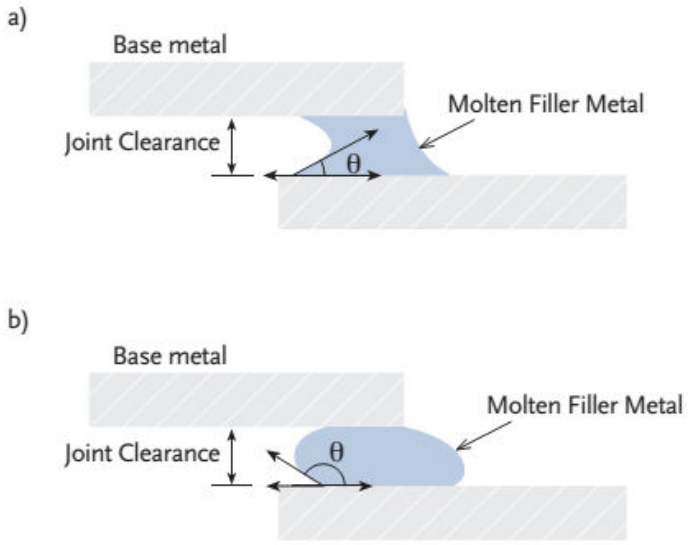


Fig.1.4 (a) The effective wetting and (b) poor wetting [62].

The wetting properties vary with different materials [63]. Titanium, zirconium, ceramics, glass, and titanium carbide are difficult to wet. Al, cast iron, W, WC, Mo, Tl, and the alloys with more than 5 % metals forming refractory oxides fall in the category fair wetting. However, Cu, Ni, Co-alloys, steels and precious metals also fall in the category of fair wetting.

### 1.3.4 The quality of brazing and its design

As a part of the overall component, the braze joint must be designed. The configuration of the joint shows a vital role in mechanical, fatigue and corrosion resistance, thermal, electrical and physical properties of the final assembly. The examples of common braze joints are given in figure 1.4 [64].

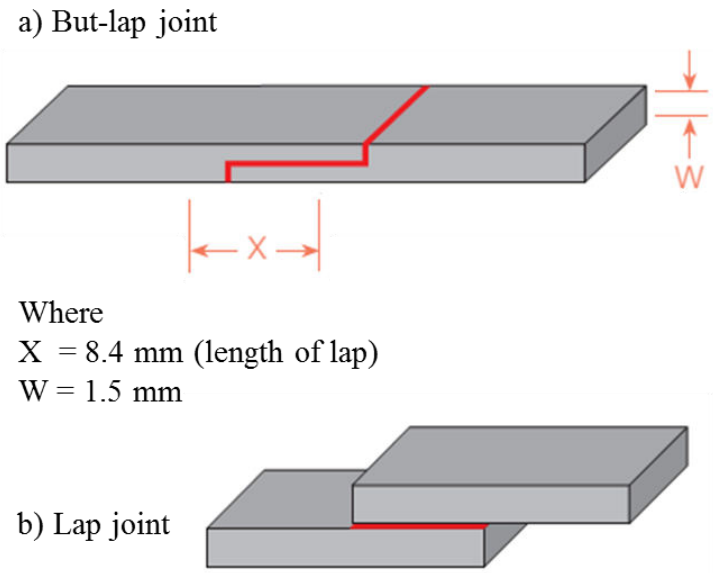


Fig.1.5. Basic type of brazes joint configurations [65].

### 1.3.5 The butt joints

The strength of the joints depending on the bonding area and hence, the strength of the joint is lower when the available bonding area is smaller. The only available bonding surfaces are the cross sectional area of the pieces being joined and therefore, the strength of the joint are limited in a butt joint. The smooth contour and clean appearance are the major advantage of this configuration. The low strength is the major disadvantage where it makes this type joint fairly uncommon.

### 1.3.6 The butt-lap joint

In order to provide mating surfaces, the increased mechanical strength was obtained due to the increased amount of contacting surface. The stress concentration of the profile minimizes and hence, reduces the risk of crack initiation. The controlled gap spacing obtained in this type of joint. The machining, cleaning and set-up added steps during production increased the manufacturing cost.

## 1.4 Applications of brazing materials and metallic glasses

Metallic glasses exhibit excellent mechanical and soft magnetic properties, therefore, their usage have been targeted for many applications [76-77]. Most of the metallic glasses, in ribbon form, have been used for power distribution transformers, recording heads, magnetic shielding, transducers as well as magnetic sensors, electronic applications, to name a few.

The bulk metallic glasses are shown very attractive properties recently and these properties are generally enhanced by suitable heat treatment method. The high amount of elastic energy stored by the bulk metallic glasses, which can useful as potential spring material. This unique combination of properties has made it first and most visible utility in the field of golf clubs. The addition of ceramic second phase particles can be imparted to increase the considerable amount of strength into the material. As an armor penetrator material, this composite can be used. For the use in aircraft frames, automobiles and medical implants, the possibilities of bulk metallic glasses as structural materials can be envisaged. The workability of the material is very high because the materials have large super-cooled liquid regions.

In friction welding of Pd-based BMGs, this property has been exploited [58]. There is no crystallization at the welded interface upon friction welding and thereby the strength of the interface is almost similar to that of the base metallic glass. BMGs have been

promoted as prime structural materials with this overview. Although the magnetic properties and nanocomposites produced from them upon devitrification have many exciting new applications [79], these have not been discussed in the present thesis. The utility of BMGs as ideal optical, die, tool and cutting materials because of their high strength, hardness, fracture toughness and fatigue strength. Therefore, the metallic glasses are useful for attractive materials for numerous applications [80] because of the combined excellent soft magnetic properties with high strength, bond ductility, toughness and corrosion resistance.

### 1.5 Motivation

We have been motivated based on the above discussion where there is a reasonable understanding of brazing propagation, only limited efforts were made to study brazing mechanism. Hence, the main work in the present thesis is to understand the mechanism of brazing, microstructural evaluation and phase studies of these metallic glasses. This thesis describes the research work on the investigation of the glass forming ability (GFA) of $(Ti_{0.5}Zr_{0.5})_{40}$ $(Cu_xNi\ (1\text{-}x))_{60}$ systems and the evolution of structures during rapid solidification. Attempts will be made to braze Ti metal using the ribbon and evaluate the brazability of the ribbons. Initially, calculations will be carried out to evaluate the theoretical GFA of Ti-Zr-Cu-Ni based metallic glass alloy. As of today, the data available on the properties of joints obtained with these advanced filler metals are still limited.

Hence, development of new brazing alloy with higher glass forming ability, strength and low melting temperature is a challenging task to reduce the distortion in the inherent microstructure of the base metal and joint. It can be noticed from the literature that GFA of Ti-Zr-Cu-Ni system has not been investigated extensively. The effect of various alloying elements has also not been studied in details. Moreover, limited

information is available on the mechanical behaviour with respect to the composition variation. Development of brazing materials for joining titanium based alloy is a current topic of interest due to the expanding utility of these alloys in aerospace, chemical apparatuses, heat exchangers, etc. The Ti based brazing alloys as filler materials are generally brittle and used in the form of powders, pastes, sprays, which will be spread prior to the joining operation. This may lead to porous joint because of the entrapped air in the powder. The main problem in the brazing of titanium is due to the formation of brittle intermetallic compounds between Ti and filler metal elements at the base metal-filler interface with the formation of brittle joints and high galvanic corrosion. The above problem can be overcome by using amorphous titanium-zirconium-based alloys in ribbons form produced through melt spinning method. They possess several advantages over the conventional crystalline filler materials such as better diffusivity of elements in amorphous state, good ductility, compositional homogeneity, accelerated interfacial reaction by improving wetting conditions, etc. Therefore, the usage of fluxes (which modify the wetting properties) can be avoided and cleaner joints can be achieved. The effect on structural, thermal and mechanical properties of Ti-Zr-Cu-Ni metallic glasses and Ti-alloy has been studied based on the above observation in the present investigation.

## 1.6 Objective

Since the work reported in this Thesis is on metallic glasses in ribbon form, no further reference will be made on bulk metallic glasses. Although an effort was made to produce one composition but due to unavailability of arc furnace, the work could not be pursued, therefore, the work reported here is for the conventional ribbon form of metallic glasses. The bulk metallic glasses are highly demanded in aerospace and critical ground-based applications, which require heat and wear-resistance because of

their excellent properties of low density, high strength and corrosion resistance. With the high specific strength and excellent corrosion resistance, the Ti is very much useful in producing transition joints to other engineering materials namely, steels, Ni-based and Cu-based alloys for expanding its practical application. A dissimilar joining of Ti to Cu has significant technological importance, as this combination of materials finds wide applications in heat exchanger components for power generation industries.

**Based on the above background and motivation, the objectives of the present study are:**

- Synthesis of the $Ti_{20}Zr_{20}Cu_{60-x}Ni_x$ (x= 10, 20, 30, 40 and 50) metallic glasses using arc milting furnace.
- Development of brazing materials for joining Titanium based alloy is a current topic of interest due to the expanding use of these alloys in aerospace, chemical apparatuses, heat exchangers, etc.
- Characterization of metallic glasses and brazing consolidated with Ti-alloy using different characterizing techniques.
- Measure the mechanical properties using Nanoidentation techniques. Universal Testing Machine for mechanical properties and Four probe method for electrical properties.
- This thesis mainly focused on clarifying the microstructure evolution mechanism of Ti/Ti-Zr-Cu-Ni/Ti composite filler, which was summarized by analysing the effect of holding time and Ti content on the microstructure of joints.

## References


1. J. Schroers, T. M. Hodges, G. Kumar, H. Raman, A. J. Barnes, Q. Pham, and T. A. Waniuk, Mater. Today 14, 14 (2011).
2. W. Klement, R. H. Willens, P. Duwez, Nature 187 (1960) 869-870.
3. W. H. Wang, C. Dong, C. H. Shek, Materials Science & Engineering R-Reports 44 (2004) 45-89.
4. A. Inoue, ActaMaterialia 48 (2000) 279-306.
5. A. Inoue, W. Zhang, T. Zhang, K. Kurosaka, ActaMaterialia 49 (2001) 2645-2652.
6. S. Shin, Materials Science Forum 449-4 (2004) 945-948.
7. Mott N. F., "Electronic Processes in Non-crystalline Materials" (Oxford, UK, 1979); Phil. Mag. 17 (1968) 1259,; Phil. Mag. 22 (1970) 7; J. Non-Cryst. Solids 1 (1969) 1
8. Anderson P. W., Phys. Rev. 109 (1958) 1432.
9. Cahn R. W., Contemp. Phys. 21 (1980) 43; Chen H.S., Rept. Prog. Phys. 43 (1980) 353; Egami T., Rept.Prog. Phys. 47 (1984) 160.
10. Glover R. E., Phys. Lett. 25A (1967) 542; Naugle D.G. and Glover R.E., Phys. Lett. 28A (1968) 110.
11. Klement Jr. W., Willens R. H. and Duwez P, Nature 187 (1960) 869.
12. Klement Jr. W., Willens R. H. and Duwez P, Nature 187 (1960) 869.
13. F. E. Luborsky (Ed.) "Amorphous Metallic Alloys" (Butterworths& Co. Ltd., London 1983).
14. K. Moorjani and J M D Coey, "Magnetic Glasses" (Elsevier, Amsterdam, 1984).
15. Inoue A., Zhang T., and Masumoto T., Mater. Trans. Japan Institute of Metals 30 (1989) 965.
16. Inoue A., Kato A., Zhang T., Kim S.G. and Masumoto T., Mater. Trans. JIM 32 (1991) 609.
17. Zhang T., Inoue A. and Masumoto T., Mater. Trans. JIM 32 (1991) 1005.

18. Peker A. and Johnson W.L., Appl. Phys. Lett. 63 (1993) 2342.

19. Inoue A., Nishiyama N. and Kimura H., Mater. Trans. JIM 38 (1997) 179.

20. A. J. F Löffler, Bulk metallic glasses, Intermetallics 11 (2003), pp.529-540.

21. Johnson W. L., Inoue A. and Liu C. T. (Eds.). "Bulk metallic glasses". Materials Research Society, vol. 554.(1999).

22. Inoue A., Yavari A. R., Johnson W. L. and Dauskardt R. H. (Eds.), "Supercooledliquid,bulk glassy and nanocrystalline states of alloys" Materials Research Society, vol. 644 (2001).

23. Kelton K. F., Greer A. L. and Rajan K. (Eds.), "Advances in metallic glasses", J Non-Cryst Solids 317 (2003)1–220.

24. Nieh T. G. (Ed.), "Bulk metallic glasses II". Intermetallics 10 (2002) 1035.

25. Buchanan O, "Bulk metallic glasses used for manufacturing net shape metal products", MRS Bull 27 (2002) 850.

26. Shiue RK, Wu SK, Chen YT, Shiue CY. Infrared brazing of Ti50Al50and Ti–6Al–4V using two Ti-based filler metals. Intermetallic 2008; 16:1083–9.

27. KamachiMudali U, AnandaRao BM, Shanmugam K, Natarajan R, Raj B.Corrosion and microstructural aspects of dissimilar joints of titanium and type 304L stainless steel. J Nucl Mater 2003; 321:40–8.

28. Lee MK, Lee JG, Lee JK, Park JJ, Lee GJ, Uhm YR, et al. Strong bonding of titanium to copper through the elimination of the brittle interfacial intermetallics.J Mater Res 2008;23:2254–63.

29. Schwarz M. Brazing: for the engineering technologist. New York: Chapman &Hall; 1995.

30. Elrefaey AA-M, Tillmann W. Microstructure and mechanical properties of brazed titanium/steel joints. J Mater Sci 2007; 42:9553–8.

31. Shiue RK, Wu SK, Chan CH. Infrared brazing Cu and Ti using a 95Ag–5Al braze alloy. Metall Mater Trans A 2004; 35A:3177–86.

32. Shiue RK, Wu SK, Chan CH. The interfacial reactions of infrared brazing Cu and Ti with two silver-based braze alloys. J Alloys Compd 2004; 372:148–57.

33. Shapiro A, Rabinkin A. State of the art of titanium-based brazing filler metals.Weld J 2003; 82:36–43.

34. Hong IT, Koo CH. Microstructural evolution and shear strength of brazing C103 and Ti–6Al–4V using Ti–20Cu–20Ni–20Zr (wt. %) filler metal. Int J Refract Met H 2006; 24:247–52.

35. Onzawa T, Suzumura A, Ko MW. Brazing of titanium using low-melting-point Ti-based filler metals. Weld Res Suppl 1990; 69:462-7

36. Peker A, Johnson WL. A highly processable metallic glass: Zr41.2Ti13.8Cu12.5-Ni10.0Be22.5. ApplPhysLett 1993; 63: 234-238.

37. Lee JG, Lee J-K, Lee M-K, Shim D, Rhee CK. Brazing of Ti using a Zr-based amorphous filler. Solid State Phenom 2008; 135: 131-134.

38. Lee JG, Choi YH, Lee JK, Lee GJ, Lee MK, Rhee CK. Low-temperature brazing of titanium by the application of a Zr–Ti–Ni–Cu–Be bulk metallic glass (BMG) alloy as a filler. Intermetallics 2010; 18: 70–3.

39. Shapiro A, Rabinkin A. State of the art of titanium-based brazing filler metals.Weld. J. 2003; 82: 36–43.

40. Botstein O, Rabinkin A. Brazing of titanium-based alloys with amorphous 25 wt.%Ti–25 wt.%Zr–50wt.%Cu filler metal. Mater. Sci. Eng. A 1994; 188: 305–15.

41. Chang CT, Shiue RK, Chang CS. Microstructural evolution of infrared brazed Ti-15-3 alloy using Ti–15Cu–15Ni and Ti–15Cu–25Ni fillers. Scr Mater 2006; 54: 853–8.

42. Shiue RK, Wu SK, Chen YT, Shiue CY. Infrared brazing of Ti50Al50and Ti–6Al–4V using two Ti-based filler metals. Intermetallics 2008; 16:1083–9.

43. Takemoto T, Okamoto I. Intermetallic compounds formed during brazing of titanium with aluminium filler metals. J. Mater. Sci 1988; 23:1301–8.

44. Humpston G, Jacobson DM. Principles of soldering and brazing. Metals Park, Ohio: ASM International; 1993.

45. Sohn WH, Bong HH, Hong SH. Microstructure and bonding mechanism of Al/Ti joint using Al–10Si–1Mg filler metal. Mater SciEng A 2003; 355:231–40.

46. Shiue RK, Wu SK, Chan CH. The interfacial reaction of infrared brazing Cu andTi with two silver-based braze alloys. J. Alloys Compd 2004; 372:148–57.

47. Flom YA. Electron beam brazing for in-space construction. Weld J 2007; 86:33–7.

48. Liaw DW, Shiue RK. Brazing of Ti–6Al–4V and niobium using three silverbased alloys. Metall. Mater. Trans. 2005; 36A:2415–27.

49. Schwartz M. Brazing, 2nd Edition, ASM International, Materials Park, 2003.

50. ASM Handbook 6, Welding Brazing and Soldering, ASM International, Materials Park, 1993.

51. Gundel P. personal communication

52. Hermanek F.J. An introduction to brazing, brochure, Alloy Metals, Inc.

53. Brazing Handbook, 4th edition, American Welding Society, Miami, 199

54. Humpston G., Jacobson D.M., Principles of Soldering and Brazing, ASM, Materials Park, 1993

55. Edenhofer B., Steel Treatment Handbook, edited by G.Totten&M.Howes, Marcel Dekker, Inc., New York, 1997

56. F. E. Luborsky (Ed.) "Amorphous Metallic Alloys" (Butterworths& Co. Ltd., London 1983).

57. Proceedings of various Conferences on Rapidly Quenched and Metastable Metals

58. 57 Evans R., Greenwood D. A. and Lloyd P., Phys. Lett. A35 (1971); 38 (1972) 151.

59. Oilmen J. J., Metal Progress. 116 (1979) 42.

60. J. M. Park, H. J. Chang, K. H. Han, W. T. Kim and D. H. Kim, Scripta Mater. 53(2005), 1.

61. T. Fukunaga, K. Suzuki and U. Mizutani, J. of Non-Cryst. Solids 150 (1992),10.

62. L. E. Tanner and R. Ray, Scripta Metall. 11 (1977), 783.

63. Y. C. Kim, W. T. Kim and D. H. Kim, Mater. Sci. Eng., A 375-377 (2004), 127.

64. Oerlikon, An Introduction to Brazing, Fundatametals and Materials Processing. Issue 4-Septermebr, 2014.

65. S. L. Zhu, X. M. Wang, F. X. Qin. and A. Inoue, Mater. Sci. Eng., A 459 (2007), 233.

66. T. Zhang, A. Inoue and T. Masumoto, Mater. Sci. Eng., A 181-182 (1994), 1423.159

67. K. Amiya, N. Nishiyama, A. Inoue and T. Masumoto, Mater. Sci. Eng., A 179-180 (1994), 692.

68. Y. C. Kim, D. H. Bae, W. T. Kim and D. H. Kim, J. of Non-Cryst. Solids 325 (2003), 242.

69. T. Fukunaga, S. Shibuya, M. Misawa and K. Suzuki, J. of Non-Cryst. Solids 95-96 (1987), 263.

70. D. E. Polk, A. Calka and B. C. Giessen, Acta Metall. 26 (1978), 1097.

71. Schwartz M., Brazing, 2nd Edition, ASM International, Materials Park, 2003.

72. ASM Handbook 6, Welding Brazing and Soldering, ASM International, Materials Park, 1993.

73. Brazing Handbook, 4th edition, American Welding Society, Miami, 199

74. Oliver J., Lille C., Pettersson R., Nylén M., Evaluation of Nibrazed prototypes in stainless & tool steels (VAMP-13), SwedishInstitute for Metals Research Report IM-2002-549.

75. Lille C., Chèse I., Pettersson R.F.A., "Corrosion of Brazed Joints in Stainless and Tool Steels (VAMP 13)", SwedishInstitute for Metals Research Report IM-2001-535.

76. Claesson E., Engström H., Holm T., Schölin K., "Nitrogen Flow Optimization System for CAB (NOCOLOK) Furnaces", VTMS Conference, England, May 1995.

77. Do Nascimento R. M., Martinelli A. E., A. BuschinelliJ. A., Review Article: Recent advances in metal-ceramic brazing, Ceramic 49 (2003) 178-198.

78. Holm T., Wiberg S., Mahlo T., Anderson R., Furnace Atmospheres for Tube Annealing, Linde Gas Special Edition, 2004.

79. Brazing Handbook, 4th edition, American Welding Society, Miami, (1999)

80. B.B. Medeiros et al (2015) Journal of Non-Crystalline Solids 425 103–109.

# Chapter 2 Experimental Techniques

## 2. Introduction

This chapter gives experimental techniques used in the research work presented in this thesis. Only brief details of the techniques used in the work are given as most of these techniques are standard ones and widely used in materials research. The experimental details to produce the alloys and ribbons for brazing joints are described in this chapter. All the characterization techniques have also been described in details to explore physical, structural, microstructure, thermal, electrical, mechanical and brazing studies of the metallic glass. Alloys of nominal compositions were prepared using vacuum arc melting furnace and then solidified rapidly using melt spinning technique to produce ribbons. These ribbons were then heat treated in vacuum furnace. At the same time these melt spun ribbons were used for brazing of Ti bar through butt and butt-lap joint techniques.

X-ray Diffractometry (XRD) was used for structure determination, whereas Differential Scanning Calorimerty (DSC) and Differential thermal analysis (DTA) were utilised for phase stability in the present study. The Field Emission Scanning Electron Microscopy (FESEM) and Transmission Electron Microscopy (TEM) were employed for morphology and phase identification and Atomic Force Microscopy (AFM) for surface characteristics. Energy Dispersive X-ray Spectroscopy (EDXS) for analysis of composition and Nanoindentation, Universal Testing Machine for mechanical properties and Four probe method for electrical properties.

## 2.1 Sample Preparation

There are a number of techniques to produce amorphous materials. To produce such a material requires rapid quenching of a vapour or a melt of a material in question in order to avoid crystallization. We have used rapid melt quenching to produce the samples studied in the work reported here. There are a few techniques by which rapid melt-quenching can be obtained. These are (a) splat quenching, (b) spark erosion, (c) copper roller quenching and (d) laser glazing among others [2.1-2.6]. The quenching rates are usually different for each technique the highest cooling rate is obtained by laser glazing while copper roller quenching provides rates between $10^4$ to $10^6$ K/s. We have used the technique of copper roller quenching procedure to produce metallic glasses with nominal compositions given by $Ti_{20}Zr_{20}Cu_{60-x}Ni_x$ (x = 10, 20, 30, 40 and 50.). These were produced in the ribbon form as described below.

### 2.1.1 Alloy preparation

The first step in preparing a metallic glass ribbon of a given composition is to prepare the crystalline alloy of the same composition. Therefore, alloys of $Ti_{20}Zr_{20}Cu_{60-x}Ni_x$, where x= 10, 20, 30, 40 and 50, were prepared using a vacuum arc melting furnace with a water cooled Cu-hearth. Ti, Zr, Cu, and Ni constituent metals with purity higher than 99.5% were weighed in appropriate amounts to make an alloy of a given composition. A batch of 50 gm was used for each composition alloy. The arc melting chamber was first evacuated to a pressure of ~$3x10^{-4}$ mbar followed by flushing multiple times using 99.9999 % pure Ar. Finally, the melting was carried out in the Ar pressure of 1200 mbar. To achieve sufficient homogeneity within the alloy, the master alloy was re-melted up to 5 times. The weight loss for an alloy after melting and homogenization was observed to be less than 0.1%.

## 2.1.2 Melt spinning

Rapid solidification of each alloy was carried out to produce glassy ribbons using a vacuum melt spinning equipment. A schematic of the set-up is shown in Fig 2.1.

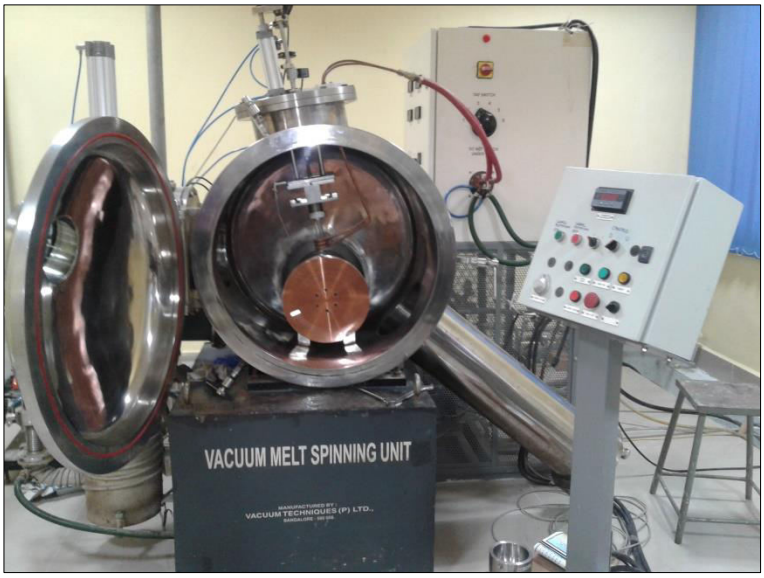


Fig.2.1 The schematic figure of vacuum melt spinning technique.

It is enclosed in an appropriate system/enclosure with a window which could be evacuated or pressurized. An alloy ingot of a given composition was placed in a quartz crucible with a hole at bottom. The crucible was placed in an RF induction coil which was used to heat the sample by passing RF current through the coil.


Fig.2.2 The $Ti_{20}Zr_{20}Cu_{50}Ni_{10}$ metallic glass ribbon.

The enclosure was evacuated to ~$10^{-4}$ mbar. Once the alloy is melted by RF induction heating, then the melt is injected using pure. Ar gas pressure of ~0.35 bar onto a rotating 300 mm diameter of copper wheel with a speed 2500 rpm. This procedure produced continuous ribbons of metallic glass of the composition which was placed in the crucible. A photograph of the ribbon, having composition $Ti_{20}Zr_{20}Cu_{50}Ni_{10}$, is shown in Fig. 2.2

## 2.2 Characterization of the samples

### 2.2.1 X-ray Diffraction

Samples, prepared as described above, were first characterized by X-ray diffraction (XRD) [4-5] to make sure that the prepared samples were amorphous/glassy in nature and not crystalline. If a sample is polycrystalline, then XRD pattern will show sharp peaks or diffraction maxima. The X-ray diffraction maxima for a polycrystalline material are described by Bragg's law which is represented mathematically as

$$2d_{hkl} \text{ Sin } \theta_{hkl} = n\lambda, \qquad (2.1)$$

where 'n' gives the order of diffraction, '$\lambda$' is wavelength of X-rays, $\theta_{hkl}$ is the angle between the incident X-ray beam and atomic lattice plane in the crystal with Miller indices (hkl) and $d_{hkl}$ is the distance between the set of parallel lattice planes**.** However, if the material is amorphous or glassy, the XRD will show a major broad peak at low angle, usually between $2\theta = 30^o$ to $40^0$ and sometimes another small broad peak at higher angles may also appear. A schematic of two XRDs is shown in Fig. 2.5.

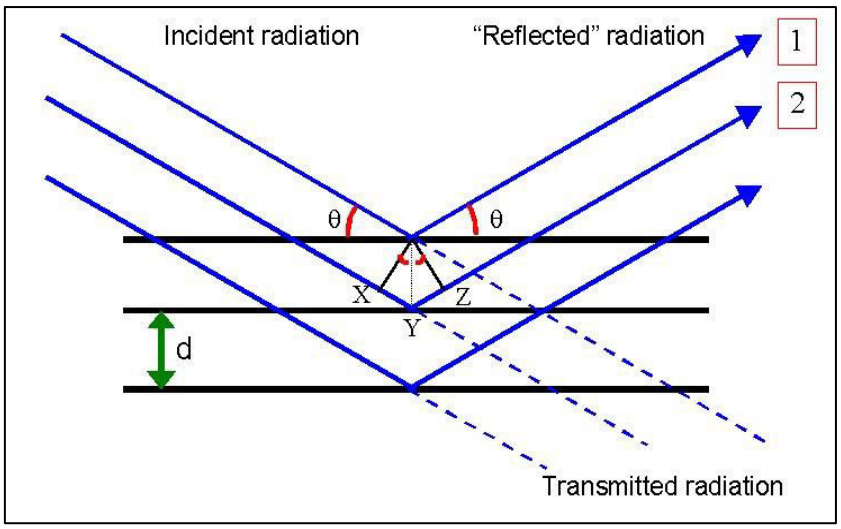


Fig. 2.3 The representation of the Braggs diffraction condition [2].

Two X-ray Diffractometers (Bruker Model No.D8 and Rigaku, Ultima IV) were used in the present work to characterize each metallic glass sample produced. As it will be shown later, each $Ti_{20}Zr_{20}Cu_{60-x}Ni_x$, (x = 10, 20, 30, 40 and 50) ribbon sample showed a broad peak in their XRD confirming the glassy nature of the sample. Annealing study was done on each sample by heating a given sample to a high temperature for a fixed time and X-ray diffraction studies were performed to determine the crystallized products. A portion of the ribbon of each $Ti_{20}Zr_{20}Cu_{60-x}Ni_x$ alloy was annealed under vacuum at different temperatures depending on the crystallization temperature of the individual alloys as determined by the DSC run. A small length of each alloy was placed in a quartz tube, which was evacuated to ~$3\times10^{-4}$ mbar pressure. Annealing for each sample at a given temperature as listed in Table 2.2, was carried out for 30 minutes duration. These temperatures were chosen on the basis of the Differential Scanning Calorimeter (DSC) runs as described later. After annealing these samples were subjected to X-ray diffraction runs to determine the structural changes which took place due to annealing.

Table 2.1 List annealing Temperatures.

| Composition of Ribbon | Annealing temperature (K) |
|---|---|
| $Ti_{20}$ $Zr_{20}$ $Cu_{50}$ $Ni_{10}$ | 753 ±5 |
| $Ti_{20}$ $Zr_{20}$ $Cu_{40}$ $Ni_{20}$ | 756 ±5 |
| $Ti_{20}$ $Zr_{20}$ $Cu_{30}$ $Ni_{30}$ | 758 ±5 |
| $Ti_{20}$ $Zr_{20}$ $Cu_{20}$ $Ni_{40}$ | 778 ±5 |
| $Ti_{20}$ $Zr_{20}$ $Cu_{10}$ $Ni_{50}$ | 783 ±5 |

### 2.2.2. Differential Scanning Calorimetric Technique (DSC)

The thermal characteristics of melt spun ribbons were evaluated using a Differential Scanning Calorimeter (DSC 821, METTLER – Toledo). The temperature and other calibrations of the instrument were done using the melting curve of 99.999% pure indium. The sample and reference pans or cups were made up of recrystallized aluminum. Typical mass of the sample used in the experiment was about 10 mg. Commercial Argon gas was used as the purge gas at a rate of 45 SCM using a mass flow controller. DSC scans were performed using a constant heating rate of 10, 20, 30 and 40 K/min (10, 20, 30and 40 °C/min), from room temperature to (650 °C), with temperature and power input accuracies of ± 0.1 K (± 0.1°C) and 0.2 μW, respectively. The crystallization temperatures are determined from onset of exothermic peak of the DSC curve. For each specimen analyzed, multiple scans were performed and the second scan was taken as an instrument baseline.

### 2.2.3 Differential Thermal Analysis (DTA)

Differential thermal analysis was done in conventional equipment (Shimadzu Thermal Analyzer Dt-40). The DTA technique was used to evaluate the melting point of the $Ti_{20}$-$Zr_{20}$-$Cu_{60-x}$-$Ni_x$ (x= 10,20,30,40 and 50) ribbons. All measurements were performed in Argon atmosphere. Alumina pans were used for material. The data were recorded at a heating rate of $10^oC$/min from room temperature to about $1200^oC$.

### 2.2.4 Kinnetics during Nonisothermal Transformation

Kissinger (1956) procedure was used to evaluate average activation energy, E. The details of Kissinger procedure is as follows. The basic equation that relates the rate of reaction to the fraction of the materials decomposed may be written as (Murray et al 1949 and Vaughan 1955)

$$\left(\frac{dx}{dt}\right)T = \mathrm{KT}(1-X) \qquad (1)$$

Where, x is the fraction of the materials decomposed, $K_T$is the magnitude of the rate constant and is given by the Arrhenius equation

$$KT = A\, e^{-\frac{E}{RT}}$$

Where, A and E are the frequency factor and activation energy respectively. Here, A is a measurement of the probability that a molecule will participate in a reaction and E is energy barrier opposing the reaction (Kissinger 1956) [1].By applying the condition that the reaction rate is maximumsuch that its derivation with respect to time is zero, one can obtain a final equation of the form (Chen 1978 and 1981)

$$\frac{E}{KBT_p} = Ln\left[\frac{T_p^2}{\emptyset}\right] + constant \ldots\ldots\ldots\ldots\ldots 3$$

Where,$T_p$ is the peak temperature, Φ is the heating rate and $K_B$ is the Boltzmann constant.InaLn ($\Phi/T^2p$) vs.1/Tp plot the slope will give the quantity (E/KB).

The activation energy of the crystallization event was determined by an approximation method proposed by Augis and Bennett (1978)[2]. Their approach showed a linear relation between ($ln\ \Phi/T_p$ ) and ($1/T_p$) while linear relation between ($ln\Phi/T^2_p$ ) and ($1/T_p$) was considered for the Kissinger model. The Augis and Bennett modelis described by the following equation [2]

$$Ln(\frac{\Phi}{T_p}) = -\frac{E_c}{RT_p} + Ln(K_0) \quad (4)$$

Where, the pre-exponential term $K_0$ is the frequency factor.

Moreover, another model proposed by Ozawa (1965) [3] was also used to estimate the activation energy during crystallization. This model describes a linear relation between ($Ln\ \Phi$) and ($1/T_p$) unlike Kissinger equation or Augis-Bennett model. The Ozawa model is described as:

$$Ln(\Phi) = -\frac{E_c}{RT_p} + const \quad (5)$$

The slope of $Ln\ (\Phi)$ versus $(1000/T_p)$ plot will give the magnitude of ($E/K_B$).

## 2. 3 Brazing

Vacuum brazing was performed to braze commercially pure CP-Ti plates using the as spun $Ti_{20}Zr_{20}Cu_{60x}Ni_x$ (x=10, 20, 30, 40 and 50) metallic glass ribbons as filler materials. The schematic representation of a typical brazing process cycle was shown in Figure 2.3, whereas Figure 2.4 showed the sample joints of different configuration used for the present study.

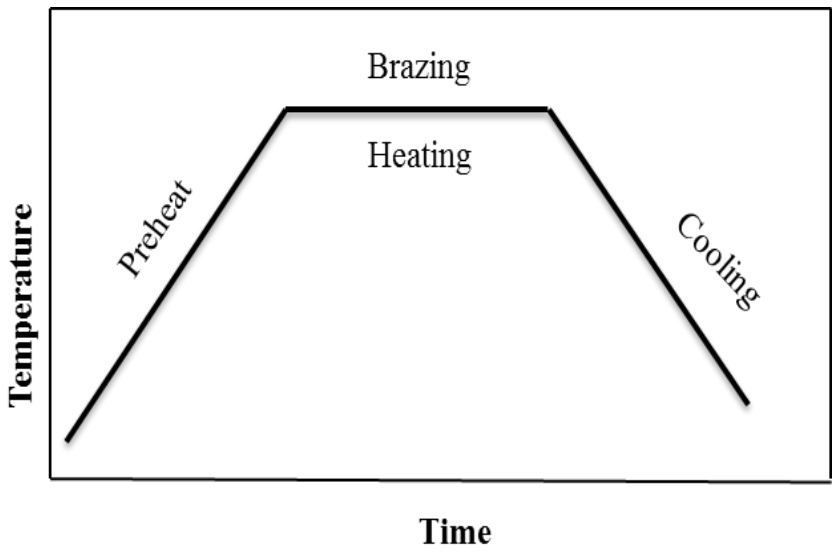


Fig. 2.4 The schematic of a typical brazing process cycle.

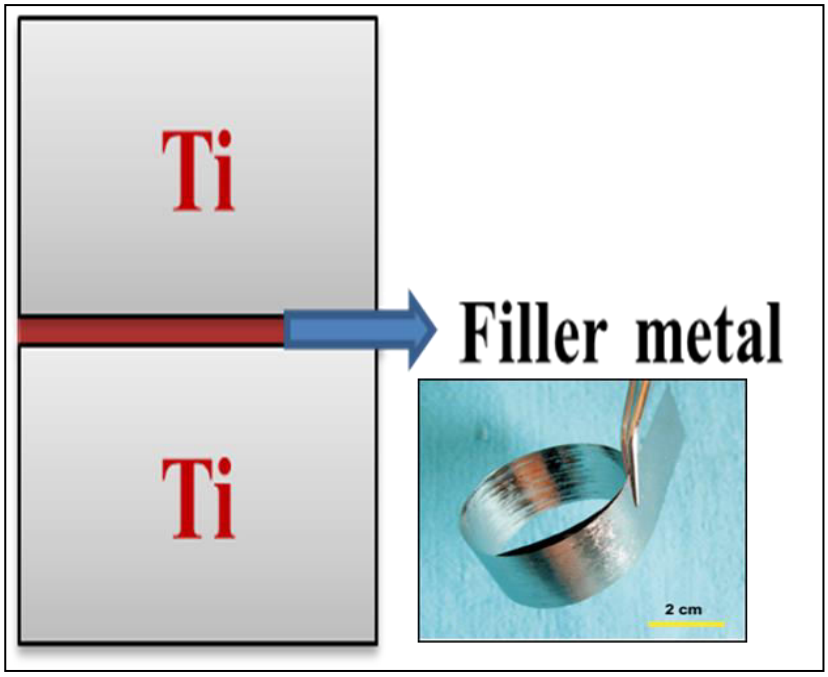


Fig. 2.5 Brazed samples Lap joint method.

For each filler ribbon, the joint with the lap configuration was used for detailed microstructural characterization whereas the joint with the lap-butt joint configuration was used for measuring tensile strength. Both types of sample joints were vacuum brazed at the same time in the vacuum furnace such that the microstructural features can be correlated with the mechanical properties. For the butt joint, the CP-Ti plates measuring 10 mm×7 mm× 3mm were prepared. In case of the lap-butt joint, the CP-Ti plates measuring 5 mm×3 mm×1 mm were first prepared and then steps were cut in EDM using a 0.5 mm wire. The reason for using lap-butt joint configuration was to increase the contact area of the joint with the expectation of an enhanced mechanical strength, as mentioned earlier in Chapter 1. The lap-butt joint profile also helps in minimizing the concentration of the stress and as a result reduced the risk of crack initiation. Thus, about 40 to 50μm thick, 8 mm wide and 15 mm long $Ti_{20}Zr_{20}Cu_{60-x}Ni_x$ (x=10, 20, 30, 40 and 50) (at. %) alloy ribbons were used as brazing filler. Both the brazing ribbons and Ti plates were initially cleaned using acetone and then the ribbons were kept in between the two Ti plates before tightening them using nicrome wire. The

samples were then placed in a vacuum furnace ($10^{-3}$ mbar) and annealed for 10 minutes. Table 2.1 shows the details of the specific annealing temperature-annealing time combinations used for different filler ribbons. The selected temperature for each sample was 20±5$^{o}$C higher than the solidus temperature of respective ribbon. The samples were then furnace cooled.

Table 2.2 Summary of annealing conditions used in the brazing experiment.

| Filler metal/ wt% | Annealing temperature/$^{o}$C | Annealing time/min |
|---|---|---|
| $Ti_{20}$ $Zr_{20}$ $Cu_{50}$ $Ni_{10}$ | 990 | 10 |
| $Ti_{20}$ $Zr_{20}$ $Cu_{40}$ $Ni_{20}$ | 967 | 10 |
| $Ti_{20}$ $Zr_{20}$ $Cu_{30}$ $Ni_{30}$ | 995 | 10 |
| $Ti_{20}$ $Zr_{20}$ $Cu_{20}$ $Ni_{40}$ | 1004 | 10 |
| $Ti_{20}$ $Zr_{20}$ $Cu_{10}$ $Ni_{50}$ | 1006 | 10 |

## 2.4 Microstructural characterization

The microstructures of $Ti_{20}$-$Zr_{20}$-$Cu_{60-x}$-$Ni_x$ (x= 10,20,30,40 and 50) metallic glasses were determined using both Field Emission Scanning Electron Microscope (FE-SEM, Carl ZEISS, FEG, Ultra 55) and Atomic Force Microscope(AFM, Seiko Instruments, SPA- 400 of 3800 probe station, Japan).

### 2.4.1 Field Emission-Scanning Electron Microscopy (FE-SEM)

The Field Emission Gun (FEG) is usually a wire of Tungsten (W) Zigma, Carl Zeiss, Germany, 30kV, Image Resolution-1.3 nm, Energy Resolution~127 eV)fastened on a sharp point. The significance of the small tip radius (~ 100 nm) is that an electric field can be concentrated to an extreme level, becoming so big that the work function of the material is lowered and electrons can leave the cathode. FE-SEM uses FEG to produce a cleaner image, less electrostatic distortions and spatial resolution of even < 2nm which means that the resolution is 3 or 6 times better than that of SEM. The images formed by the field emission scanning electron microscope are formed by the

secondary electrons, backscattered electrons, characteristic X- rays, Auger electrons and others that are emitted by the sample. The FE-SEM images were obtained at an operating voltage of 15 kV and the working distance was about 8.5 mm.

### 2.4.2 Energy dispersive x-ray spectroscopy

In the present study, chemical composition of $Ti_{20}Zr_{20}Cu_{60-x}Ni_x$ (x=10,20,30,40 and 50) metallic glasses were determined through(EDX) analysis. EDX spectrum were obtained using the same FE-SEM, equipped with an EDAX (Oxford Instruments).The operating voltage and working distance for EDX measurement were 15 kV and 8.5 mm, respectively.

### 2.4.3 Atomic Force Microscopy (AFM)

Atomic force microscopy (AFM) is a very high - resolution type of scanning probe microscopy, the resolution obtained by this technique can resolve the single atom and map the real 3- D images of the surface the morphology. In the present case, SPA 400 of SPI 3800 probe station of Seiko Instruments, Japan was used for both contact mode and current mode AFM studies. The topography of $Ti_{20}Zr_{20}Cu_{60-x}Ni_x$ (x=10, 20, 30, 40 and 50) metallic glasses were studied using an AFM probe that touches the surface of a sample with a sharp tip (often less than 100 nm). The spring constant of the cantilever was 2.2 N/m and resonance frequency was 29 KHz. The radius of curvature of the tip was less than 35 nm. When surface morphology and local current are registered simultaneously, a dc voltage of 1V was applied to the bottom electrode prior to scanning. The range of current, which the current preamplifier could measure, was 100 pA to 100 nA. For each metallic glass a new tip was used to avoid artifacts due to tip erosion.

### 2.4.4 Transmission Electron Microscopy (TEM)

The structure and morphology of phase distribution of $Ti20.Zr_{20}.Cu_{60-x}.Ni_x$ (x=10, 20, 30, 40 and 50) metallic glasses were determined using a Transmission electron microscope (Tecnai 20 $G^2$ ST win, FEI, The Netherlands. Operated at 300 kV. The images were captured using a Gatan CCD camera. Final thinning was conducted in a Fishbone ion milling system at 4 kV and 5 mA with ion milling at an angle less than 10°. Liquid nitrogen cooled stage was used. In this work, the amourphouces and monocrystalline samples were prepared with a GATAN polishing ion device at an incident angle of 4 to $5^o$ from the top part and an etching voltage of 4kv.These values were observed to be appropriate and non-structural changes were detected in the major part of our sample .However, in the harder samples (using small voltage and angles) the milling time was quite large.

## 2.5 Mechanical Characterization

### 2.5.1 Nanoindentation

The nano-mechanical properties such as hardness and Young's modulus were determined using a Hysitron Nanomechanical system (Tribo Indentor, 900 series, USA). The machine had depth resolution of 0.04nm and load resolution of 1nN. The thermal drift was kept to <0.5nm/s. The machine had a load range of 1 to 10,000 µN. The Berkovich indenter used in all the nanoindentation experiments had a tip radius of about 120 nm and a semi-apex angle of 65.3°. The samples were indented with a maximum load of 5000µN. The trapezoid load function (which includes the loading, holding and unloading segments) was used to measure the hardness of the ribbons and lap joint samples with a loading rate of $200\mu Ns^{-1}$, segment time of 10s and dwell time of 10s. The details of the grids used for nanohardness evaluation is illustrated in Fig. 2.6.

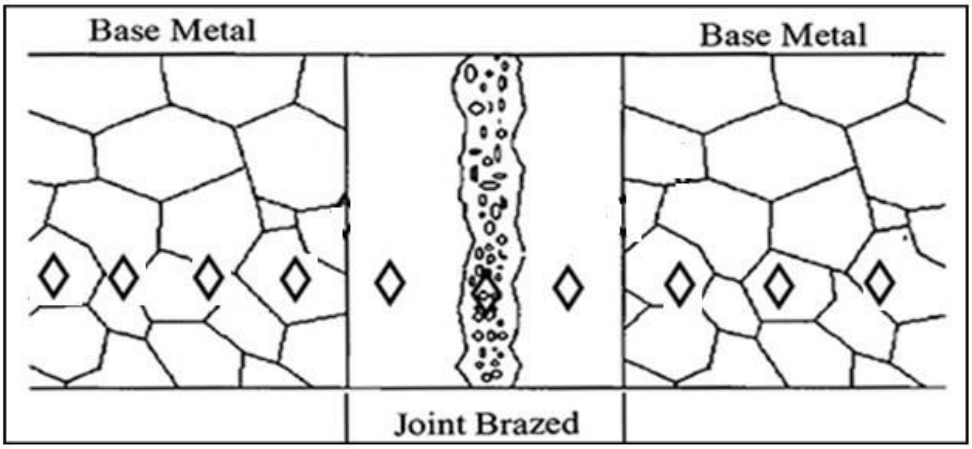


Fig. 2.6 Schematic representation of the profile Nano-hardness testing [7].

### 2.5.2 Tensile Test

Tensile tests of the brazed joints both at room temperature were carried out at a constant speed of 0.5 mm/min by a universal testing machine UTM (INSTRON 5500R). The machine had load cells of 1 and 100kN with an accuracy of ±1% of full scale. The typical tensile specimen is shown in Fig. 2.7. It has enlarged ends or shoulders for gripping. The important part of the specimen is the gage section. The cross-sectional area of the gage section is reduced relative to that of the remainder of the specimen so that deformation and failure will be accure.

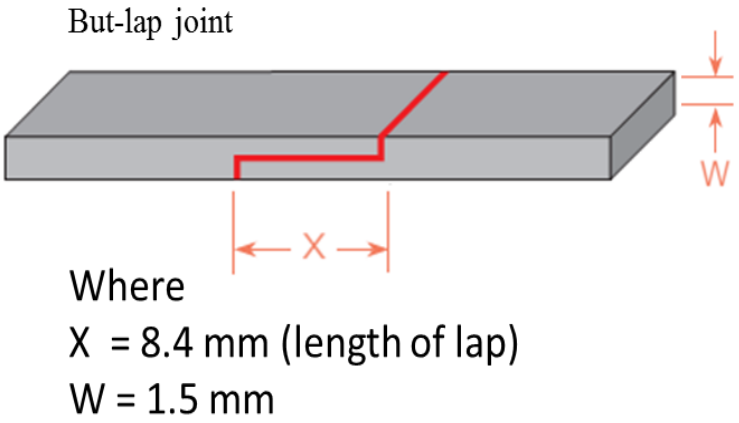


Fig. 2.7 The Butt-Lap Joint for all five samples.

## 2.6 Physical Characterization

### 2.6.1 Electrical Resistivity

The resistivity measurements of $Ti_{20}Zr_{20}Cu_{60-x}Ni_x$ (x=10, 20, 30, 40 and 50) metallic glass ribbons were carried out using an apparatus which employs dc four probe technique. This technique avoids contact resistance. The two outer leads were connected to a constant current source (Model No. 6221, Keithley, USA) and two inner leads were connected to a high impedance nano-voltmeter (Model No. 2182A, Keithley, USA). A chromel-alumel thermocouple was used to measure the sample temperature. The thermocouple was connected to a micro-voltmeter (Model No. 2001, Keithley, USA).

The main purpose of performing resistivity measurements as a function of temperature in this work was to determine the crystallization temperatures of the five metallic glasses and compare these data with the experimental data of corresponding temperatures measured from the DSC measurements.

Accordingly, for $Ti_{20}Zr_{20}Cu_{50}Ni_{10}$, $Ti_{20}Zr_{20}Cu_{40}Ni_{20}$, $Ti_{20}Zr_{20}Cu_{30}Ni_{30}$, $Ti_{20}Zr_{20}Cu_{20}Ni_{40}$ and $Ti_{20}Zr_{20}Cu_{10}Ni_{50}$ metallic glass ribbons in addition to room temperature measurement the resistivity measurements were also carried out from -200 to 600ºC using a homemade set-up and the same chromel-alumel thermocouple as mentioned above.

The data were collected using a Lab view programme. A constant current of 10 mA was passed through each sample using the constant current source as mentioned above. The corresponding voltage was measured using the nano-voltmeter as mentioned above. In order to determine room temperature resistance ($\rho_{RT}$), the resistance at room temperature was measured for each sample about 50 times and the average was taken. Accuracy in determination of resistivity is mainly limited by thickness measurement of the thin melt spun metallic glass ribbons. To improve thickness measurement accuracy,

six pieces of each sample were put together and then total thickness was measured using an imported screw gauge. The variation in thickness was very little from one place to another. The average thicknesses of $Ti_{20}Zr_{20}Cu_{50}Ni_{10}$, $Ti_{20}Zr_{20}Cu_{40}Ni_{20}$, $Ti_{20}Zr_{20}Cu_{30}Ni_{30}$, $Ti_{20}Zr_{20}Cu_{20}Ni_{40}$ and $Ti_{20}Zr_{20}Cu_{10}Ni_{50}$ metallic glass ribbons were respectively measured to be 46, 28, 62, 63 and 36 μm. The estimated accuracy in determining thicknesses was better than 2%. The magnitudes of ($\rho_{RT}$) were determined by using the standard formula [$\rho = R(A/l)$] where A is the cross sectional area and $l$ is the length between voltage terminals. Errors in measurements of length and thickness were absolutely minimized by taking long lengths of about 30 cm and width of at least 2.5 cm.

## References


1. Cullity B. D. and Stock S. R., "Elements of X-Ray Diffraction (3rd Edition)", 2001.
2. http://fys.kuleuven.be/iks/nvsf/experimental-facilities/x-ray-diffraction-2013-bruker-d8-discover
3. Guinier A.,"X-Ray Diffraction: In Crystals, Imperfect Crystals, and Amorphous Bodies (Dover Books on Physics)" 1994.
4. H.E. Kissinger, Anal. Chem. 29, 1702 (1957).
5. J.A. Augis, J.E. Bennett, J.Therm, Anal Color 13, 283(1978).
6. T. Ozawa, Polymer 12, 150(1971).
7. W.C. Oliver, G.M. Pharr, Measurement of Hardness and Elastic Modulus by Instrumented Indentation: Advances in Understanding and Refinements to Methodology, J. Mater. Res. 19 (2004) 3-20.
8. E. Ganjeh et al. Materials and Design 39, 33–41 (2012)

# Chapter 3

## Results and Discussion

## Structural Characterization and Thermal Properties of Ti-Zr-Cu-Ni metallic glasses

### 3.1 Introduction:

Since metallic glasses are in metastable state, it is important to know their thermal behaviour and crystallization process since on thermal treatment and crystallization their properties change. In this chapter, the studies on structural, microstructural and crystallization studies of $Ti_{20}Zr_{20}Cu_{60-x}Ni_x$ (x = 10, 20, 30, 40 and 50) metallic glasses are presented and discussed.

### 3.2.1 Results and Discussion

### 3.2.2 Structure

The XRD spectrum of all samples, shown in Fig. 3.1, revealed amorphous nature with a characteristic broad hump. It is seen from Table 3.2 that all the XRD peaks are between 41 and 40.5$^o$ [4]. The corresponding full width at half maxima (FWHM) are also given in Table 3.2, which indicates that the short-range order is nearly the same for each sample as FWHM of peaks are nearly the same. The FWHM of x =10 sample is slightly higher indicating short-range order smaller in this sample when compared to other samples.

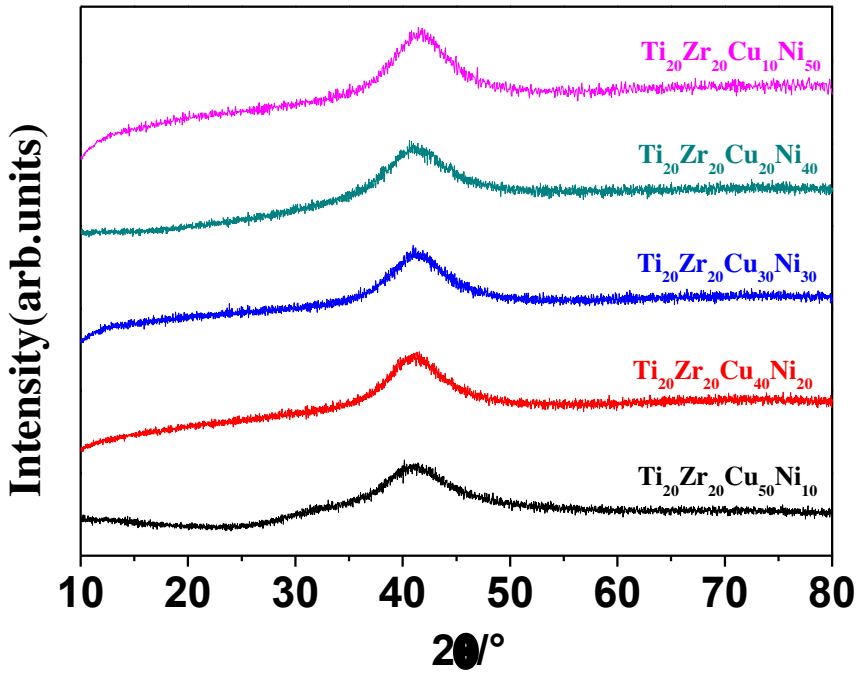


Fig.3.1The XRD pattern of the $Ti_{20}Zr_{20}Cu_{60-x}Ni_x$ (x= 10,20,30,40 and 50) metallic glasses.

Table 3.2 FWHM of $Ti_{20}Zr_{20}Cu_{60-x}Ni_x$ (x= 10,20,30,40 and 50) metallic glasses.

| Composition | Peak(2θ°) | FWHM | Height (counts) | Adj.R-Square |
|---|---|---|---|---|
| $Ti_{20}Zr_{20}Cu_{50}Ni_{10}$ | 40.96 | 10.6 | 770.53 | 0.80237 |
| $Ti_{20}Zr_{20}Cu_{40}Ni_{20}$ | 40.96 | 7.7 | 874.41 | 0.50124 |
| $Ti_{20}Zr_{20}Cu_{30}Ni_{30}$ | 41.28 | 7.4 | 839.53 | 0.57129 |
| $Ti_{20}Zr_{20}Cu_{20}Ni_{40}$ | 41.30 | 8.7 | 869.67 | 0.40583 |
| $Ti_{20}Zr_{20}Cu_{10}Ni_{50}$ | 41.30 | 7.7 | 1091.80 | 0.48907 |

### 3.3 Thermal Analysis

All the samples were run on DSC to study their crystallization. The following sections present these results. Non-isothermal mode was used for the runs.

#### 3.3.1 $Ti_{20}Zr_{20}Cu_{50}Ni_{10}$ Metallic glass

Fig. 3 shows the DSC curves for$Ti_{20}Zr_{20}Cu_{50}Ni_{10}$ metallic glasses. The heating rates of 10, 20, 30 and 40 K/min were maintained during the non-isothermal runs. The state of the transformation has been taken as the point where the base line was deviated from linearity [5, 6]. There were two characteristic temperatures involved. The temperature

at which the onset of the crystallization process initiates is denoted by $T_x$ while the peak temperature is denoted by $T_p$. For all the heating rates, both two temperatures, mentioned above, were identified clearly as shown in Figures.3.2.. Both $T_x$ and $T_p$ increased with the increase of heating rates as observed normally (*cf.*, Fig.3.2 and Table 3.3).

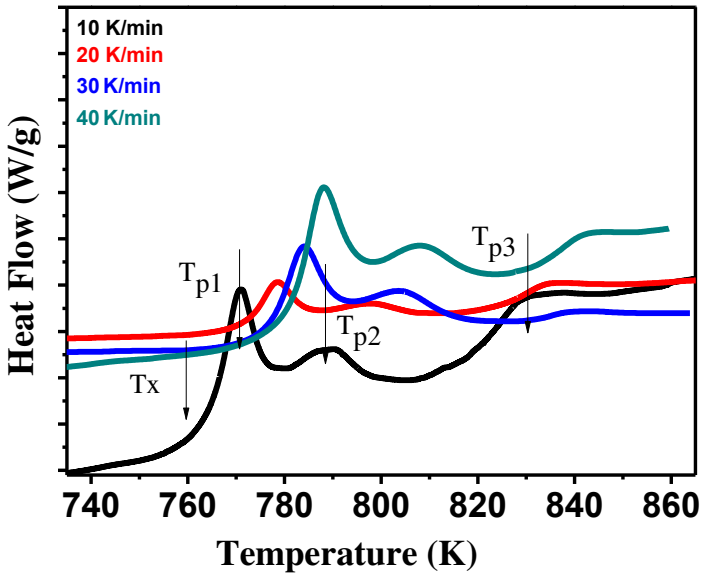


Fig.3.2: The DSC curves of $Ti_{20}Zr_{20}Cu_{50}Ni_{10}$ metallic glass at various heating rates.

Table 3.3: The Variation of exothermic peaks of $Ti_{20}Zr_{20}Cu_{50}Ni_{10}$ metallic glass as a function of heating rates.

| **Heating Rate (K/Min)** | **$Ti_{20}Zr_{20}Cu_{50}Ni_{10}$** | | | |
|---|---|---|---|---|
| | **$T_x$/K** | **$T_{p1}$/K** | **$T_{p2}$/K** | **$T_{p3}$/K** |
| 10 | 755 | 771 | 789 | 831 |
| 20 | 771 | 778 | 798 | 835 |
| 30 | 775 | 784 | 803 | 840 |
| 40 | 780 | 788 | 807 | 842 |

For this sample three stages crystallization processes were observed for all the four heating rates**.** The peak areas in these plots increased with heating rates. This was expected because of the heating rate enhanced the reaction rates and thereby the rate of change of enthalpy takes place as a function of temperature $\left(\frac{dH}{dT}\right)$ [7]. The magnitude of

$T_x$ (the crystallization initiation temperature) was 755 K at 10 K/min heating rate, whereas the magnitudes of $T_{p1}$, $T_{p2}$ and $T_{p3}$ were 771, 789 and 831K, respectively. $T_x$ was found to be 771 K at 20 k/min, whereas at the above heat rate the magnitudes of $T_{p1}$, $T_{p2}$ and $T_{p3}$ were 778, 789 and 835K. Similarly, the $T_x$ was found to be 775 K at 30 K/min and the respective magnitudes of $T_{p1}$, $T_{p2}$ and $T_{p3}$ were 784, 803 and 840K. In an analogous manner, for the heating rate of 40 K/min, the magnitude of $T_x$ was 780K and the respective magnitudes of $T_{p1}$, $T_{p2}$ and $T_{p3}$ were 788, 807 and 842K. The first and second peaks are obtained due to the crystallization at low and high temperatures, respectively. It is interesting to note that the third peak although is very small it shifts toward higher temperature as heating rate increases. Analysis of the growth process of the first peak in Fig. 3.2 appeared to suggest that possibly there was a relatively slower initial rise in the activation energy (E) requirement, which subsequently rises as the temperature increase. This observation may indicate that the second crystallization step had started even before the first step was completed. These factors are discussed one by one. It may be possible that the crystal of nature produced during the first crystallization was considered to be metastable. Hence, it may be argued that the increase in temperature, these metastable materials was transformed into new structure [8-10]. There may be another possibility that this metallic glass of multicomponent nature has not crystallize in single step. If this conjecture is true then the crystal which remained within the melt might have had a different composition and therefore, it might be possible that it had crystallized with slower rate to obtain another phase at high temperature. The first crystallization event took place with the appearance of a sharp peak due to the formation of nuclei at higher rate, whereas it was found to be broad for the second peak where the growth process obtained very slowly. The third peak is really very broad.

### 3.3.2 $Ti_{20}Zr_{20}Cu_{40}Ni_{20}$ Metallic glass

Fig. 3.3 shows the DSC curves for $Ti_{20}Zr_{20}Cu_{40}Ni_{20}$ metallic glass for the four heating rates. The experimental conditions and parameter were exactly the same mentioned in earlier section (3.3.1). The single stage crystallization process was observed in all the heating rates. The peak areas in these plots increased with heating rates. This was expected because the rate of the reaction increased with increase of heating rate, and hence, the rate of change of enthalpy as a function of temperature$\left(\frac{dH}{dT}\right)$. Table 3.4 gives the values of $T_x$ and $T_p$ for the heating rates of 10, 20, 30 and 40 K/min as (756 and 764 K), (768 and 773 K), (770 and 779 K) and (772 and 783 K), respectively.

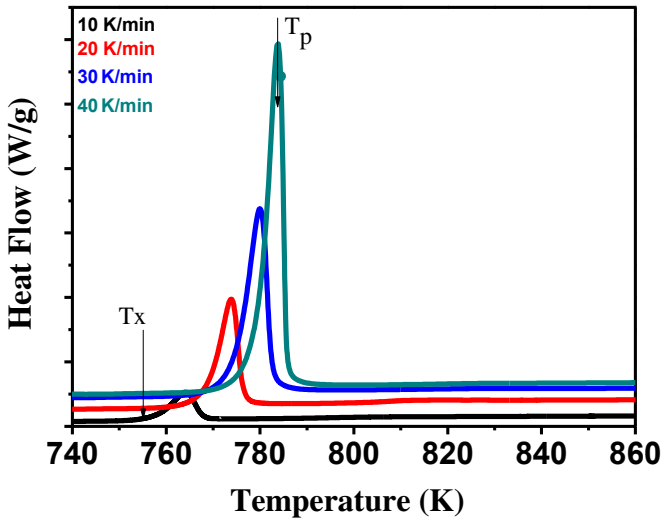


Fig.3.3: DSC curves of $Ti_{20}Zr_{20}Cu_{40}Ni_{20}$ metallic glass at various heating rates.

Table 3.4: The Variation of exothermic peaks of $Ti_{20}Zr_{20}Cu_{40}Ni_{20}$ metallic glass as a function of heating rates.

| Heating Rates (K/Min) | $Ti_{20}Zr_{20}Cu_{40}Ni_{20}$ | |
|---|---|---|
| | $T_x$(K) | $T_p$(K) |
| 10 | 756 | 764 |
| 20 | 768 | 773 |
| 30 | 770 | 779 |
| 40 | 772 | 783 |

### 3.3.3 $Ti_{20}Zr_{20}Cu_{30}Ni_{30}$ Metallic glass

The DSC curves for $Ti_{20}Zr_{20}Cu_{30}Ni_{30}$ metallic glasses are shown in Fig.3.4, The experimental conditions and parameter were kept the same as mentioned in Section 3.3.1. The peak areas in these plots increased with heating rates as in the previous sample.

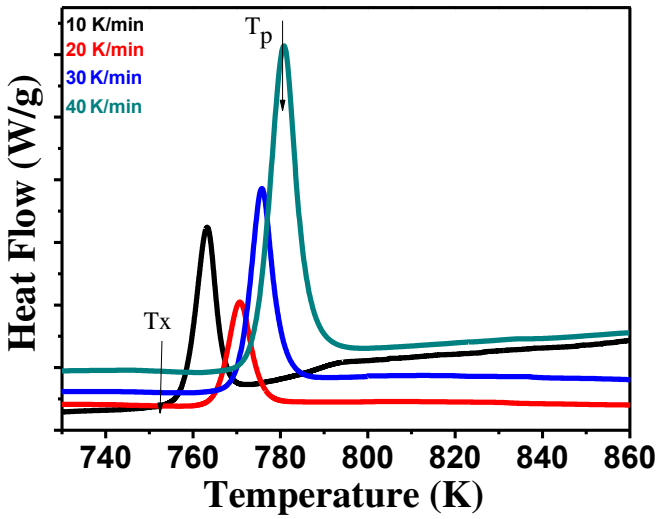


Fig 3.4: DSC curves of $Ti_{20}Zr_{20}Cu_{30}Ni_{30}$ metallic glass at various heating rates.

Table 3.5: $T_x$ and $T_p$ values for $Ti_{20}Zr_{20}Cu_{30}Ni_{30}$ metallic glass as a function of heating rates.

| Heating Rate(K/Min) | $Ti_{20}Zr_{20}Cu_{30}Ni_{30}$ | |
|---|---|---|
| | $T_x$(K) | $T_p$(K) |
| 10 | 757 | 763 |
| 20 | 764 | 770 |
| 30 | 767 | 775 |
| 40 | 771 | 780 |

The magnitudes of ($T_x$ and $T_p$) were found to be (755 and 763 K), (764 and 770 K), (767 and 775 K) and (771 and 780 K), for the heating rates of 10, 20, 30 and 40K/min, respectively as shown in Fig.3.4 and Table 3.5. The pattern of $\left(\frac{dH}{dT}\right)$ is also the same as $Ti_{20}Zr_{20}Cu_{40}Ni_{20}$ metallic glass.

### 3.3.4 $Ti_{20}Zr_{20}Cu_{20}Ni_{40}$ Metallic glass

The magnitudes of $T_x$ and $T_p$ **are** given as (778 and 785K), (785 and 793K), (791 and 798K) and (795 and 802K), shown in Fig. 3.5 and listed in Table 3.6, for the heating rates of 10, 20, 30 and 40 K/min, respectively for the $Ti_{20}Zr_{20}Cu_{20}Ni_{40}$ metallic glass.

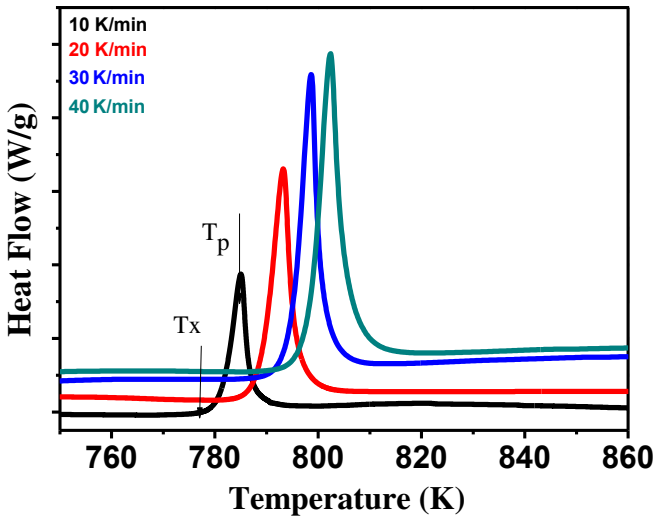


Fig 3.5: DSC curves of $Ti_{20}Zr_{20}Cu_{20}Ni_{40}$ metallic glass at various heating rates.

Table 3.6: $T_x$ and $T_p$ values for $Ti_{20}Zr_{20}Cu_{20}Ni_{40}$ metallic glass as a function of heating rates

| Heating Rate(K/Min) | $Ti_{20}Zr_{20}Cu_{20}Ni_{40}$ | |
|---|---|---|
| | $T_x$(K) | $T_p$(K) |
| 10 | 778 | 785 |
| 20 | 785 | 793 |
| 30 | 791 | 798 |
| 40 | 795 | 802 |

### 3.3.5 $Ti_{20}Zr_{20}Cu_{10}Ni_{50}$ Metallic glass

The magnitudes of the ~~above~~ parameters $T_x$ and $T_p$ are found to be (778 and 784 K), (795 and 802 K), (801 and 808 K) and (805 and 812 K) for the heating rates 10, 20, 30 and 40 K/min, respectively, shown in Fig 3.6 and given in Table 3.7. The behaviours of $\left(\frac{dH}{dT}\right)$, for all the metallic glasses are the same.

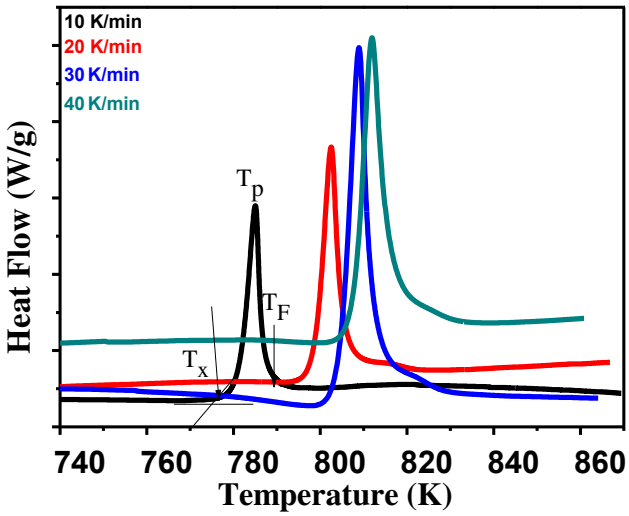


Fig 3.6: DSC curves of $Ti_{20}Zr_{20}Cu_{10}Ni_{50}$ metallic glass at various heating rates.

Table 3.7: $T_x$ and $T_p$ values for $Ti_{20}Zr_{20}Cu_{10}Ni_{50}$ metallic glass as a function of heating rates

| Heating Rate (K/Min) | $Ti_{20}Zr_{20}Cu_{10}Ni_{50}$ | |
|---|---|---|
| | $T_x$(K) | $T_P$(K) |
| 10 | 778 | 784 |
| 20 | 795 | 802 |
| 30 | 801 | 808 |
| 40 | 805 | 812 |

### 3.4 The kinetics of crystallization

Kissinger (1956) procedure was used to evaluate average activation energy, E. The details of Kissinger procedure is as follows. The basic equation that relates the rate of reaction to the fraction of the materials decomposed may be written as (Murray et al 1949 and Vaughan 1955)

$$\left(\frac{dx}{dt}\right)T = \mathrm{KT}(1-X) \qquad (1)$$

Where, x is the fraction of the materials decomposed, $K_T$is the magnitude of the rate constant and is given by the Arrhenius equation

$$KT = A\, e^{-\frac{E}{RT}}$$

Where, A and E are the frequency factor and activation energy respectively. Here, A is a measurement of the probability that a molecule will participate in a reaction and E is energy barrier opposing the reaction (Kissinger 1956) [1].By applying the condition that the reaction rate is maximumsuch that its derivation with respect to time is zero, one can obtain a final equation of the form (Chen 1978 and 1981)

$$\frac{E}{KBT_p} = Ln\left[\frac{T_p^2}{\emptyset}\right] + constant \ldots\ldots\ldots\ldots\ldots 3$$

Where,$T_p$ is the peak temperature, Φ is the heating rate and $K_B$ is the Boltzmann constant.InaLn ($\Phi/T^2p$) vs.1/Tp plot the slope will give the quantity (E/KB).

The activation energy of the crystallization event was determined by an approximation method proposed by Augis and Bennett (1978)[2]. Their approach showed a linear relation between ($ln\ \Phi/T_p$ ) and ($1/T_p$) while linear relation between ($ln\Phi/T^2_p$ ) and ($1/T_p$) was considered for the Kissinger model. The Augis and Bennett modelis described by the following equation [2]

$$Ln(\frac{\Phi}{T_p}) = -\frac{E_c}{RT_p} + Ln(K_0) \qquad (4)$$

Where, the pre-exponential term $K_0$ is the frequency factor.

Moreover, another model proposed by Ozawa (1965) [3] was also used to estimate the activation energy during crystallization. This model describes a linear relation between ($Ln\ \Phi$) and ($1/T_p$) unlike Kissinger equation or Augis-Bennett model. The Ozawa model is described as:

$$Ln(\Phi) = -\frac{E_c}{RT_p} + const \qquad (5)$$

The slope of Ln (Φ) versus (1000/$T_p$) plot will give the magnitude of ($E/K_B$).

### 3.4.1 Kissinger Model

Generally, Kissinger model [1, 20] is most commonly used to estimate the activation energy and glass transition temperature, which describes the dependence of peak temperature on heating rate for a particular transition. Using the following Kissinger equation (1), the activation was calculated where the crystallization peak temperature ($T_p$) obtained from DSC thermograms (*cf.,* Figs 3.2-3.6) [1, 20]:

$$Ln(\frac{\Phi}{T_p^2}) = -(\frac{E_c}{RT_p}) + const., \ldots\ldots\ldots\ldots\ldots\ldots\ldots\ldots (1)$$

Thus, the experimental data were best fitted to Equation (1) as shown in Fig. 3.8. The activation energies for crystallizations in the different metallic glass systems were evaluated from the slopes of these best fitted lines from the respective plots of L*n* ($\Phi/T^2_p$) versus ($1000/T_p$) as shown in Fig. 3.7. The activation energies calculated at 90% fraction of crystallization for Kissinger model [1, 20] for the crystallization is presented in Table 8. For $Ti_{20}Zr_{20}Cu_{50}Ni_{10}$ metallic glasses the activation energies for the 1st, 2nd and 3rdpeaks were evaluated to be 395, 396 and 681KJ/mole, respectively.

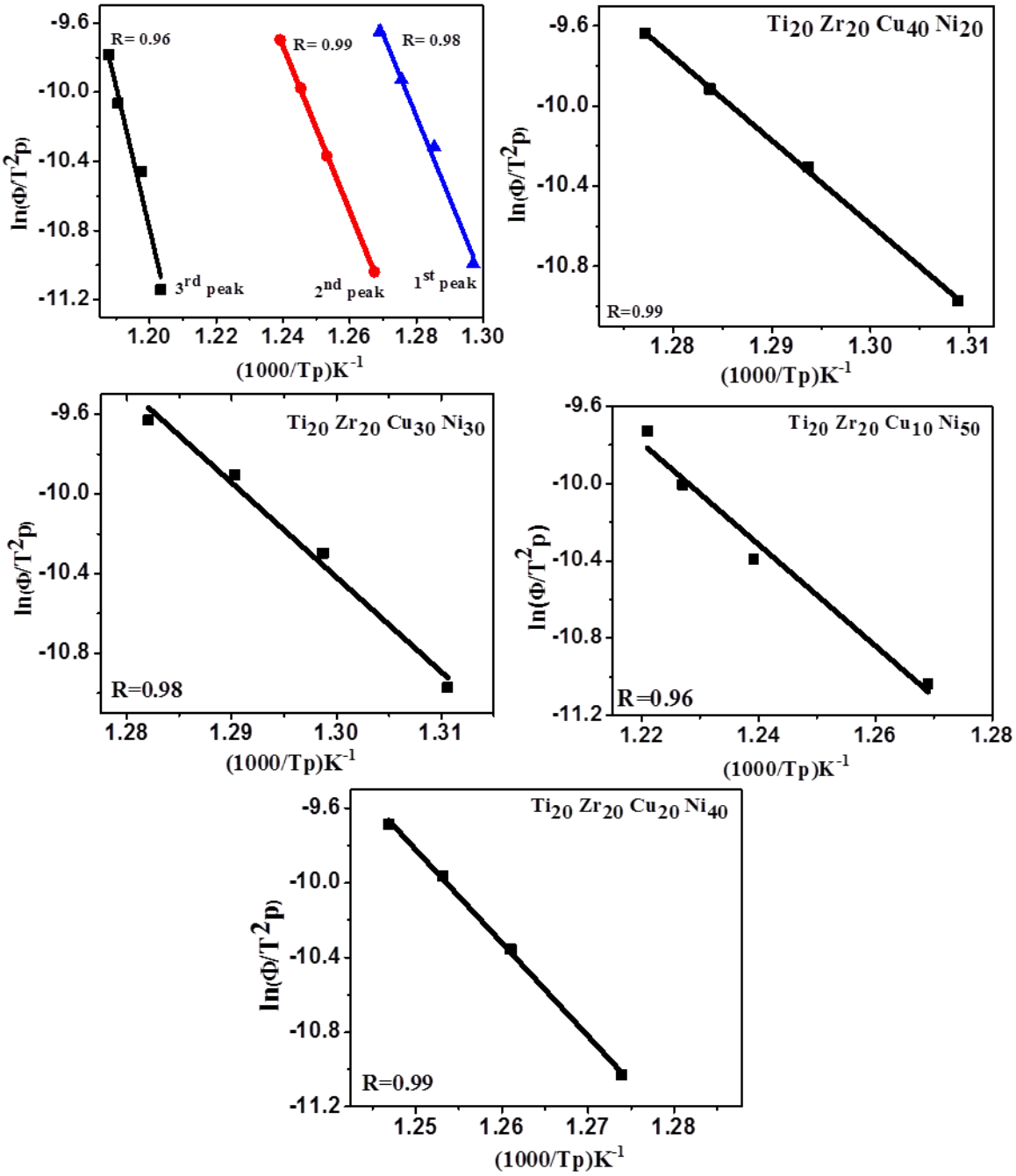


Fig. 3.7: Ln ($\Phi/T_p^2$) versus ($1000/T_p$) of $Ti_{20}$-$Zr_{20}$-$Cu_{60-x}$-$Ni_x$ (x = 10, 20, 30, 40 and 50) metallic glasses for 3 peaks of x =10 sample and one peak for other samples.

Table 3.8: Activation energies ($E_c$) for crystallization of the $Ti_{20}$-$Zr_{20}$-$Cu_{60-x}$-$Ni_x$ (x= 10, 20, 30, 40 and 50) metallic glasses (from Kissinger Model [20]).

| **Composition** | ***Ec* (KJ/mol) for Crystallization process using Kissinger method** | | |
|---|---|---|---|
| | **1st Peak** | **2nd Peak** | **3nd Peak** |
| $Ti_{20}Zr_{20}Cu_{50}Ni_{10}$ | 395 | 396 | 681 |
| $Ti_{20}Zr_{20}Cu_{40}Ni_{20}$ | 349 | -- | -- |
| $Ti_{20}Zr_{20}Cu_{30}Ni_{30}$ | 394 | -- | -- |
| $Ti_{20}Zr_{20}Cu_{20}Ni_{40}$ | 416 | -- | -- |
| $Ti_{20}Zr_{20}Cu_{10}Ni_{50}$ | 218 | -- | -- |

### 3.4.2 Augis and Bennett Model

This model is described by the following equation (2):

$$Ln(\frac{\Phi}{T_p}) = -(\frac{E_c}{RT_p}) + Ln(K_0) \ldots\ldots\ldots\ldots (2)$$

where, the pre-exponential $K_0$ is the frequency factor.

Thus, the experimental data were best fitted to Equation (2) as shown in Fig. 3.8. The activation energies for crystallizations in the different metallic glass systems were evaluated from the slopes of these best fitted lines as shown in Fig. 3.8. Using Augis and Bennett model [2, 20], the activation energies of crystallization are calculated which are given in Table 3.9. The corresponding activation energies for the 1st, 2nd and 3rd peaks were found to be 401, 403 and 688 KJ/mole, respectively, for $Ti_{20}Zr_{20}Cu_{50}Ni_{10}$ metallic glass.

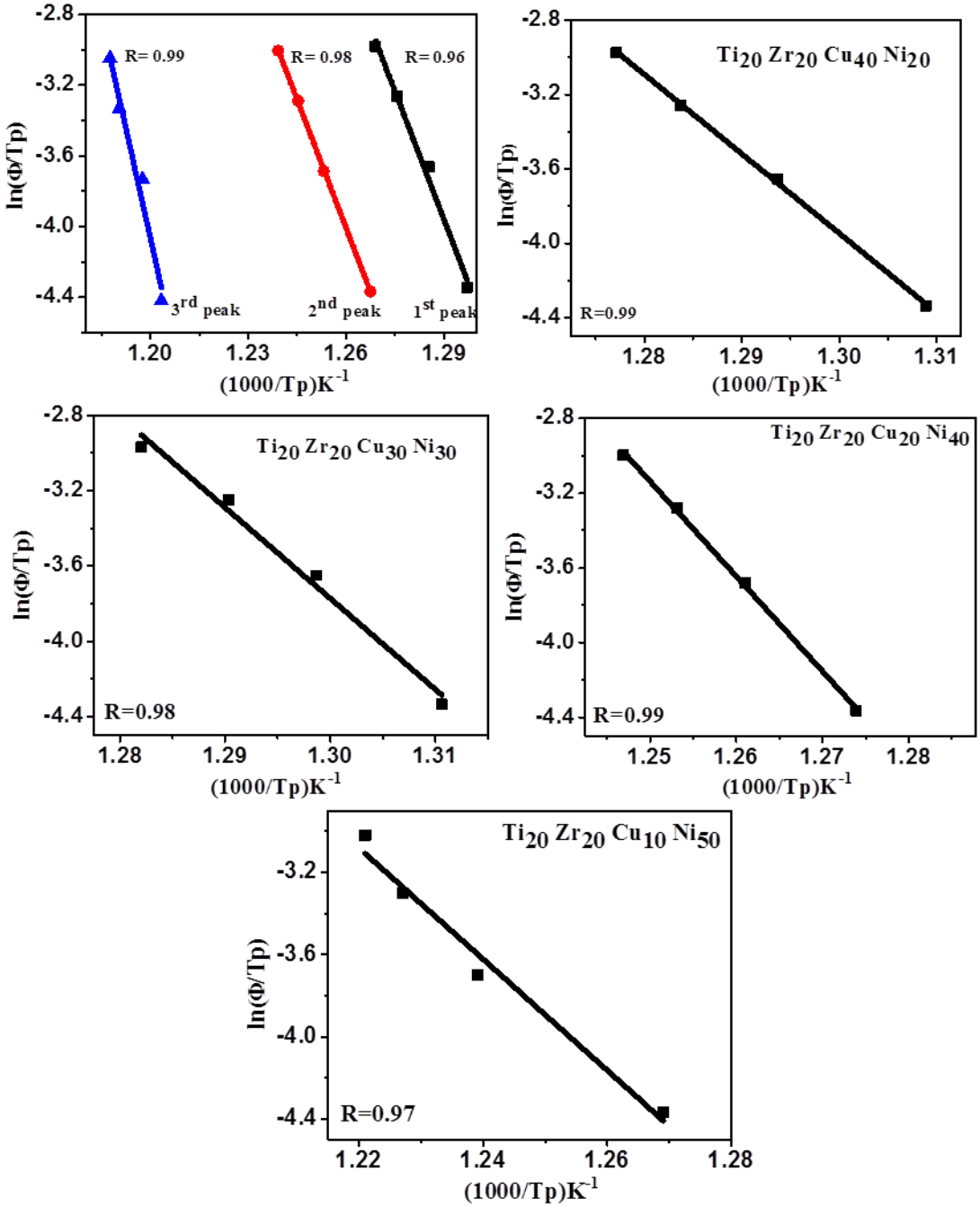


Fig. 3.8: *Ln(Φ/$T_p$)* versus *(1000/$T_p$)*of $Ti_{20}$-$Zr_{20}$-$Cu_{60-x}$-$Ni_x$ (x = 10, 20, 30, 40 and 50) metallic glasses.

Table. 3.9 Activation energies ($E_c$) for crystallization of the $Ti_{20}Zr_{20}Cu_{60-x}Ni_x$ (x= 10, 20, 30, 40 and 50) metallic glasses (from Augis and Bennett Model [21]).

| **Composition** | ***Ec* (KJ/mol) for Crystallization process using Augis& Bennett method** | | |
|---|---|---|---|
| | **1st Peak** | **2nd Peak** | **3nd Peak** |
| $Ti_{20}Zr_{20}Cu_{50}Ni_{10}$ | 401 | 403 | 688 |
| $Ti_{20}Zr_{20}Cu_{40}Ni_{20}$ | 355 | -- | -- |
| $Ti_{20}Zr_{20}Cu_{30}Ni_{30}$ | 401 | -- | -- |
| $Ti_{20}Zr_{20}Cu_{20}Ni_{40}$ | 422 | -- | -- |
| $Ti_{20}Zr_{20}Cu_{10}Ni_{50}$ | 225 | -- | -- |

### 3.4.3 Ozawa Model

This model is described by the following equation (3):

$$Ln(\Phi) = -(\frac{E_c}{RT_p}) + const \qquad (3)$$

Thus, the experimental data were best fitted to Equation (3) as shown in Fig. 3.9. The activation energies for crystallizations in the different for metallic glass systems (different x values) were evaluated from the slopes of these best fitted lines as shown in Fig. 3.9. The activation energies calculated for Ozawa Model [3, 21] for the crystallization are presented in Table 3.10. For $Ti_{20}Zr_{20}Cu_{50}Ni_{10}$ metallic glasses the activation energies for the 1st, 2nd and 3rd peaks were evaluated to be 408, 409 and 695 KJ/mole, respectively.

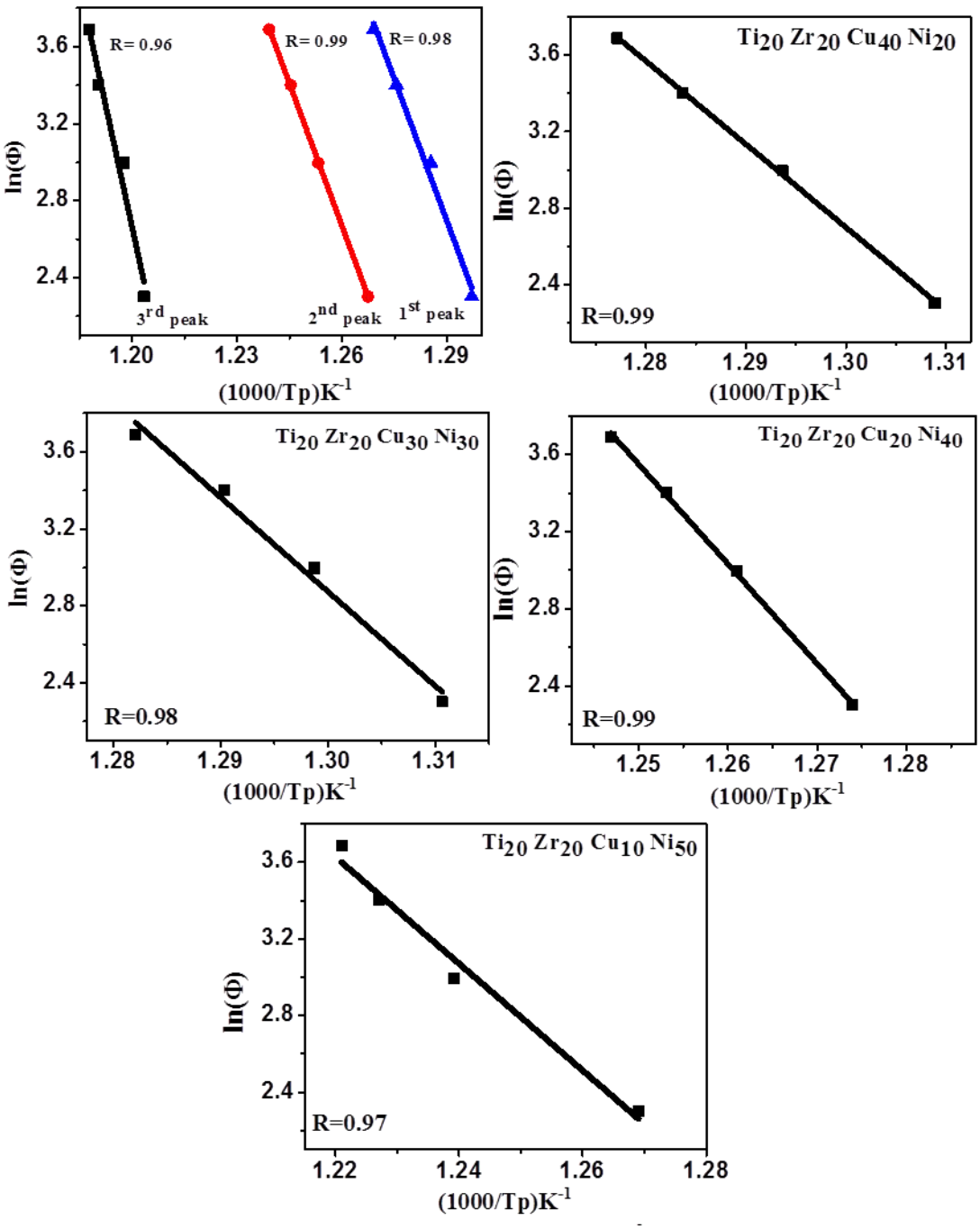


Fig .3.9 The 1st, 2nd and 3rd crystallization events determined from the plots of Plots of L*n* (Φ) versus *(1000/$T_p$)* of $Ti_{20}Zr_{20}Cu_{60-x}Ni_x$ (x= 10, 20, 30, 40 and 50) metallic glasses.

Table. 3.10 The Ec for $Ti_{20}Zr_{20}Cu_{60-x}Ni_x$ (x= 10, 20, 30, 40 and 50) metallic glasses (from Ozawa Model [22]).

| Composition | *Ec* (KJ/mol) for Crystallization process using Ozawa Method | | |
|---|---|---|---|
| | 1st Peak | 2nd Peak | 3nd Peak |
| $Ti_{20}Zr_{20}Cu_{50}Ni_{10}$ | 408 | 410 | 695 |
| $Ti_{20}Zr_{20}Cu_{40}Ni_{20}$ | 361 | -- | -- |
| $Ti_{20}Zr_{20}Cu_{30}Ni_{30}$ | 407 | -- | -- |
| $Ti_{20}Zr_{20}Cu_{20}Ni_{40}$ | 429 | -- | -- |
| $Ti_{20}Zr_{20}Cu_{10}Ni_{50}$ | 232 | -- | -- |

Looking at the activation energies, it is observed for the first peak of x = 10 sample it is higher than x =20 sample in all the three models. It is also observed that all the three models give nearly the same (within a few percent) activation energy for a given sample. Therefore, it looks like that one can use any of these three models. However, Kissinger model has been widely used for calculating activation energies of metallic glasses.

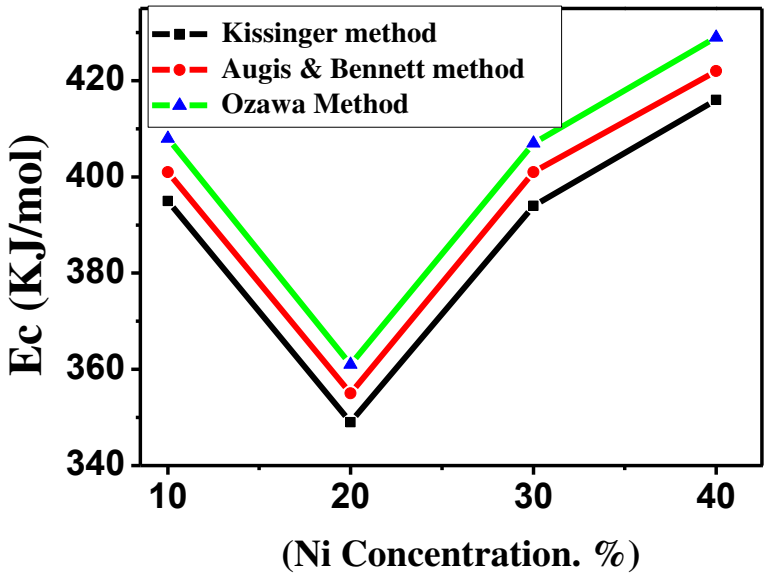


Figure 3.10 Plot $E_c$ values for the first peak obtained by various methods vs Ni Concentration %).

Figure 3.10 shows activation energy plot vs. Ni concentration. It is observed that for x = 20 to x = 40, it is almost linear. Of course, the activation energy for x =10 does not fall on this straight line behaviour [15]. The sample (x = 10) certainly behaves differently than other samples as it has three crystallization peaks while other samples have only one peak. One may have to look at the microstructure of these samples more carefully to figure out the reason for this deviation.

### 3.5 FESEM Analysis of Microstructures of $Ti_{20}Zr_{20}Cu_{60-x}Ni_x$ (x= 10, 20, 30, 40 and 50) metallic glasses

#### 3.5.1 Surface studies of $Ti_{20}Zr_{20}Cu_{50}Ni_{10}$ Metallic glass

FESEM has been used to study surface topography of the $Ti_{20}Zr_{20}Cu_{60-x}Ni_x$ (x= 10, 20, 30, 40 and 50) metallic glasses. Figure 3.11 (a) shows the microstructure of the $Ti_{20}Zr_{20}Cu_{50}Ni_{10}$ metallic glass ribbon. The corresponding EDX data along with the typical elemental composition are shown in Figure 3.11 (b). The metallic glass ribbon looked reasonably smooth without the sign of crystallites on the surface as shown in Figure 3.11 (a). The data from Figure 3.11 (b) confirmed that the (at %) presence of different elements followed almost the nominal composition of $Ti_{20}Zr_{20}Cu_{50}Ni_{10}$ metallic glass ribbon within the limits of typical experimental error [12-14]. Similar observations have also been made for other four remaining metallic glass ribbons (see Figs.3.12-3.15), as in the case of $Ti_{20}Zr_{20}Cu_{50}Ni_{10}$ metallic glass.

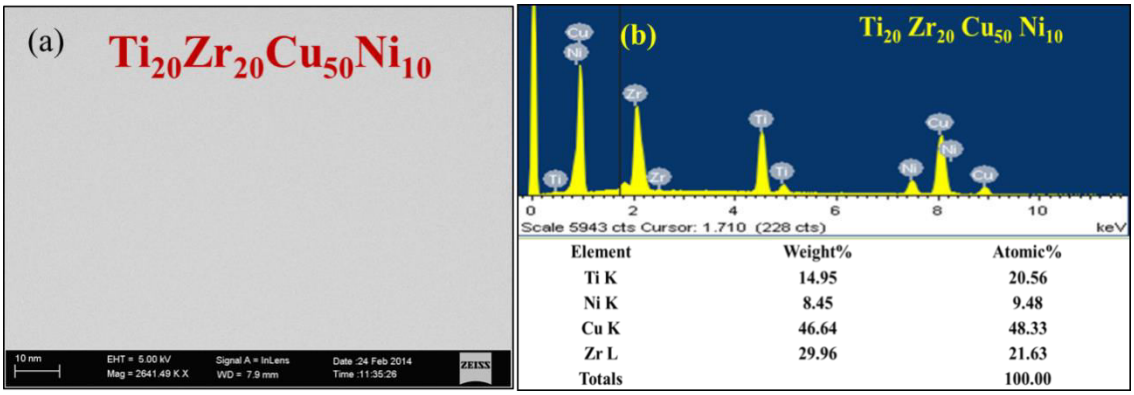


| Element | Weight% | Atomic% |
|---|---|---|
| Ti K | 14.95 | 20.56 |
| Ni K | 8.45 | 9.48 |
| Cu K | 46.64 | 48.33 |
| Zr L | 29.96 | 21.63 |
| Totals | | 100.00 |

Fig. 3.11: FESEM studies on $Ti_{20}Zr_{20}Cu_{50}Ni_{10}$metallic glass (a) Surface morphology and (b) Average (at.%) chemical compositions by EDX.

### 3.5.2Surface studies of$Ti_{20}Zr_{20}Cu_{40}Ni_{20}$ Metallic glass

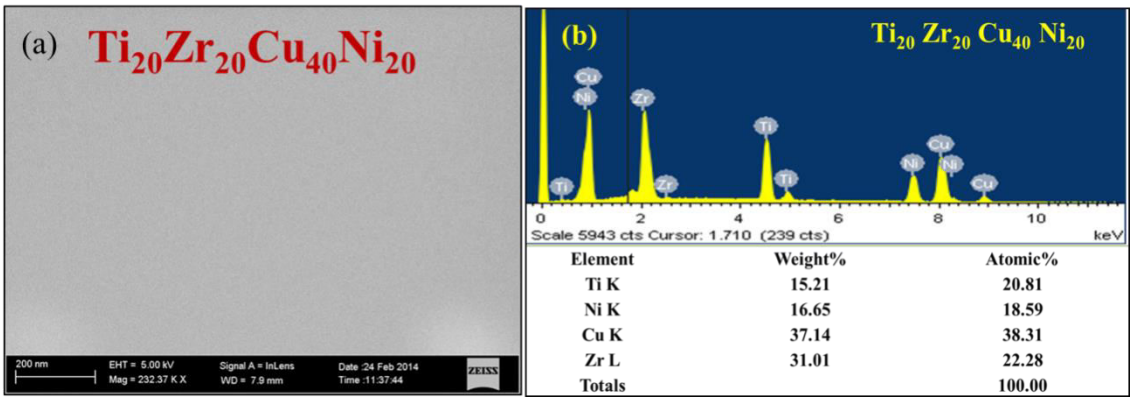


| Element | Weight% | Atomic% |
|---|---|---|
| Ti K | 15.21 | 20.81 |
| Ni K | 16.65 | 18.59 |
| Cu K | 37.14 | 38.31 |
| Zr L | 31.01 | 22.28 |
| Totals | | 100.00 |

Fig. 3.12: FESEM studies on $Ti_{20}Zr_{20}Cu_{40}Ni_{20}$metallic glass ribbon (a) Surface morphology and (b) Average (at.%) chemical compositions by EDX.

### 3.5.3 Surface studies of$Ti_{20}Zr_{20}Cu_{30}Ni_{30}$ Metallic glass

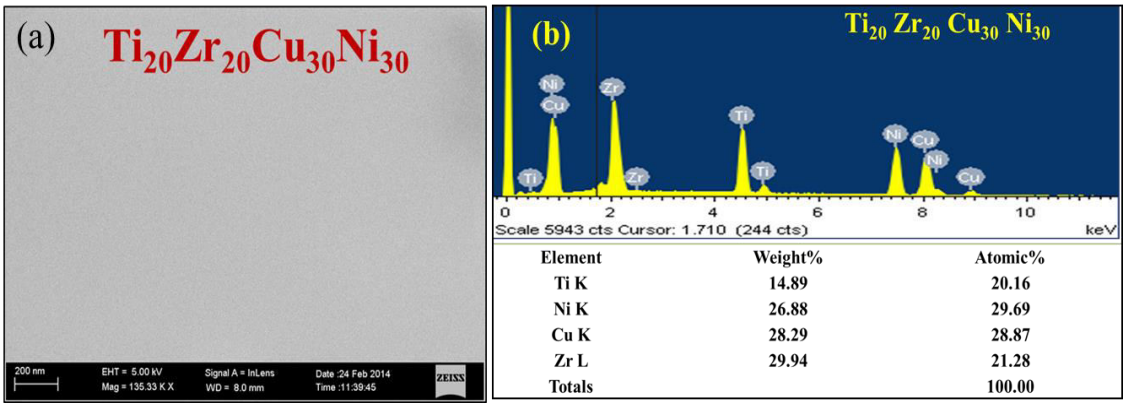


| Element | Weight% | Atomic% |
|---|---|---|
| Ti K | 14.89 | 20.16 |
| Ni K | 26.88 | 29.69 |
| Cu K | 28.29 | 28.87 |
| Zr L | 29.94 | 21.28 |
| Totals | | 100.00 |

Fig. 3.13: FESEM studies on $Ti_{20}Zr_{20}Cu_{30}Ni_{30}$metallic glass ribbon (a) Surface morphology and (b) Average (at.%) chemical compositions by EDX.

### 3.5.4 Surface studies of$Ti_{20}Zr_{20}Cu_{20}Ni_{40}$ Metallic glass

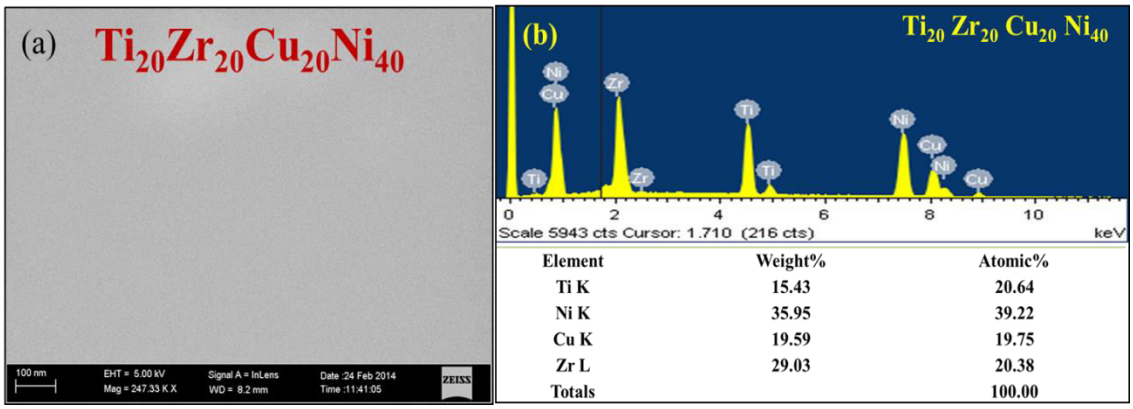


| Element | Weight% | Atomic% |
|---|---|---|
| Ti K | 15.43 | 20.64 |
| Ni K | 35.95 | 39.22 |
| Cu K | 19.59 | 19.75 |
| Zr L | 29.03 | 20.38 |
| Totals | | 100.00 |

Fig. 3.14 FESEM studies on $Ti_{20}Zr_{20}Cu_{20}Ni_{40}$metallic glass ribbon (a) Surface morphology and (b) Average (at.%) chemical compositions by EDX.

### 3.5.5 Surface studies of$Ti_{20}Zr_{20}Cu_{10}Ni_{50}$ Metallic glass

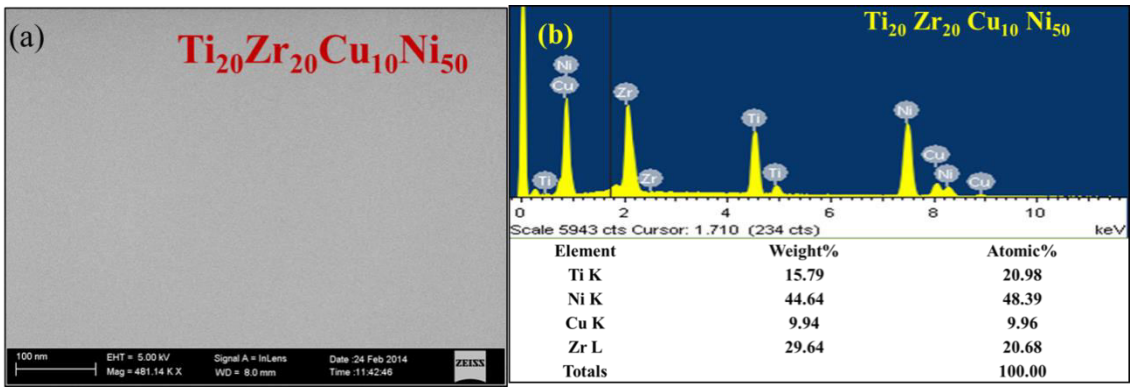


| Element | Weight% | Atomic% |
|---|---|---|
| Ti K | 15.79 | 20.98 |
| Ni K | 44.64 | 48.39 |
| Cu K | 9.94 | 9.96 |
| Zr L | 29.64 | 20.68 |
| Totals | | 100.00 |

Fig. 3.15: FESEM studies on $Ti_{20}Zr_{20}Cu_{10}Ni_{50}$metallic glass ribbon (a) Surface morphology and (b) Average (at.%) chemical compositions by EDX.

### 3.6 AFM

AFM measurements were carried out to determine the surfaces, that is, shiny side (S) and dull side (D). These results are shown below.

#### 3.6.1 Surface topography and roughness

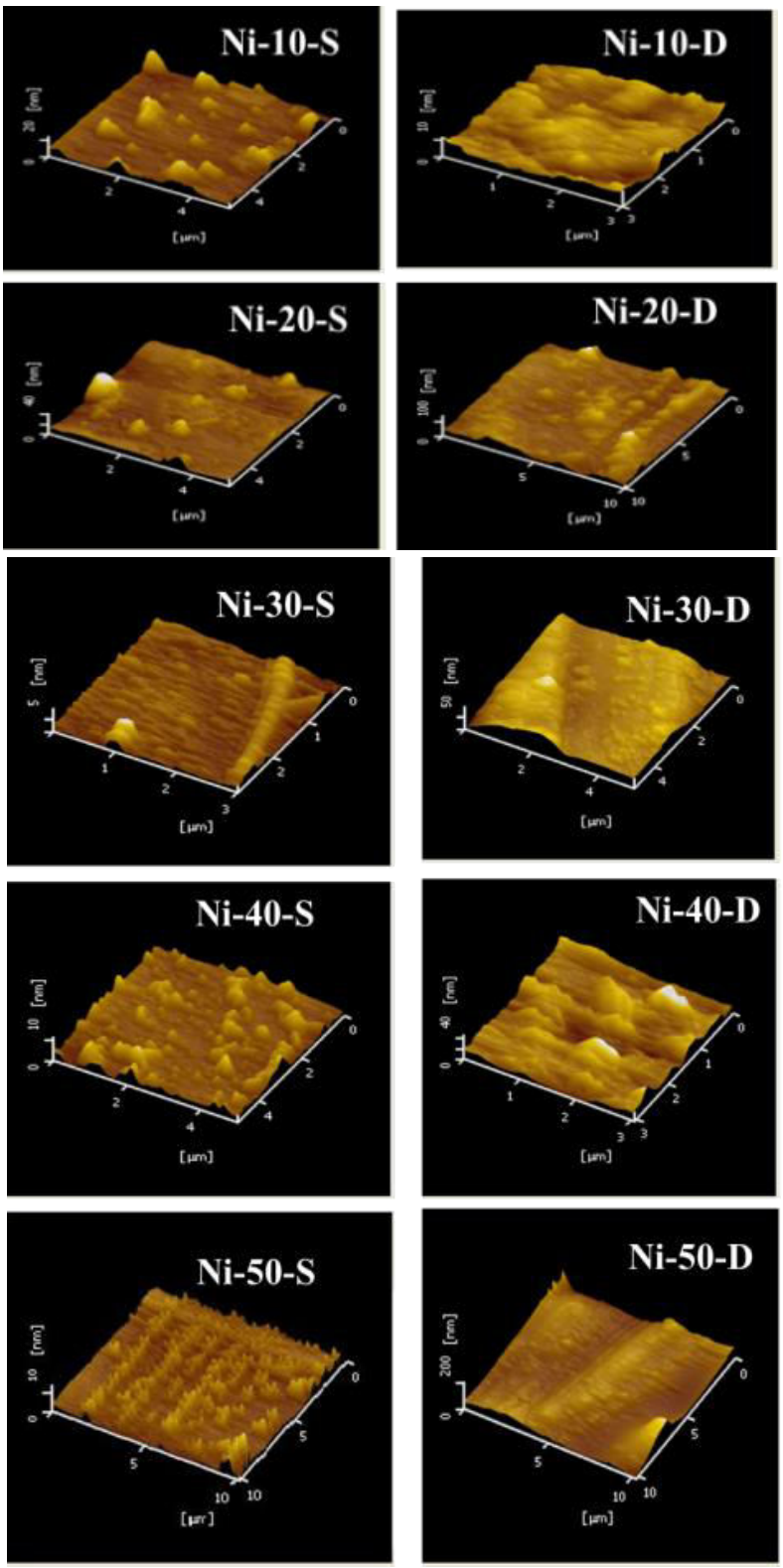

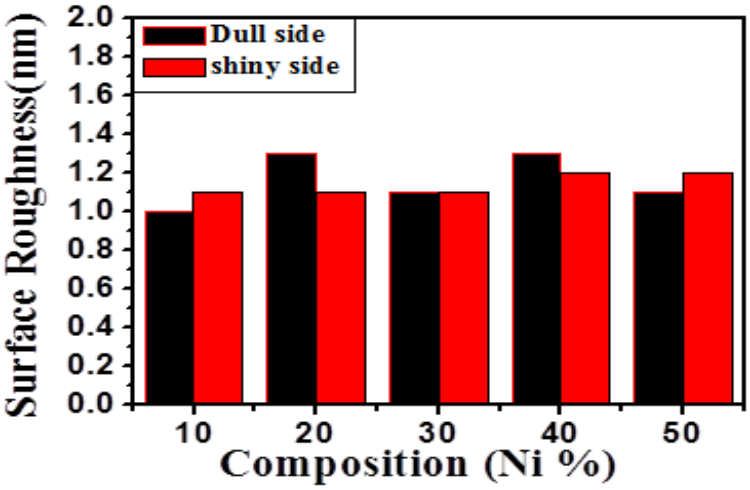


Fig. 3.16: Roughness histogram measured by AFM technique for the $Ti_{20}Zr_{20}Cu_{60-x}Ni_x$ (x= 10,20,30,40 and 50) metallic glass ribbons.

Table 3.11: Average Roughness values (in nm) measured by AFM for virgin $Ti_{20}Zr_{20}Cu_{60-x}Ni_x$ (x= 10,20,30,40 and 50) metallic glass ribbons.

| **Composition** | **Average Roughness( in nm) measured by AFM** | |
|---|---|---|
| | **Shiny side (nm)** | **Dull side (nm)** |
| $Ti_{20}Zr_{20}Cu_{50}Ni_{10}$ | 1.0 | 1.1 |
| $Ti_{20}Zr_{20}Cu_{40}Ni_{20}$ | 1.3 | 1.1 |
| $Ti_{20}Zr_{20}Cu_{30}Ni_{30}$ | 1.1 | 1.1 |
| $Ti_{20}Zr_{20}Cu_{20}Ni_{40}$ | 1.3 | 1.2 |
| $Ti_{20}Zr_{20}Cu_{10}Ni_{50}$ | 1.1 | 1.2 |

AFM images of the surface topography for the pairs of corresponding shiny (s) and dull (D) sides of $Ti_{20}Zr_{20}Cu_{60-x}Ni_x$ (x= 10, 20, 30, 40 and 50) metallic glass ribbons **are** shown in Figs 3.16 (a, b), (c, d), (e, f), (g, h) and (i, j). This is possibly the very first attempt made by us to the best of our knowledge to look at roughness as well as surface topography of both shiny and dull sides of metallic glass ribbons. The histogram of average surface roughness (Ra) values of $Ti_{20}Zr_{20}Cu_{60-x}Ni_x$ (x= 10, 20, 30, 40 and 50) metallic glass ribbons are shown in Fig. 3.16. The corresponding average surface roughness values of both sides and determined by scanning 10 spots on each metallic

glass ribbon are given in Table 3.11. For the compositions $Ti_{20}Zr_{20}Cu_{10}Ni_{50}$ and $Ti_{20}Zr_{20}Cu_{50}Ni_{10}$the dull sides had roughness marginally lower than those of the corresponding shiny sides. For the compositions $Ti_{20}Zr_{20}Cu_{30}Ni_{30}$the dull side had roughness equal to that of the corresponding shiny side. However, for the compositions $Ti_{20}Zr_{20}Cu_{40}Ni_{20}$ and $Ti_{20}Zr_{20}Cu_{20}Ni_{40}$ the shiny sides had roughness marginally lower than those of the corresponding dull sides. Although a one to one correspondence between surface roughness and preferential initiation of surface crystallization in comparison to that in the bulk is yet to be unequivocally established [15]. It is speculated that surface roughness may affect the rate and kinetics of crystallization.

**3.7 Annealing studies of ribbons**

The XRD spectra shown in Fig. 3.17 confirmed that annealing at 753 K for 30 min produced the crystalline phases $Ni_4Ti_3$, $Cu_{51}Zr_{14}$, $Ni_2Ti$ and $NiTi_2$ in the $Ti_{20}Zr_{20}Cu_{50}Ni_{10}$ metallic glass ribbon. The annealing temperature corresponded to the onset of crystallization temperature ($T_x$) of the second exothermic peak on DSC curve (Fig. 3.3).The XRD spectra shown in Fig. 3.18 confirmed that annealing at 756 K for 30 min produced the crystalline phases $NiTi_2$, NiTi, $Ni_4Ti_3$, $CuNi_2Ti$, $Ni_2Ti$ and $Cu_8Zr_3$in the $Ti_{20}Zr_{20}Cu_{50}Ni_{10}$ metallic glass ribbons. The annealing temperature corresponded to the onset of crystallization temperature ($T_x$) of the exothermic peak on DSC curve (Fig. 3.4). The XRD spectra shown in Fig. 3.19 confirmed that annealing at 758 K for 30 min produced the crystalline phases NiTi, $NiTi_2$, $Ni_4Ti_3$, $CuNi_2Ti$, and $Ni_2Ti$, $NiTi_{0.8}Zr_{0.2}$ in the $Ti_{20}Zr_{20}Cu_{30}Ni_{30}$ metallic glass ribbons [16]. The annealing temperature corresponded to the onset of crystallization temperature ($T_x$) of the exothermic peak on DSC curve (Fig. 3.5).

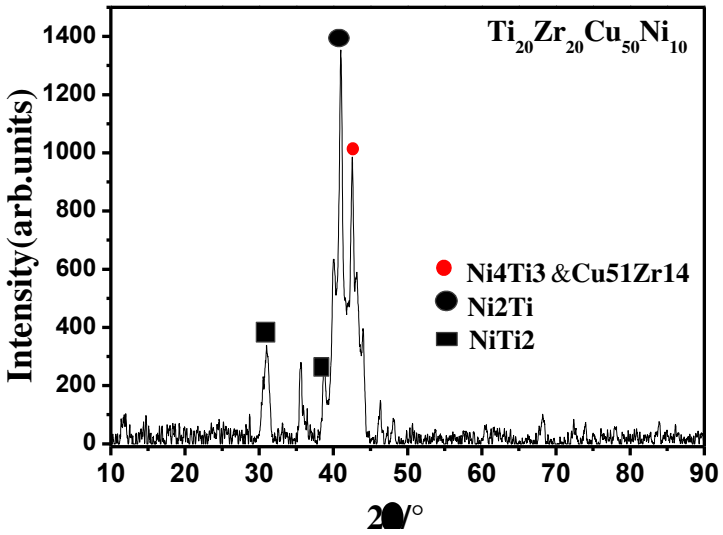


Fig. 3.17 The $Ti_{20}Zr_{20}Cu_{50}Ni_{10}$ metallic glass ribbon annealed at 753 K for 30 min, and the corresponding XRD spectrum.

The XRD spectra shown in Fig. 3.20 confirmed that annealing at 778 K for 30 min produced the crystalline phases NiTi, $NiTi_2$, $Ni_2Ti$, $Cu_8Zr_3$, $Ni_4Ti_3$, $CuNi_2Ti$, $Ni_2Ti$, and $NiTi_{0.8}Zr_{0.2}$ in the $Ti_{20}Zr_{20}Cu_{20}Ni_{40}$ metallic glass ribbons. The annealing temperature corresponded to the onset of crystallization temperature ($T_x$) of the exothermic peak on DSC curve (Fig. 3.6).

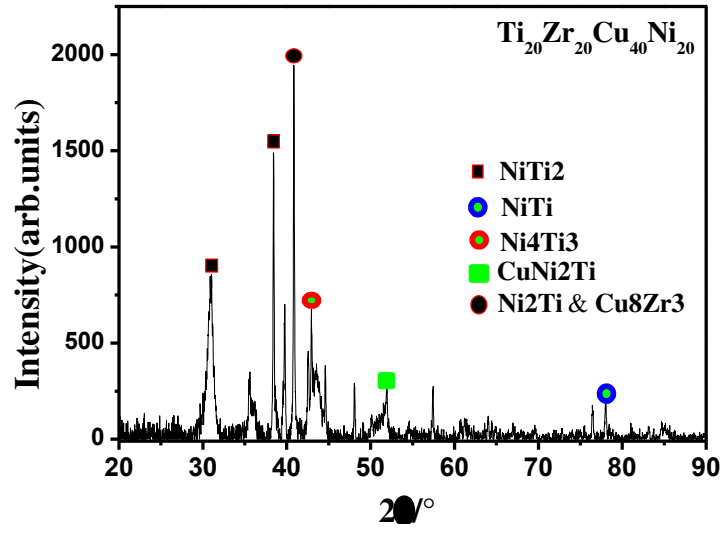


Fig. 3.18 The $Ti_{20}Zr_{20}Cu_{40}Ni_{20}$ metallic glass ribbon annealed at 756 K for 30 min, and the corresponding XRD spectrum.

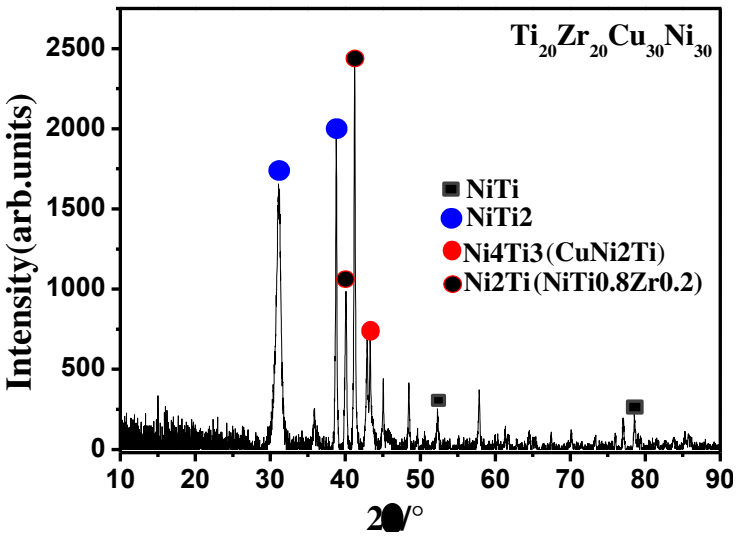


Fig. 3.19 XRD spectra of the $Ti_{20}Zr_{20}Cu_{30}Ni_{30}$ Metallic glass Ribbons annealed at 758 K for 30Min.

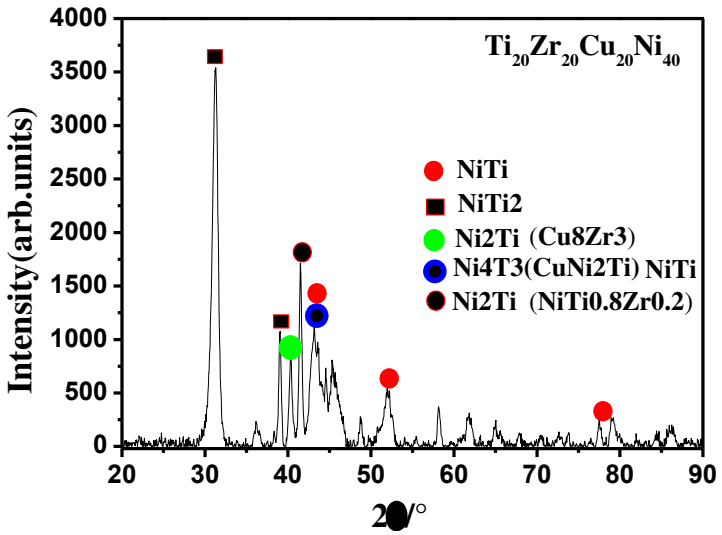


Fig. 3.20 XRD spectra of the $Ti_{20}Zr_{20}Cu_{20}Ni_{40}$ Metallic glass Ribbons annealed at 778 K for 30Min.

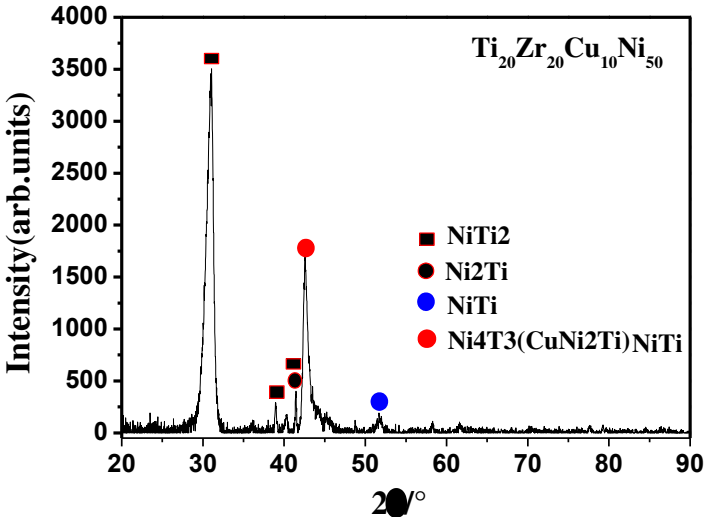


Fig. 3.21 The $Ti_{20}Zr_{20}Cu_{10}Ni_{50}$ metallic glass ribbon annealed at 783 K for 30min, and the corresponding XRD spectrum.

The XRD spectra shown in Fig. 3.21 confirmed that annealing at 783 K for 30 min produced the crystalline phases $NiTi_2$, $Ni_2Ti$, NiTi, $Ni_4Ti_3$, and $CuNi_2Ti$ in the $Ti_{20}Zr_{20}Cu_{10}Ni_{50}$ metallic glass ribbons. The annealing temperature corresponded to the onset of crystallization temperature ($T_x$) of the exothermic peak on DSC curve (Fig. 3.7).

### 3.8 Transmission Electron Microscopy

#### 3.8.1 The annealed ribbon at 753 K for 30 min of $Ti_{20}Zr_{20}Cu_{50}Ni_{10}$ metallic glass

The Figs. 3.22(a-c), represent the bright field (BF), dark field (DF) and corresponding SAED [17], respectively for the$Ti_{20}Zr_{20}Cu_{50}Ni_{10}$ metallic glass ribbon annealed at 753 K for 30 min. Table 3.12 presents the corresponding data on composition analysis of the annealed $Ti_{20}Zr_{20}Cu_{50}Ni_{10}$ metallic glass ribbon. These results e.g., Fig. 3.23 (c) and Table 3.12 corroborated with the corresponding XRD data (Fig. 3.17).The homogeneous distribution of the various nanocrystalline phases in amorphous matrix has been shown in Figs.3.21 (a) and (b). Existence of these nanocrystalline phases were confirmed from both the XRD data (Fig. 3.17) and the compositional analysis data obtained from the TEM studies (Table 3.12).The range of the size of spherical features in the dark field image (Figure 3.22b) was about 10 to 100nm while the average feature

size was about 50 nm (Figure 3.22a). The BF, DF and corresponding SAED pattern of the annealed $Ti_{20}Zr_{20}Cu_{40}Ni_{20}$ metallic glass at 756 K for 30min are shown in Figs 3.23(a), (b) and (c), respectively. Table 3.13 presents the corresponding data on compositional analysis of the same annealed ribbon. These results e.g., Fig. 3.23 (c) and Table 3.13 corroborated with the corresponding XRD data (Fig. 18). The homogeneous distribution of the various nanocrystalline phases in amorphous matrix has also been observed (Figs. 3.23 (a) and (b)). Existence of the nanocrystalline phases were confirmed from both the XRD data (Fig. 3.18) and the compositional analysis data obtained from the TEM studies (Table 3.13). The range of the size of spherical features in the dark field image (Figure 3.23b) was about 10 to 100nm [18, 19].

The same phenomena followed for BF, DF and the corresponding SAED patterns of the annealed metallic glass ribbons viz., $Ti_{20}Zr_{20}Cu_{30}Ni_{30}$ (annealed at 758 K), $Ti_{20}Zr_{20}Cu_{20}Ni_{40}$ (annealed at 778 K) and $Ti_{20}Zr_{20}Cu_{10}Ni_{50}$ (annealed at 783 K) (Figs.3.24 a-c; Figs.3.25 a-c and Figs.3.26 a-c), as in the case for other two glass ribbons mentioned earlier (sections 3.8.1 and 3.8.2).The corresponding data on compositional analysis of the above three glasses are also shown in TEM studies Tables 3.14-3.16. Existence of these nanocrystallie phases were confirmed from both the XRD data (Figs. 3.19-3.21).

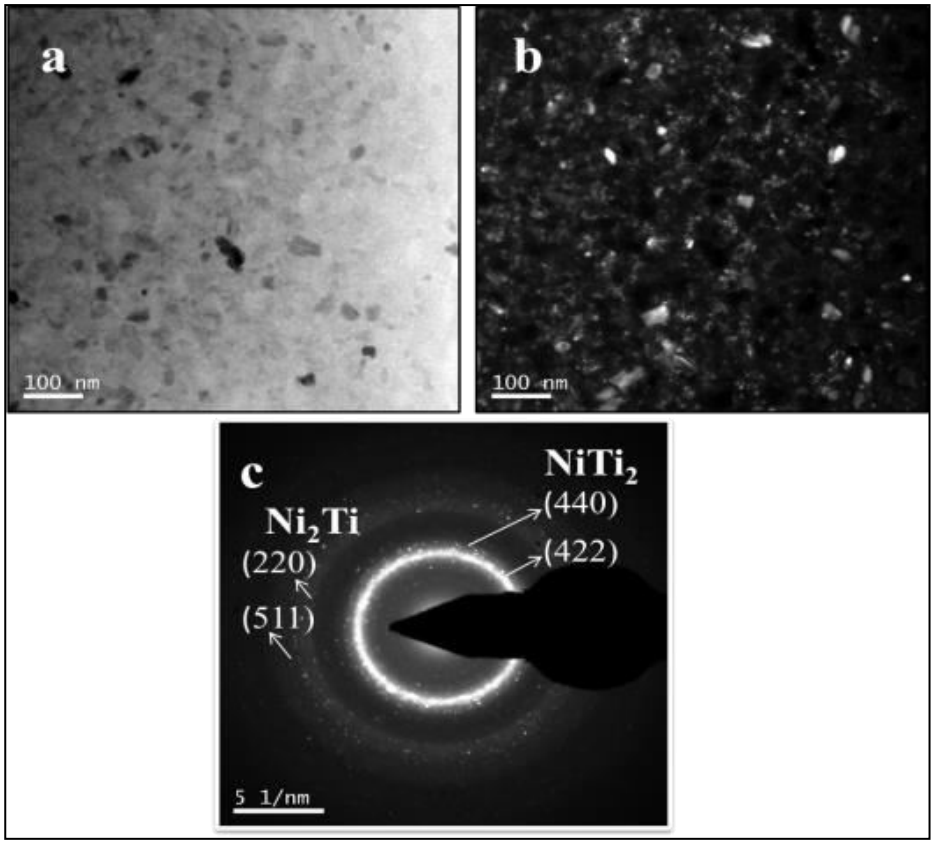


Fig. 3.22 The annealed ribbon of $Ti_{20}Zr_{20}Cu_{50}Ni_{10}$ metallic glass at 753 K for 30min and the corresponding TEM images: (a)-(c): BF image, DF image and selected area of electron diffraction pattern (SAED), respectively.

Table 3.12 The analytical composition of the $Ti_{20}Zr_{20}Cu_{50}Ni_{10}$ metallic glass ribbon (annealed at 753 K for a period of 30min)

| **Elements (at %)** | | | | |
|---|---|---|---|---|
| **Ti** | **Zr** | **Cu** | **Ni** | **Phases** |
| 19.52 | 20.82 | 50.36 | 11.09 | NiTi & NiTi2 |

### 3.8.2 The annealed ribbon at 756 K for 30 min of $Ti_{20}Zr_{20}Cu_{40}Ni_{20}$ metallic glass

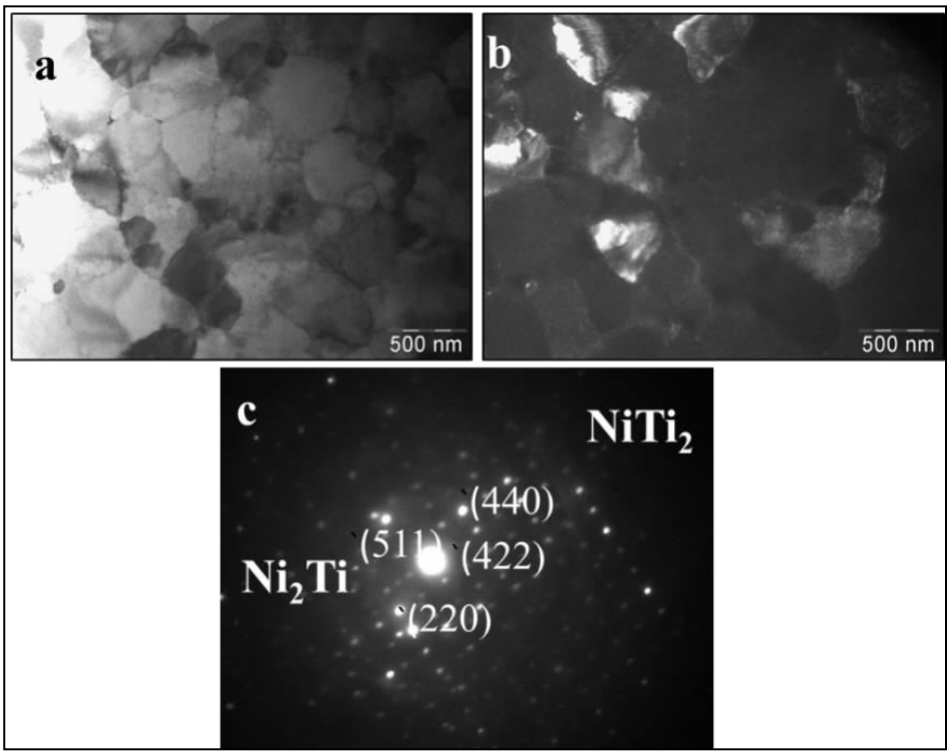


Fig. 3.23The annealed ribbon of $Ti_{20}Zr_{20}Cu_{40}Ni_{20}$ metallic glass at 756 K for 30min and the corresponding TEM images: (a)-(c): BF image, DF image and selected area of electron diffraction pattern (SAED), respectively.

Table 3.13 The analytical composition of the $Ti_{20}Zr_{20}Cu_{40}Ni_{20}$ metallic glass ribbon (annealed at 753 K for a period of 30min)

| **Elements (at. %)** | | | | |
|---|---|---|---|---|
| **Ti** | **Zr** | **Cu** | **Ni** | **Phases** |
| 18.14 | 22.13 | 38.45 | 21.26 | Ni2Ti & NiTi2 |

### 3.8.3 The annealed ribbon at 758 K for 30 min of $Ti_{20}Zr_{20}Cu_{30}Ni_{30}$ metallic glass

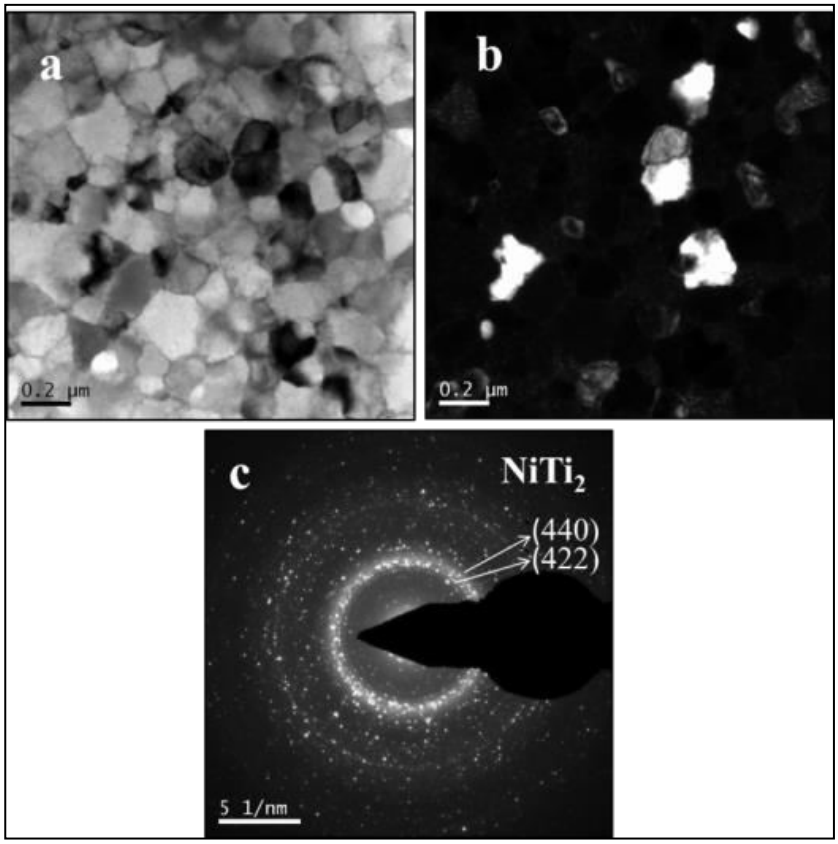


Fig.3.24 The annealed ribbon of $Ti_{20}Zr_{20}Cu_{30}Ni_{30}$ metallic glass at 758 K for 30min and the corresponding TEM images: (a)-(c): BF image, DF image and selected area of electron diffraction pattern (SAED), respectively.

Table 3.14 The analytical composition of the $Ti_{20}Zr_{20}Cu_{30}Ni_{30}$ metallic glass ribbon (annealed at 758K for a period of 30min)

| Elements (at. %) | | | | |
|---|---|---|---|---|
| **Ti** | **Zr** | **Cu** | **Ni** | **Phases** |
| 18.34 | 23.28 | 26.74 | 31.63 | NiTi |

### 3.8.4 The annealed ribbon at 778 K for 30 min of $Ti_{20}Zr_{20}Cu_{20}Ni_{40}$ metallic glass

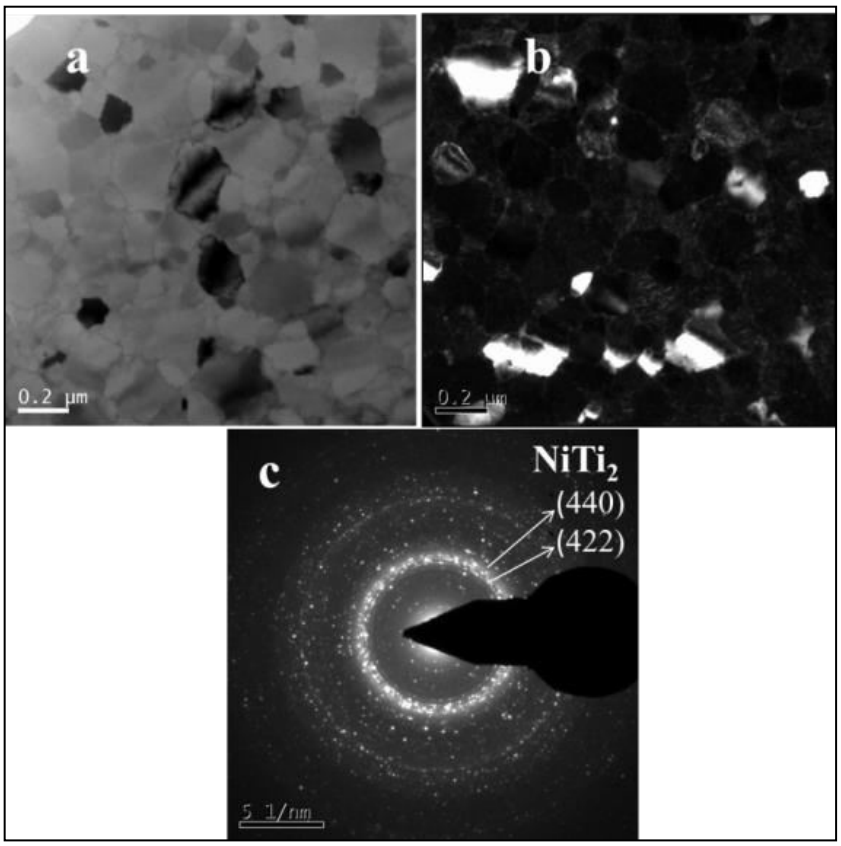


Fig. 3.25 The annealed ribbon of $Ti_{20}Zr_{20}Cu_{20}Ni_{40}$ metallic glass at 778 K for 30min and the corresponding TEM images: (a)-(c): BF image, DF image and selected area of electron diffraction pattern (SAED), respectively.

Table 3.15 The analytical composition of the $Ti_{20}Zr_{20}Cu_{20}Ni_{40}$ metallic glass ribbon (annealed at 778K for a period of 30min)

| **Elements (at. %)** | | | | |
|---|---|---|---|---|
| **Ti** | **Zr** | **Cu** | **Ni** | **Phases** |
| 18.00 | 19.30 | 17.77 | 44.91 | NiTi2 |

### 3.8.5 The annealed ribbon at 783 K for 30 min of $Ti_{20}Zr_{20}Cu_{10}Ni_{50}$ metallic glass

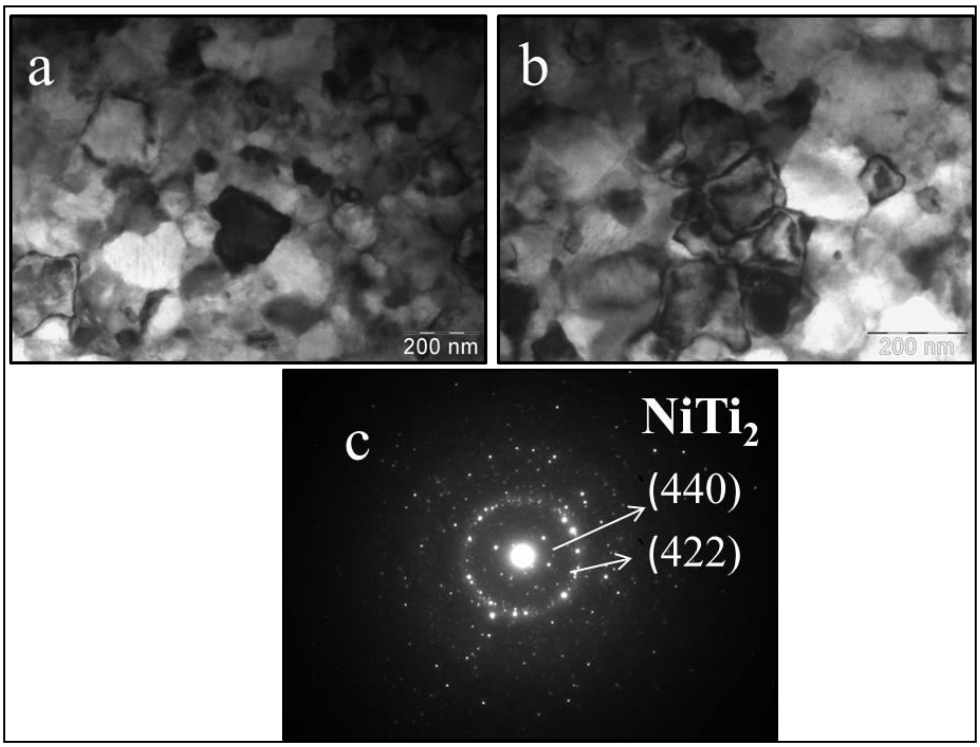


Fig.3.26 The annealed ribbon of $Ti_{20}Zr_{20}Cu_{10}Ni_{50}$ metallic glass at 778 K for 30min and the corresponding TEM images: (a)-(c): BF image, DF image and selected area of electron diffraction pattern (SAED), respectively.

Table 3.16 The analytical composition of the $Ti_{20}Zr_{20}Cu_{10}Ni_{50}$ metallic glass ribbon (annealed at 783K for a period of 30min)

| Elements (at. %) | | | | |
|---|---|---|---|---|
| **Ti** | **Zr** | **Cu** | **Ni** | **Phases** |
| 17.21 | 22.97 | 9.75 | 50.06 | NiTi2 |

### 3.9 Conclusion

A detailed investigations of structural tests was conducted on five different metallic glasses (MGs) have been reported in this chapter. Based on our experimental results, the following conclusion could be summarized**:** XRD results show that all the samples have amorphous in nature. The phase transformation kinetics of the $Ti_{20}Zr_{20}Cu_{60-x}Ni_x$ (x=10, 20, 30, 40 and 50) metallic glasses have been carried out using several

theoretical models and the following conclusions can be made. The metallic glasses under investigation (except $Ti_{20}Zr_{20}Cu_{50}Ni_{10}$ glass) show a single crystallization region, The $Ti_{20}Zr_{20}Cu_{50}Ni_{10}$ glass shows three crystallization peaks.

The activation energy ($E_c$) for the first crystallization was estimated by means of Kissinger, Augis-Bennett and Ozawa models.

FESEM has been used to study surface topography of the $Ti_{20}Zr_{20}Cu_{60-x}Ni_x$ (x= 10, 20, 30, 40 and 50) metallic glasses. Figure 3.11(a) shows the microstructure of the $Ti_{20}Zr_{20}Cu_{50}Ni_{10}$ metallic glass ribbon. The corresponding EDS data along with the typical elemental compositions are shown in Fig. 3.11(b). From AFM images, the actual surface topography has been investigated.

The annealed XRD spectra shown in Fig. 3.17 confirmed that annealing at 753 K for 30 min produced the crystalline phases $Ni_4Ti_3$, $Cu_{51}Zr_{14}$, $Ni_2Ti$ and $NiTi_2$ in the $Ti_{20}Zr_{20}Cu_{50}Ni_{10}$ metallic glass ribbon. The XRD spectra shown in Fig. 3.18 confirmed that annealing at 756 K for 30 min produced the crystalline phases $NiTi_2$, NiTi, $Ni_4Ti_3$, $CuNi_2Ti$, $Ni_2Ti$ and $Cu_8Zr_3$in the $Ti_{20}Zr_{20}Cu_{40}Ni_{20}$ metallic glass ribbon. The XRD spectra shown in Fig. 3.19 confirmed that annealing at 758 K for 30 min produced the crystalline phases NiTi, $NiTi_2$, $Ni_4Ti_3$, $CuNi_2Ti$, and $Ni_2Ti$, $NiTi_{0.8}Zr_{0.2}$ in the $Ti_{20}Zr_{20}Cu_{30}Ni_{30}$ metallic glass ribbon. The XRD spectra shown in Fig. 3.20 confirmed that annealing at 778 K for 30 min produced the crystalline phases NiTi, $NiTi_2$, $Ni_2Ti$, $Cu_8Zr_3$, $Ni_4Ti_3$, $CuNi_2Ti$, $Ni_2Ti$, and $NiTi_{0.8}Zr_{0.2}$ in the $Ti_{20}Zr_{20}Cu_{20}Ni_{40}$ metallic glass ribbons and spectra shown in Fig. 3.21confirmed that annealing at 783 K for 30 min produced the crystalline phases $NiTi_2$, $Ni_2Ti$, NiTi, $Ni_4Ti_3$, and $CuNi_2Ti$ in the $Ti_{20}Zr_{20}Cu_{10}Ni_{50}$ metallic glass ribbon. TEM has been used to study the phase identification and microstructure analysis of the $Ti_{20}Zr_{20}Cu_{60-x}Ni_x$ (x= 10, 20, 30, 40 and 50) metallic glasses. The $Ti_{20}Zr_{20}Cu_{50}Ni_{10}$ metallic glass ribbon annealed at 753 K

for 30min produced the crystalline phases NiTi and $NiTi_2$ and $Ti_{20}Zr_{20}Cu_{40}Ni_{20}$ metallic glass ribbon annealed at 756 K for 30min produced the crystalline phases $Ni_2Ti$ and $NiTi_2$. The $Ti_{20}Zr_{20}Cu_{30}Ni_{30}$, $Ti_{20}Zr_{20}Cu_{20}Ni_{40}$ and $Ti_{20}Zr_{20}Cu_{10}Ni_{50}$ metallic glass ribbons annealed at 758, 778 and 783 K, respectively for a period of 30 min produced the crystalline phases of NiTi, $NiTi_2$ and $NiTi_2$, respectively. The homogeneous distribution of the various nanocrystalline phases in the amorphous matrix and the existence of these nanocrystallie phases were confirmed from the XRD, TEM data and compositional analysis data obtained from the EDS studies.

## References


1. H.E.Kissinger, Anal. Chem. 29, 1702 (1957).
2. J.A.Augis, J.E.Bennett, J.Therm, Anal Color 13, 283(1978).
3. T.Ozawa, Polymer 12, 150(1971).
4. F. Spaepen, A microscopic mechanism for steady state inhomogeneous flow in metallic glasses, Acta Metall. 25 (1977) 407e415.
5. J.J. Kim, Y. Choi, S. Suresh, A.S. Argon, Nano crystallization during nan indentation of a bulk amorphous metal alloy at room temperature, Science 295 (2002) 654-657.
6. W.H. Wang, D.W. He, D.Q. Zhao, Y.S. Yao, M. He, Nanocrystallization of ZrTiCuNiBeC bulk metallic glass under high pressure, Appl. Phys. Lett. 75 (1999) 2770-2772.
7. M. Telford, The case for bulk metallic glass, Mater. Today 7 (2004) 36-43.
8. B. Zhang, D.Q. Zhao, M.X. Pan, W.H. Wang, A.L. Greer, Amorphous metallic plastic, Phys. Rev. Lett. 94 (2005) 205502.
9. R. Martinez, G. Kumar, J. Schroers, Hot rolling of bulk metallic glass in its supercooled liquid region, Scr. Mater. 59 (2008) 187-190.
10. H.M. Chiu, G. Kumar, J. Blawzdziewicz, J. Schroers, Thermoplastic extrusion of bulk metallic glass, Scr. Mater. 61 (2009) 28-31.
11. J. Schroers, T.M. Hodges, G. Kumar, H. Raman, A.J. Barnes, Q. Pham, T.A. Waniuk, Thermoplastic blow molding of metals, Mater. Today 14 (2011) 14-19.
12. Y. Fukuda, Y. Saotome, H. Kimura, A. Inoue, Nanoimprinting of metallic glass for periodic nano-hole structures with dies fabricated by FIB-CVD and RIE, Mater. Trans. 52 (2011) 239-242.
13. G. Kumar, A. Desai, J. Schroers, Bulk metallic glass: the smaller the better, Adv.Mater. 23 (2011) 461-476.
14. J.P. Patterson, D.R.H. Jones, Moulding of a metallic glass, Mater. Res. Bull. 13(1978) 583-585.
15. Y. Kawamura, T. Itoi, T. Nakamura, A. Inoue, Mater. Sci. A 304e306 (2001) 735-739.
16. Y. Saotome, K. Imai, S. Shioda, S. Shimizu, T. Zhang, A. Inoue, Intermetallics 10(2002) 1241-1247.
17. G. Kumar, G. Rector, R.D. Conner, J. Schroers, Embrittlement of Zr-based bulk metallic glasses, Acta Mater. 57 (2009) 3572-3583.

18. Patel AT, Pratap A. Kinetics of crystallization of Zr52Cu18Ni14-Al10Ti6 metallic glass. J Therm Anal Calorim. 2012; 107: 159–65.

19. Johari GP, Schmeltzer JWP. Crystal nucleation and growth in glass forming systems: some new results and open problems. In: Schmeltzer JWP, editor. Glass: selected properties and crystallization. New York: Walter de Gruyter; 2014. p. 521–87.

20. H. E. Kissinger, J. Res. Nat. Bur. Stand. 57(1956) 217–221.

21. J.A. Augis , J.E. Bennett, J. Therm. Anal. 13 (1978) 283-292.

22. T. Ozawa, Bull. Chem. Soc. Jpn. 35 (1965) 1881-1886.

23. A. Hruby´, "Evaluation of Glass-Forming Tendency by Means of DTA," Czech.

# Chapter 4
# Mechanical and Functional properties

## 4.1 Introduction

The metallic amorphous alloys were widely studied in the recent past because they possess excellent characteristics *viz*., soft magnetic properties, greater compressive strength, significant behaviour of anti-corrosion and many others. In many applications, mechanical properties of metallic glasses (MGs) are an important input. Similarly, in many electrical and magnetic applications, it is important to know electrical behaviour of a metallic glass with composition as well as temperature. The variations of the physical, mechanical and electrical properties of $Ti_{20}Zr_{20}Cu_{60-x-}Ni_x$ (x=10, 20, 30, 40 and 50) metallic glasses as a function of composition are presented in this Chapter.

There were first report of high glass forming ability (GFA) of Cu-Ti based alloys namely, $Cu_{47}Ti_{34}Zr_{11}Ni_8$ and $Cu_{47}Ti_{33}Zr_{11}Ni_8Si_{1,}$ which can be cast fully amorphous in the rod forms of 4 and 7 mm in diameter [1, 2]. Afterwards, much effort were made in order to develop novel Cu-Ti based bulk glassy alloys possessing more GFA and improved mechanical properties [3, 4]. However, it has been observed that the metallic glasses have drawbacks which are the lack of ductility shown in tensile experiments and limited plasticity under macroscopic compression [5]. Therefore, in order to overcome the above constraints, the technique of the nanoindentation has become popular to evaluate mechanical properties of these materials [6-8]. The response of nanoindentation on Cu-Ti based metallic glasses has recently been appeared [9].

## 4.2 Density

The experimentally measured density of all the alloys and the corresponding $Ti_{20}Zr_{20}Cu_{60-x}Ni_x$ (x=10, 20, 30, 40 and 50) metallic glasses have been plotted as a function of the percentage of Ni in the composition and are shown in Fig. 4.1. The data from Fig. 4.1 confirmed that the density (ρ) of all the alloys decreased consistently from 7.9 to 7.5 g/cm$^3$ while those of all the metallic glasses decreased consistently from 7.5 to 7.1 g/cm$^3$ as the Ni percentage was increased from 10 to 50% in the corresponding compositions [10]. These data are also included in Table 4.1.

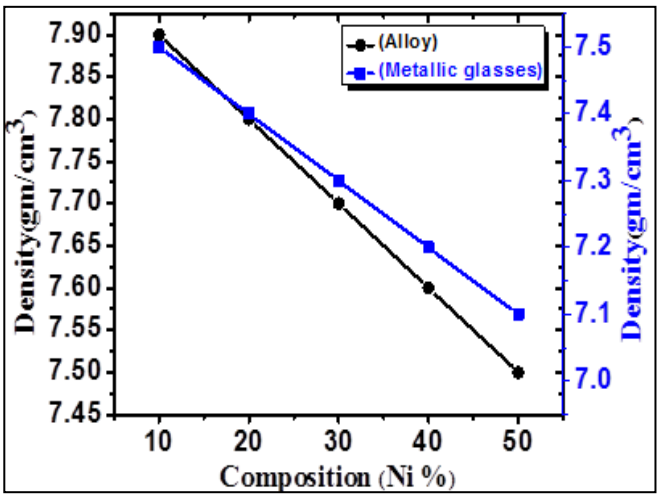


Fig.4 .1 experimentally measured density of all the alloys and the corresponding $Ti_{20}Zr_{20}Cu_{60-x}Ni_x$ (x=10, 20, 30, 40 and 50) metallic glasses as a function of the percentage of Ni in the composition.

Table 4.1 Density data of metallic alloys and as-spun ribbons

| Composition | Density measurement of alloys and as-spun ribbons | |
|---|---|---|
| | Alloy (g/cm$^3$) | As-spun ribbon (g/cm$^3$) |
| $Ti_{20}$ $Zr_{20}$ $Cu_{50}$ $Ni_{10}$ | 7.94 | 7.57 |
| $Ti_{20}$ $Zr_{20}$ $Cu_{40}$ $Ni_{20}$ | 7.85 | 7.42 |
| $Ti_{20}$ $Zr_{20}$ $Cu_{30}$ $Ni_{30}$ | 7.75 | 7.34 |
| $Ti_{20}$ $Zr_{20}$ $Cu_{20}$ $Ni_{40}$ | 7.63 | 7.22 |
| $Ti_{20}$ $Zr_{20}$ $Cu_{10}$ $Ni_{50}$ | 7.51 | 7.14 |

The lower density of metallic glasses in ribbon is expected due to voids, defects etc. which may depend on the melt spinning conditions.

### 4.3 Mechanical Properties: nanoindentation studies on the $Ti_{20}Zr_{20}Cu_{60-x}Ni_x$ (x=10, 20, 30, 40 and 50) metallic glasses.

The significant physical quantities obtained from the load versus depth of penetration plot are: the peak load, $P_{max}$, maximum depth of penetration, $h_{max}$, final depth of penetration, $h_f$, and the contact stiffness, S. from the Oliver and Pharr (O-P) model [6] the nanohardness (H) of a material is given by the following Equation (1):

$$H = \frac{P_{\max}}{A_{cr}} \quad (1)$$

where, $P_{max}$ is the maximum applied load in the nanoindentation experiment and $A_{cr}$ is the real contact area between the nanoindenter and the material.

According to Oliver and Pharr [6], the polynomial form of $A_{cr}$ can be expressed as Equation (2):

$$A_{cr} = 24.56h_c^{\,2} + C_1 h_c + C_2 h_c^{\,1/2} + C_3 h_c^{\,1/4} + ..... + C_8 h_c^{\,1/128} \quad (2)$$

where, $C_1$ to $C_8$ are constants to be determined by standard calibration method and $h_c$ is the penetration depth determined from the following Equation (3):

$$h_c = h_{\max} - \kappa \frac{P_{\max}}{S} \quad (3)$$

where, $\kappa \approx 0.75$ for a Berkovich indenter [6] .

Again, the contact stiffness (S) which is the slope (BE) of the first ~1/3$^{rd}$ linear part recorded during the unloading cycle of the P-h plot (Fig. 1) can be expressed by the following Equation (4) as [6]:

$$S = \frac{dP}{dh}\Big|h = h_{\max} = \alpha C_A E_r \sqrt{A_{cr}} \quad (4)$$

where, $\alpha = 1.034$ and $C_A = 2/\sqrt{\pi}$ for a Berkovich indenter [28] and $E_r$ is the reduced Young's modulus. Following the O-P model [6], $E_r$ can be expressed by the following Equation (5) as:

$$\frac{1}{E_r} = \frac{1-\nu_i^2}{E_i} + \frac{1-\nu_s^2}{E_s} \tag{5}$$

where, $E_i$ and $\nu_i$ are the Young's modulus and Poisson's ratio, respectively and subscripts i and s, denotes the indenter and the sample, respectively. For the Berkovich diamond indenter used in the present work, the values of $E_i$ and $\nu_i$ were taken as 1140 GPa and 0.07 respectively, following [6].

However, according to Oliver and Pharr [6], the unloading curve simply obeys the power law relationship given by the following Equation (6) as:

$$P = \alpha(h - h_f)^m \tag{6}$$

where, α and m are empirical constants which can be determined by fitting the experimentally measured data from the load versus depth of penetration data plot to Equation (6). Thus, the contact stiffness was determined using the following Equation (7) as [6]:

$$S = \frac{dP}{dh}\Big|h = h_{\max} = \alpha m(h - h_f)^{m-1} \tag{7}$$

Therefore, substituting the values of S, α, $C_A$ and $A_{cr}$ in Equation (4), the value of the reduced modulus $E_r$was calculated. The Young's modulus value of the sample, $E_s$, was then easily obtained from Equation (5), using the known values of $E_r$ and $E_i$.

The typical representative P-h plots measured at a load of 5,000 mN for ~~the~~ metallic glasses (a) $Ti_{20}Zr_{20}Cu_{50}Ni_{10,}$ (b) $Ti_{20}Zr_{20}Cu_{40}Ni_{20,}$ (c) $Ti_{20}Zr_{20}Cu_{30}Ni_{30,}$ (d) $Ti_{20}Zr_{20}Cu_{20}Ni_{40}$ and (e) $Ti_{20}Zr_{20}Cu_{10}Ni_{50}$ are shown in Figs 4.2 (a), (b), (c), (d) and (e), respectively. Based on these data and using the mathematical formalism of the Oliver and Pharr model [11], as described earlier in chapter 2, the nanohardness (H) and the reduced Young's modulus (E) were estimated. All these data are depicted in Table 4.2.

The data presented in Table 4.2 show that both reduced Young's modulus (E) and nanohardness (H) increased approximately linearly as the Ni percentage was increased from 10 to 50% in the corresponding compositions. The reason for this is yet to be well understood and hence further work will need to be done in future to understand the genesis of this behaviour.

Table 4.2 Calculated values of hardness and Young's modulus of $Ti_{20}Zr_{20}Cu_{60-x}Ni_x$ (x=10, 20, 30, 40 and 50) metallic glasses measured at a load of 5000 μN

| **Composition** | **Calculated values of hardness and Young's modulus as-spun ribbons** | |
|---|---|---|
| | **E (GPa)** | **H (GPa)** |
| $Ti_{20}$ $Zr_{20}$ $Cu_{50}$ $Ni_{10}$ | 107±6.55 | 7.0±0.18 |
| $Ti_{20}$ $Zr_{20}$ $Cu_{40}$ $Ni_{20}$ | 112±6.88 | 6.9±0.12 |
| $Ti_{20}$ $Zr_{20}$ $Cu_{30}$ $Ni_{30}$ | 121±6.12 | 7.2±0.21 |
| $Ti_{20}$ $Zr_{20}$ $Cu_{20}$ $Ni_{40}$ | 122±7.52 | 7.3±0.23 |
| $Ti_{20}$ $Zr_{20}$ $Cu_{10}$ $Ni_{50}$ | 124±7.88 | 7.4±0.24 |

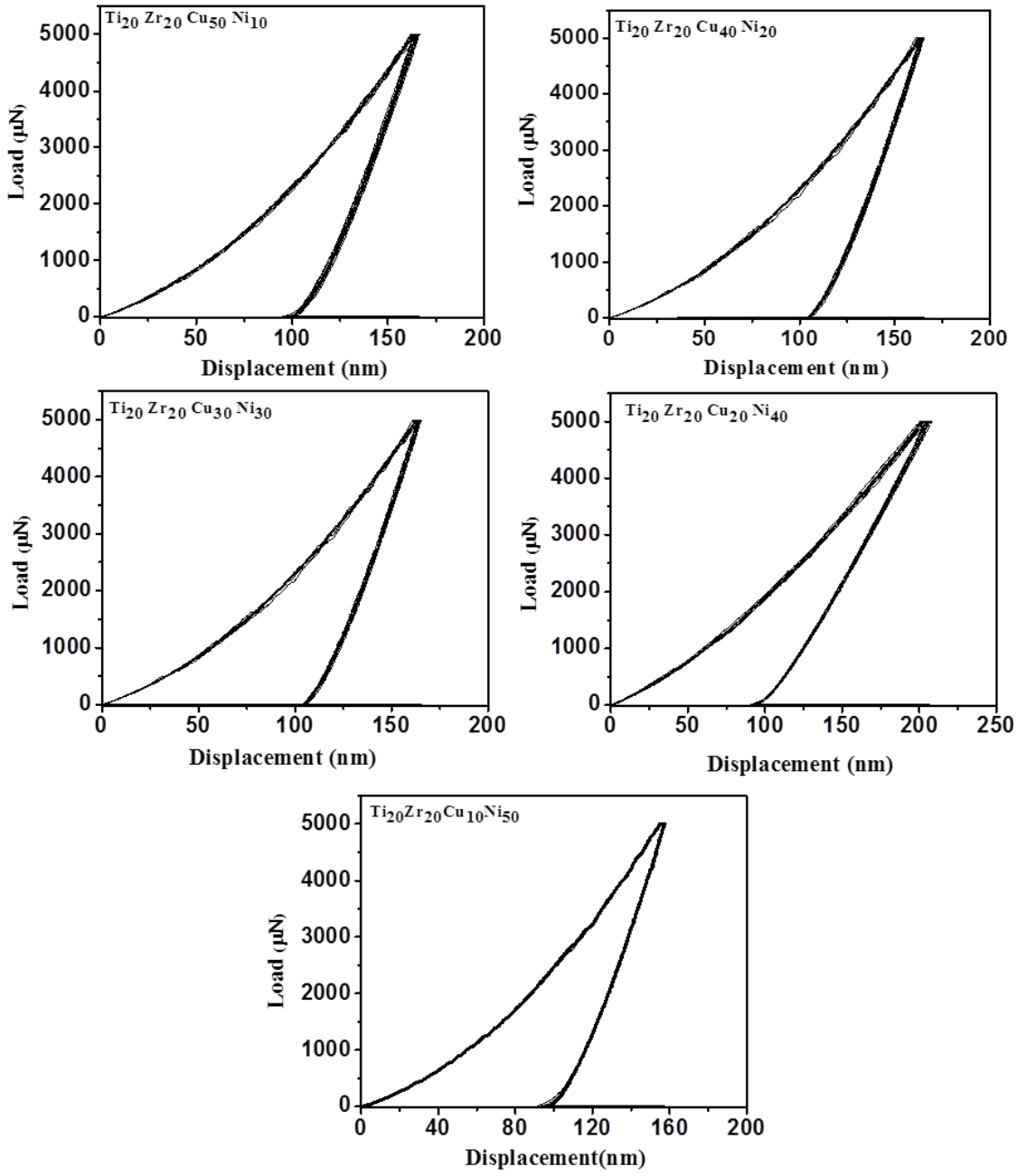


Fig. 4.2 The typical representative P-h plots measured at a load of 5000 μN for the metallic glasses (a) $Ti_{20}Zr_{20}Cu_{50}Ni_{10,}$ (b) $Ti_{20}Zr_{20}Cu_{40}Ni_{20,}$ (c) $Ti_{20}Zr_{20}Cu_{30}Ni_{30,}$ (d) $Ti_{20}Zr_{20}Cu_{20}Ni_{40}$ and (e) $Ti_{20}Zr_{20}Cu_{10}Ni_{50}$.

### 4.4 Electrical Resistivity: Evaluation of temperature dependence resistivity of the $Ti_{20}Zr_{20}Cu_{60-x}Ni_x$ (x=10, 20, 30, 40 and 50) metallic glasses

The magnitudes of ($\rho_{RT}$) at room temperature (i.e., 300K) were measured to be 46, 28, 62, 63 and 32 Ω-cm for $Ti_{20}Zr_{20}Cu_{50}Ni_{10}$, $Ti_{20}Zr_{20}Cu_{40}Ni_{20}$, $Ti_{20}Zr_{20}Cu_{30}Ni_{30}$, $Ti_{20}Zr_{20}Cu_{20}Ni_{40}$ and $Ti_{20}Zr_{20}Cu_{10}Ni_{50}$ metallic glass ribbons, respectively. The normalized resistivity [($\rho_T$)/($\rho_{RT}$)], where ($\rho_T$) is resistivity at a given temperature T(K) and ($\rho_{RT}$) is the resistivity at room temperature for $Ti_{20}Zr_{20}Cu_{50}Ni_{10}$, $Ti_{20}Zr_{20}Cu_{40}Ni_{20}$, $Ti_{20}Zr_{20}Cu_{30}Ni_{30}$, $Ti_{20}Zr_{20}Cu_{20}Ni_{40}$ and $Ti_{20}Zr_{20}Cu_{10}Ni_{50}$ metallic glass ribbons, which are plotted as a function of temperature (from 0 to 1000 K) and shown in Figs 4.3 (a), (b), (c), (d) and (e), respectively. In all the data plotted in Fig 4.3 generally there was a temperature ($T_s$) at which the sudden severe drop in resistivity ratio started and a temperature ($T_m$) at which it reached a minimum value which was taken as the temperature of complete crystallization for the sample. This sharp drop in [($\rho_T$)/($\rho_{RT}$)] was due to the crystallization of each metallic glass. As seen in the figure (a) which is for x = 10 sample, it has more than one crystallization as observed in DSC also. For x =2 sample, it shows first crystallization and a very small crystallization later which was not detected in DSC, This may be due to different heating rates in the electrical resistance measurements which was much slower than the ones used in DSC measurements. For other samples it shows only one crystallization as observed in DSC.

For $Ti_{20}Zr_{20}Cu_{50}Ni_{10}$, $Ti_{20}Zr_{20}Cu_{40}Ni_{20}$, $Ti_{20}Zr_{20}Cu_{30}Ni_{30}$, $Ti_{20}Zr_{20}Cu_{20}Ni_{40}$ and $Ti_{20}Zr_{20}Cu_{10}Ni_{50}$ metallic glass ribbons these pair ($T_s$ and $T_m$) of temperatures were measured to be respectively (749 and 788 K, Figure 4.3 (a)), (779 and 798 K, Fig 4.3 (b)), (778 and 800 K, Fig 4.3 (c)), (794 and 820 K, Fig 4.3(d)) and (803 and 822 K, Fig 4.3 (e)). These data are given in Table 4.3.

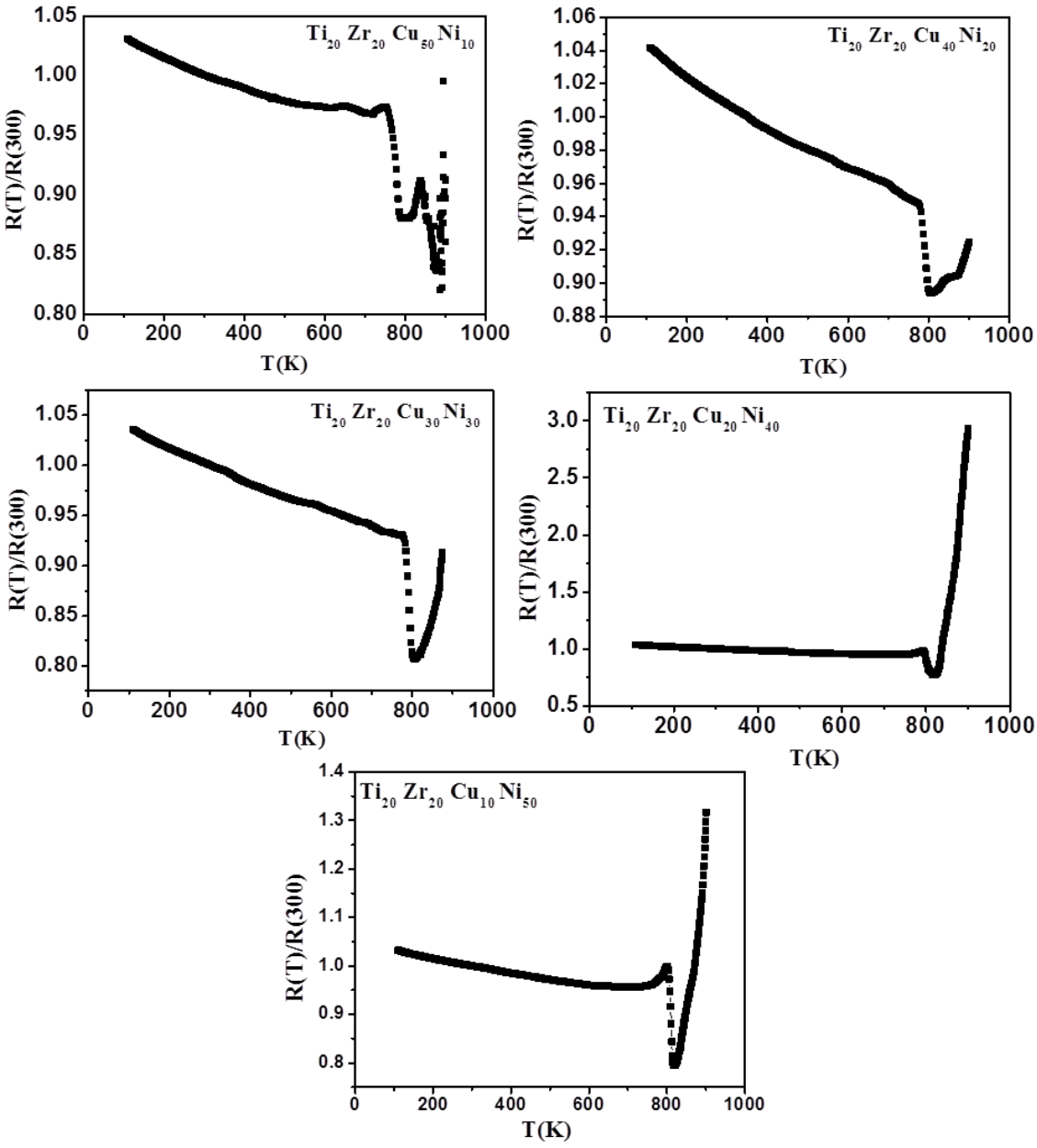


Fig .4.3 Temperature (e.g., from 0 to 1000 K) dependence of normalized resistivity for metallic glass ribbons : (a) $Ti_{20}Zr_{20}Cu_{50}Ni_{10}$, (b)$Ti_{20}Zr_{20}Cu_{40}Ni_{20}$, (c) $Ti_{20}Zr_{20}Cu_{30}Ni_{30}$, (d) $Ti_{20}Zr_{20}Cu_{20}Ni_{40}$ and (e) $Ti_{20}Zr_{20}Cu_{10}Ni_{50}$.

Table 4.3 Room Temperature Resistivity of $Ti_{20}Zr_{20}Cu_{60-x}Ni_x$ (x=10, 20, 30, 40 and 50) metallic glasses and corresponding temperatures of onset and completion of crystallization processes (Temperature given in bracket is derived from DSC measurements as-spun ribbons.)

| **Composition** | **Room Temperature Resistivity (Temperature given in bracket is derived from DSC measurements as-spun ribbons.)** | | |
|---|---|---|---|
| | **$T_x$(K)** | **$T_P$(K)** | **RT-ρ (μΩ-cm)** |
| $Ti_{20}Zr_{20}Cu_{50}Ni_{10}$ | 749 (753) | 788 (771) | 61 |
| $Ti_{20}Zr_{20}Cu_{40}Ni_{20}$ | 779 (756) | 798 (764) | 60 |
| $Ti_{20}Zr_{20}Cu_{30}Ni_{30}$ | 778 (758) | 800 (763) | 62 |
| $Ti_{20}Zr_{20}Cu_{20}Ni_{40}$ | 794 (778) | 820 (785) | 63 |
| $Ti_{20}Zr_{20}Cu_{10}Ni_{50}$ | 803 (783) | 822 (788) | 64 |

Just for the purpose of comparison two other temperatures are added inside first brackets in corresponding cases. These are $T_x$, the crystallization initiation temperature as mentioned earlier and $T_P$ the peak temperature as discussed earlier in Chapter 3. Based on the experimental data presented in Chapter 3, for $Ti_{20}Zr_{20}Cu_{50}Ni_{10}$, $Ti_{20}Zr_{20}Cu_{40}Ni_{20}$, $Ti_{20}Zr_{20}Cu_{30}Ni_{30}$, $Ti_{20}Zr_{20}Cu_{20}Ni_{40}$ and $Ti_{20}Zr_{20}Cu_{10}Ni_{50}$ metallic glass ribbons these pair ($T_x$ and $T_p$) of temperatures were measured to be respectively (753 and 771 K, Table 4.3), (756 and 764 K, Table 4.3), (758 and 763K, Table 4.3), (778 and 785, Table 4.3) and (783 and 788K, Table 4.3). Thus, in other words, these temperatures compared fairly well with the experimentally measured pair ($T_s$ and $T_m$) of temperatures for the metallic glass ribbon samples in correspondence. The difference may be due to the slow heating rate used in the resistance measurements, as mentioned earlier.

Finally, some minor differences in ($T_s$ and $T_m$) and ($T_x$ and $T_p$) could be attributed to the corresponding differences in temperature measurements due to the usage of different thermocouples in DSC and resistivity measurement experiments, and the variations in rate of increase of temperature in the respective cases. Also it needs to be noted that ($T_s$ and $T_m$) and ($T_x$ and $T_p$) are kind of similar but not exactly the same as each other. Moreover, the heat flow measured in DSC experiments is entirely different from resistivity ratio measured in temperature dependence of resistivity experiments. It was interesting to note that $Ti_{20}Zr_{20}Cu_{10}Ni_{50}$ metallic glass also showed linear behaviour over a large temperature interval but the slope of the normalized resistivity versus temperature curve much less. However, it showed a slightly different behaviour at about 523 K where $[(\rho_T)/(\rho_{RT})]$ had started to decrease slowly without exhibiting a sharp drop until the temperature had risen to about 653 K where a sharp decrease in $[(\rho_T)/(\rho_{RT})]$ was observed. Thus, $[(\rho_T)/(\rho_{RT})]$ reached the minimum value at about 703 K prior to a sharp increase at 753 K. However, beyond 753K $[(\rho_T)/(\rho_{RT})]$ started to decrease again. Thus, the particular normalized resistivity measurements indicated the existence of three regions where $[(\rho_T)/(\rho_{RT})]$ started to decrease. In other words these data mean that there were possibly three crystallization steps. The first one appeared to be sluggish. It was followed by the second one which showed fast crystallization. This second crystallization step was followed by the third one which had also exhibited fast crystallization. It may be recalled that the corresponding DSC plot had shown (Fig 4.3) only two crystallization steps. The first crystallization step was sluggish while the other one was a fast one. It is conjectured that possibly the first crystallization step was so sluggish that it could not be observed in the DSC experiments.

For $Ti_{20}Zr_{20}Cu_{40}Ni_{20}$, $Ti_{20}Zr_{20}Cu_{30}Ni_{30}$, $Ti_{20}Zr_{20}Cu_{20}Ni_{40}$ and $Ti_{20}Zr_{20}Cu_{10}Ni_{50}$ metallic glass ribbons single sharp drop followed by the sharp rise in $[(\rho_T)/(\rho_{RT})]$ confirmed that these were really single step crystallization processes as observed earlier in the respective DSC measurements (Figures 3.3,3.4,3.5,3.6 and 3.7, Chapter 3). The data presented in Fig. 4.3 confirmed that on an average the normalized resistivity of all samples had a linear dependency on temperature in the range from 73 K to 773 K. Ziman [11, 12, and 13] has worked on temperature dependence of resistivity of metallic glasses using the liquid metal theory. In both liquid metal and metallic glass only short range order exist. His work has shown that $\rho(T) \propto T$ for $T > \theta_D$, and $\rho(T) \propto T^2$ for $T << \theta_D$ where $\theta_D$ is the Debye temperature which for most metallic glasses it is ~ 200 K (i.e., 73 K). Thus, the observed temperature dependence of resistivity agrees with the Ziman's theoretical predictions [11-13] and it also follows the general trend reported in literature [14-16] for most metallic glasses.

**4.5 Conclusions**

The typical representative plots of P-h obtained at a load of 5000μN for the (a) $Ti_{20}Zr_{20}Cu_{50}Ni_{10}$, (b) $Ti_{20}Zr_{20}Cu_{40}Ni_{20}$, (c) $Ti_{20}Zr_{20}Cu_{30}Ni_{30}$, (d) $Ti_{20}Zr_{20}Cu_{20}Ni_{40}$ and (e) $Ti_{20}Zr_{20}Cu_{10}Ni_{50}$ metallic glasses with a view to understand the Hardness and Young's modulus properties of these metallic glasses. The present work is the very first experimental observation to the best of our knowledge, where density, nanoindentation at a constant peak load of 5000 μN, and the intrinsic contact resistance have been reported. The magnitudes of $\rho_{RT}$ (at 300 K) were measured and found to be 61, 60, 62, 63 and 64 Ω-cm for $Ti_{20}Zr_{20}Cu_{50}Ni_{10}$, $Ti_{20}Zr_{20}Cu_{40}Ni_{20}$, $Ti_{20}Zr_{20}Cu_{30}Ni_{30}$, $Ti_{20}Zr_{20}Cu_{20}Ni_{40}$ and $Ti_{20}Zr_{20}Cu_{10}Ni_{50}$ metallic glass ribbons, respectively.

## Reference


1. X.H. Lin,W.L. Johnson, Formation of Ti–Zr–Cu–Ni bulkmetallic glasses, J. Appl. Phys. 78 (1995) 6514–6519.

2. H. Choi-Yim, R. Busch,W.L. Johnson, The effect of silicon on the glass forming ability of the Cu47Ti34Zr11Ni8 bulk metallic glass forming alloy during processing of composites, J. Appl. Phys. 83 (1998) 7993–7997.

3. Y.J. Yang, F.W. Kang, D.W. Xing, J.F. Sun, Q.K. Shen, J. Shen, Formation andmechanical properties of bulk Cu–Ti–Zr–Ni metallic glasses with high glass forming ability, Trans. Nonferrous Met. Soc. China 17 (2007) 16–20.

4. M. Calin, J. Eckert, L. Schultz, Improved mechanical behavior of Cu–Ti-based bulkmetallic glass by in situ formation of nanoscale precipitates, Scr. Mater. 48 (2003) 653–658.

5. C.A. Schuh, T.G. Nieh, A survey of instrumented indentation studies on metallic glasses, J. Mater. Res. 19 (2004) 46–57.

6. Y. Huang, Y.L. Chiu, J. Shen, J.J.J. Chen, J. Sun, Nanoindentation study of Ti-based metallic glasses, J. Alloys Compd. 479 (2009) 121–128.

7. N.K. Mukhopadhyay, A. Belger, P. Paufler, D.H. Kim, Nanoindentation studies on Cu–Ti–Zr–Ni–Si–Sn bulk metallic glasses, Mater. Sci. Eng. A 449–451 (2007) 954–957.
8. N.K. Mukhopadhyay, P. Paufler, Micro- and nanoindentation techniques for Mechanical characterisation of materials, Int. Mater. Rev. 51 (2006) 209-245.

9. B.B. Medeiros et al. / Journal of Non-Crystalline Solids 425 (2015) 103–109

10 X. L. Bian, G. Wang, K. C. Chan, J. L. Ren, Y. L. Gao, Appl. Phys. Lett. 103, 101907 (2013).

11 Oliver W. C. and Pharr G. M., J. Mater. Res. 7 (1992) 1564.

12 Dugdale J. S., Contemp. Phys. 28 (1987) 547.

13 Howson M.A. and Gallagher B.L., Phys.Repts. 170 (1983) 265.

14 Ziman, J. M., Phil. Mag. 6 (1961) 1013.

15 Mooij J. H., phys. stat.solidi (a) 17 (1973) 521.

16 L. E. Levine Appl. Phys. Lett. 96, 026101 -2010.

## Chapter 5
## Vacuum-brazing of Ti-alloy using melt-spun Ti-Zr-Cu-Ni ribbons

### 5.1 Introduction

This chapter presents the microstructural analysis for brazed samples of $Ti_{20}Zr_{20}Cu_{60-x}Ni_x$ (x=10, 20, 30, 40 and 50) metallic glasses with CP-Ti alloy.

### 5. 2 The melting behaviour of fillers

The filler foils were examined for their melting behaviours by differential thermal (DTA) analyser on a heating rate of 10°C/ min from 900 to 1200°C. Air flow at a constant of 20 ml/min was allowed during these experiments. In Table 5.1, the brazing filler melting ranges are presented.

Table 5.1Themelting behaviours of the filler foil

| Alloys of brazing filler | Melting temperature (Solidus/Liquidus. °C ) |
|---|---|
| $Ti_{20}Zr_{20}Cu_{50}Ni_{10}$ | 910/1000 |
| $Ti_{20}Zr_{20}Cu_{40}Ni_{20}$ | 950/1000 |
| $Ti_{20}Zr_{20}Cu_{30}Ni_{30}$ | 960/1000 |
| $Ti_{20}Zr_{20}Cu_{20}Ni_{40}$ | 980/1010 |
| $Ti_{20}Zr_{20}Cu_{10}Ni_{50}$ | 990/1100 |

### 5.3 Differential Thermal Analysis of $Ti_{20}Zr_{20}Cu_{60-x}Ni_x$(x=10, 20, 30, 40 and 50) metallic glasses

The melting points for $Ti_{20}Zr_{20}Cu_{60-x}Ni_x$ (x=10, 20, 30, 40 and 50) metallic glasses were taken into account, which are shown in Figs 5.1(a-e). There were three peaks found for first onset ($T_{m1}$), second onset ($T_{m1}$) and third onset ($T_{m1}$) melting points at 986, 1089, 1117°C, respectively and similarly three peaks found for first end set ($T_{m2}$), second end set ($T_{m2}$) and third end set ($T_{m2}$) melting points at 999, 1097, 1127°C, respectively. However, only single peak has been observed in other four metallic glasses (Figs 5.1 b-e), the onset and end set were also shown. The DSC data (Chapter

No-3, Section No.3.3.1, Fig. No.2) mentioned earlier also showed that the first $Ti_{20}Zr_{20}Cu_{50}Ni_{10}$ metallic glassy stem had three steps involved in the crystallization, whereas the reaming four metallic glasses had single step during crystallization process. The melting point of $Ti_{66}Ni$ (wt. %) eutectic alloy was obtained from the Ti-Ni binary phase diagram and found to be 1118$^{o}$C [1, 2]. It can be assumed reasonably that the melting point of $TiH_2$-Ni-B brazing powder was mainly accompanied by the composition of the Ti-Ni alloy. During the heating process, the appearance of the second peak is due to the chemical reaction of $Ti + B \rightarrow TiB$. The general observation is that the brazing point temperature is somewhat higher than that of the filler metal and as a result, the brazing temperature selected, accordingly. The brazing temperatures were chosen to be 990, 967, 995, 1004 and 1006$^{o}$C during brazing experiments for metallic glasses are shown in Figs. (a), (b), (c), (d) and (e), respectively.

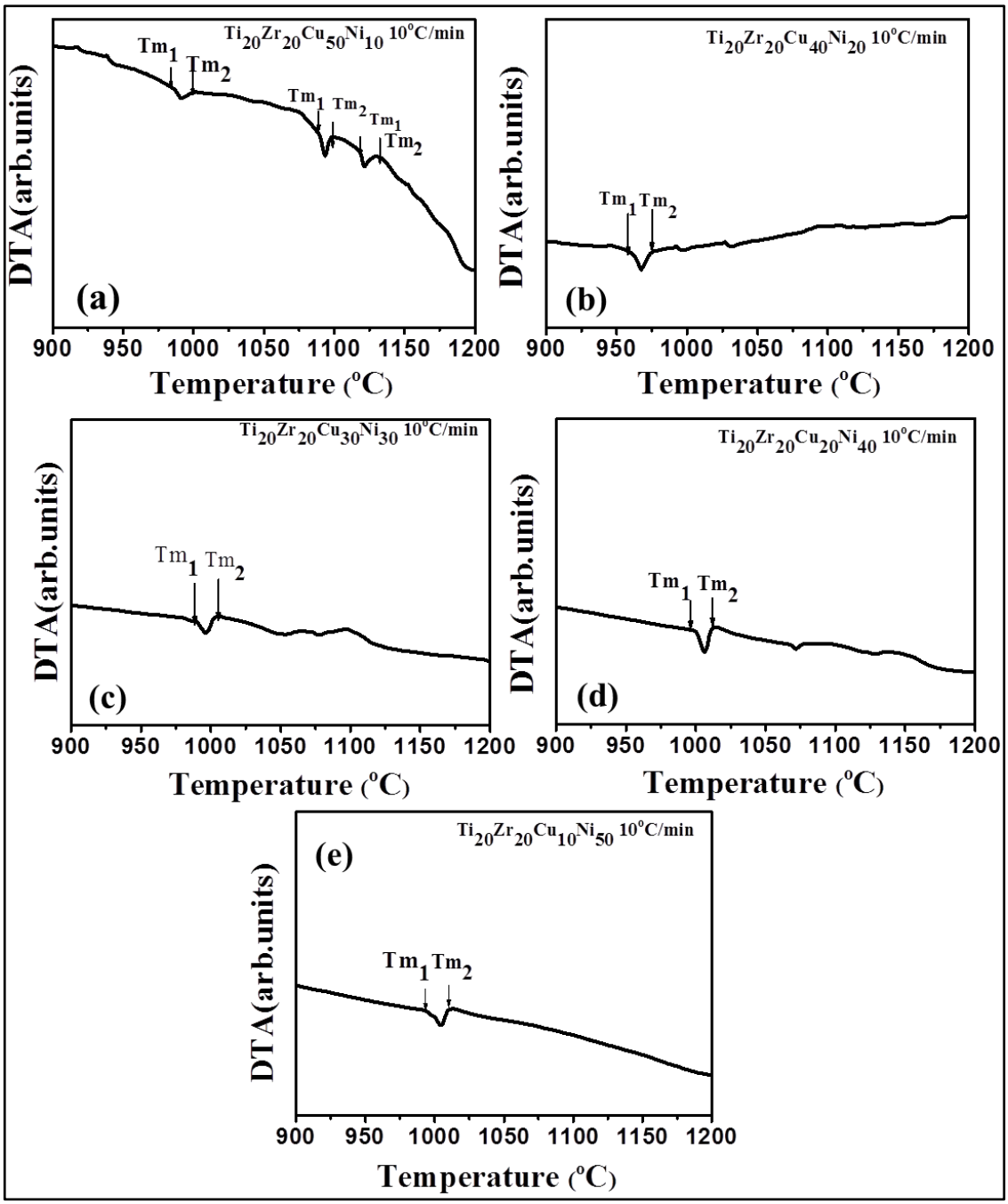


Fig.5.1 DTA curves of $Ti_{20}Zr_{20}Cu_{60-x}Ni_x$ (x=10, 20, 30, 40 and 50) metallic glasses

### 5.4 Microstructural Analysis of Brazed Joints

Regarding the methodology of the brazing joints, it has been described in detail in Chapter-2. The pure commercial Ti was used for the base metal during the investigation. Purpose of this investigation was to braze two pieces of CP-Ti using the $Ti_{20}Zr_{20}Cu_{60-x}Ni_x$ (x=10, 20, 30, 40 and 50) metallic glass ribbons of 50μm thickness as the filler material. Afterwards, in order to join Ti by the isothermal holding at corresponding brazing temperatures for a period of 10 min under a pressure of $5\times10^{-5}$ Pa and then cooled in the furnace, in Ar inert atmosphere employing vacuum brazing technique. The cross-sections of the brazing joints samples were characterized by field emission scanning electron microscopic (FESEM) and energy-dispersive X-ray spectrometric (EDX) techniques with a spot size of 1 μm.

### 5.4.1 The Microstructure analysis of $Ti_{20}Zr_{20}Cu_{60-x}Ni_x$ (x=10, 20, 30, 40 and 50) metallic glass brazed joints at corresponding brazing temperatures for a period 10 min

The FESEM analyses including EDX of $Ti_{20}Zr_{20}Cu_{60-x}Ni_x$ (x=10, 20, 30, 40 and 50) brazed joint composites at corresponding brazing temperatures are shown in Figures, 5.2-5.21.

#### 5.4.1.1 $Ti/Ti_{20}Zr_{20}Cu_{50}Ni_{10}/Ti$

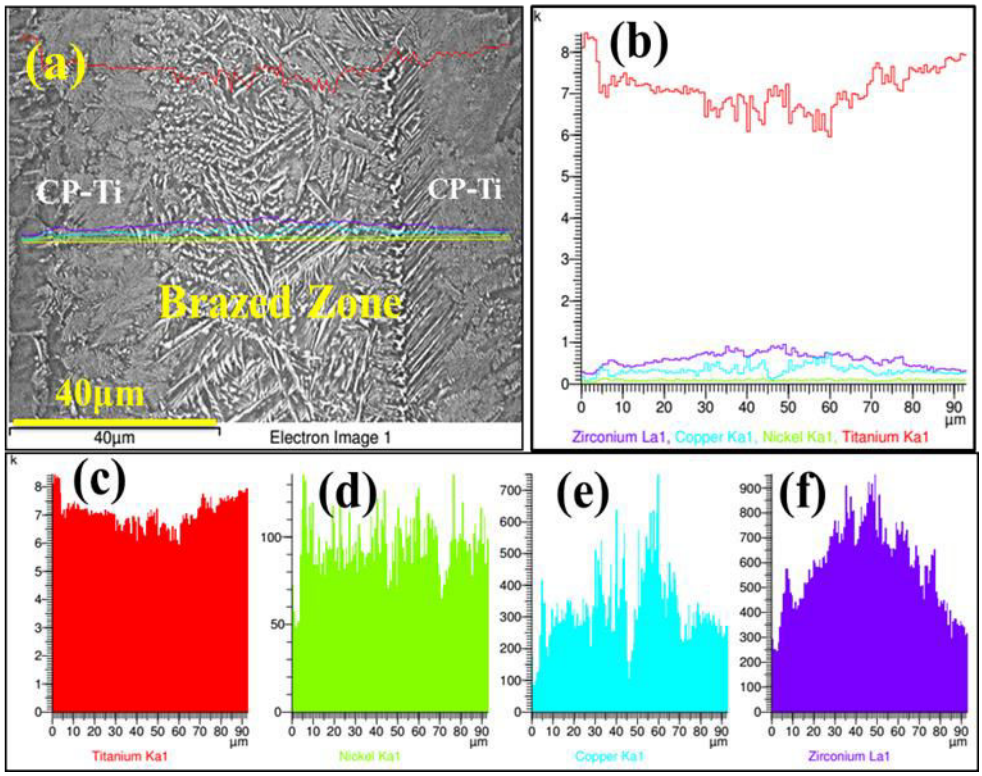


Fig. 5.2 FESEM analysis of $Ti/Ti_{20}Zr_{20}Cu_{50}Ni_{10}/Ti$ composite brazed joint at 990°C for period of 10 min: (a) Cross sectional BSE image, (b) corresponding EDX based line scan analysis across 40µm length comprising the CP-Ti pieces on both sides of brazed joint, corresponding concentration profiles of elements :(c) Ti, (d) Ni (e) Cu and (f) Zr.

Figure 5.2 (a) shows the cross sectional BSE image of the $Ti/Ti_{20}Zr_{20}Cu_{50}Ni_{10}/Ti$ composite joint. It has been indicated in Fig 5.2 (a) that the joint was devoid of imperfections (in respect of cracks and voids) and soundly bonded. It appears that there was possibly a vigorous interfacial interaction which had occurred during the brazing process and there must be a chemical reaction between the Ti substrate and molten

metallic glass filler including involvement of dissolution and diffusion [6]. A good wetting and strong bonding between the substrates and filler alloy has been observed from these results. The continuous and formation of sound interfacial reaction layers at the interface between the brazing alloy and substrates, which were shown in Fig. 5.2 (a). It was appeared that the average thickness of the reaction layer found to be about 50 µm and formed at the interface of Ti-alloy/brazed material [7]. The thickness of the gap between reaction layer and Ti-alloy was only around 1µm. As shown in Figure 5.2 a, both reaction layers were primarily composed of Ti.In Fig, 5.2 (b), the corresponding EDX based line scan analysis is shown across 40 µm length comprising of the CP-Ti pieces on both sides of brazed joints [8].It indicates that the amount of Ti slightly varied at the interface in comparison to its presence at the middle of the brazed joint. Compared to that of Ti, the amounts of Ni, Cu and Zr were a little on the lower side. The distribution of the primary elements across the brazing seam was obtained by EDX in order to describe the atomic behaviour at the solid/liquid interface [9]. Thus, the corresponding concentration profiles of Ti, Ni, Cu and Zrare given in Figs,5.2(c), (d), (e)and (f), respectively [10-15]. Similarly, the corresponding EDX based X-ray maps of the elemental distribution of Ti, Zr, Cu and Ni are indicated in Figs,5.3(a), (b),(c) and (d), respectively.

Although the presence of Ti was throughout across the brazed joint, there was a relative increase near the interface region where the reaction had initially started, Fig.5.2 (c).From Fig.5.3 (a), it appears that Ti concentration is less in brazed region. Similarly, the amounts of Cu (Fig.5.2e) and Zr (Fig.5.2f) were more at the centre of the brazed joint but became slightly lesser at the vicinity of the interface [6]. However, Ni (Fig.5.2d) appeared to be nearly uniformly distributed across the span of the brazed joint.

The amount of both dissolved Ti and Ti-alloy, and the diffusion rate of Cu in the filler metal were relatively high (because the concentration of Ti in the filler material is very small compared to base material) due to the appearance of a high concentration of Cu in the whole brazing experiment. Meanwhile, after reducing the concentration in the filler, the diffusion of Zr, Ni and Cu atoms from filler into the Ti substrate occurred. In other words, because of the interfacial interaction, the transformation of the quaternary Ti-Zr-Cu-Ni to a series of liquid of Ti-Zr-Cu-Ni system took place with unknown compositions. It is quite obvious that the occurrence of joint microstructure during isothermal solidification and cooling of the Ti-Zr-Cu-Ni molten pool were due to complicated behaviour. In the binary phase diagrams of Ti-Zr and Cu-Ni, it is known that both the Ti and Zr, and Cu and Ni element pairs not only have similar atomic radii and crystal structure, but also are fully miscible with one another [3, 17, 18]. These observations are in good agreement with the X-ray maping data of Ti, Zr,Cu and Ni, as depicted in Figs.5.3(a), (b), (c) and (d), respectively [19].

The FESEM image of the interface microstructures of Ti/$Ti_{20}Zr_{20}Cu_{50}Ni_{10}$/Ti composite brazing joint at 990$^{o}$Cdemonstrated the following four zones: Ti rich diffusion 1, Ti rich diffusion 2, the discontinuous reaction and the central zones are given in Figs.5.4 (a), (b), (c) and (d), respectively. To have an approximate idea of the elemental compositions of these regions, EDX spectra were taken from Ti-rich phase,α-Ti rich phase, $(Ti,Zr)_2Cu$ and eutectoid rich region, which are depicted in Figs5.4 (a), (b), (c)and (d), respectively.

The EDX spectra collected from diffusion zone 1, diffusion zone 2, discontinuous reaction zone and central zone, are shown in Figs.5.5 (a), (b), (c) and (d), respectively. Approximate average chemical compositions obtained from such numerous experiments are shown in Table 5.2.

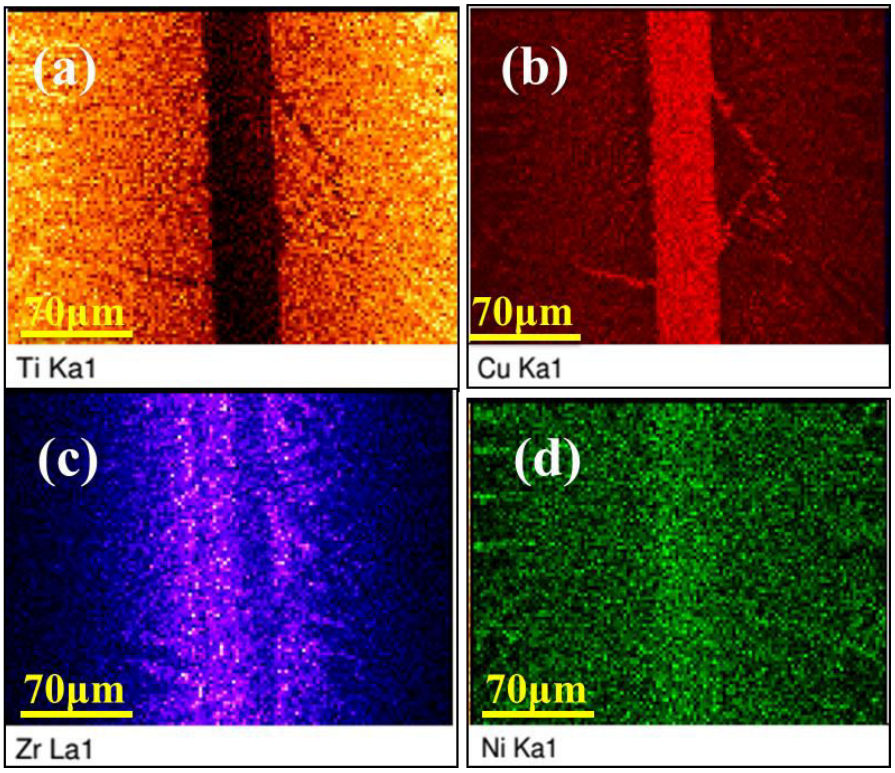


Fig. 5.3 FESEM analysis of Ti/ $Ti_{20}Zr_{20}Cu_{50}Ni_{10}$ /Ti composite joint brazed at 990°C for 10 min. EDX based X-ray Maps of the distribution of various elements across the brazed joint (a) Ti, (b) Cu, (c) Zr and (d) Ni.

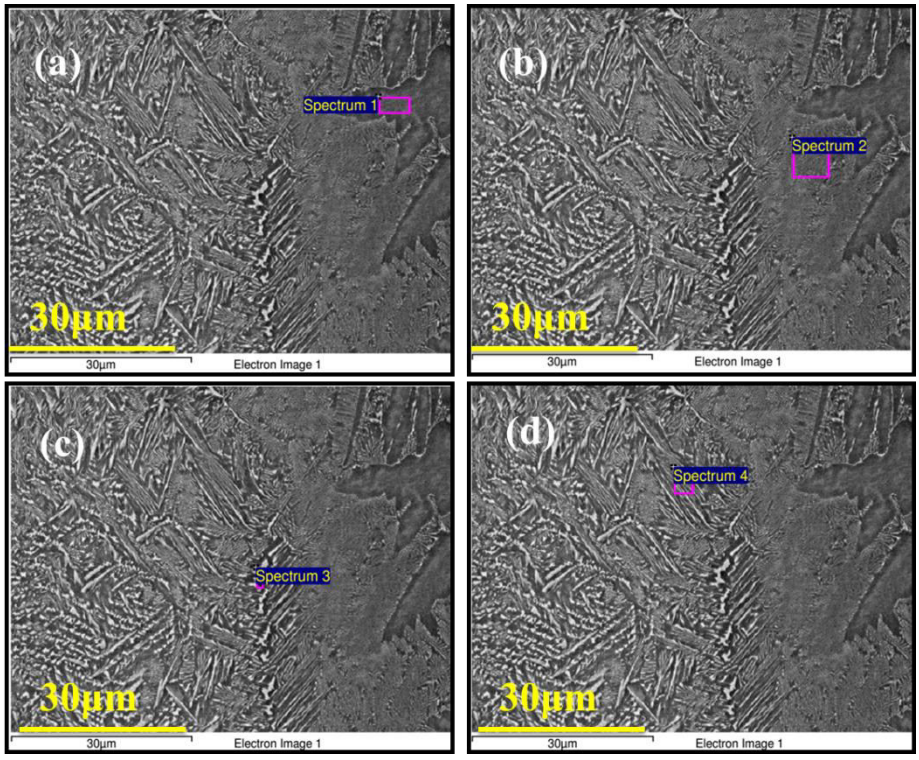


Fig.5.4 Further FESEM images of the interface microstructures of Ti/ $Ti_{20}Zr_{20}Cu_{50}Ni_{10}$ /Ti composite brazed joint at 990°C for a period of 10 min: (a) Diffusion zone 1 (b) diffusion zone 2, (c) discontinuous reaction zone and (d) central zone.

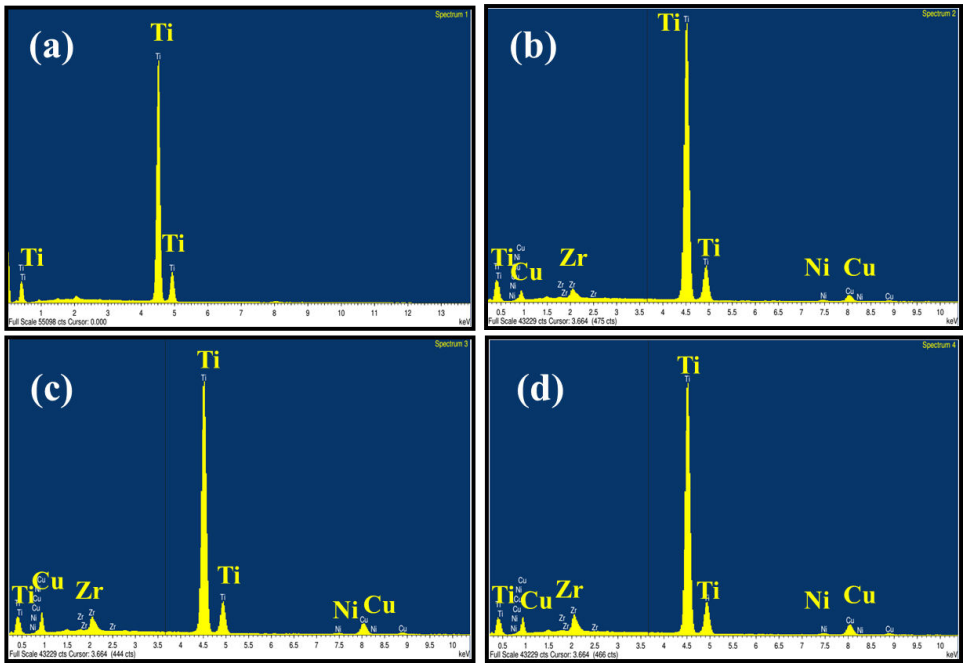


Fig.5.5TheEDXspectra of the interface microstructures of Ti/$Ti_{20}Zr_{20}Cu_{50}Ni_{10}$/Ti composite joint brazed at 990°C for 10 min:

Table 5.2 EDX analyses based elemental chemical composition analysis of interface microstructures of Ti/ $Ti_{20}Zr_{20}Cu_{50}Ni_{10}$/Ti composite brazing joint 990°C

| Area | Elements (at. %) | | | | | |
|---|---|---|---|---|---|---|
| | Ti | Zr | Cu | Ni | Phases | |
| Spectrum 1 | 100.00 | --- | --- | -- | Ti-rich | |
| Spectrum 2 | 91.35 | 2.07 | 5.63 | 0.95 | α-Ti | Ref[4] |
| Spectrum 3 | 85.56 | 3.30 | 10.32 | 0.82 | $(Ti, Zr)_2Cu$ | Ref[5] |
| Spectrum 4 | 85.60 | 3.86 | 9.53 | 1.02 | Eutectoid | Ref[3] |

Thus, on the basis of the experimental data displayed in Figs 5.2-5.5 and Table 5.2, it appears possible to suggest the following processes to have occurred during the brazed joint formation: During the isothermal solidification of the molten brazed and had eventually formed primary β-Ti, the residual melt was solidified via eutectic reaction upon the cooling cycle of brazing. Based on the data of Table 5.2, the eutectic consisted most probably of $(Ti,Zr)_2Cu$, α-Ti and Ti-rich as shown in Figs.5.4 (a-d) and 5.5 (a-d). The β-Ti is totally soluble with Zr according to related binary alloy phase diagrams [3].

The maximum solubilities of Cu and Ni in the β-Ti phase are 33.5 and 8 at. %, respectively. In contrast, Cu and Ni are dissolved in α-Ti phase up to 1.6 and 0.2 at. %, respectively [20]. These values are significantly lower than their respective solubilities in β-Ti phase. Both Cu and Ni are hence well known to be stabilizers of the β-phase in CP-Ti. On cooling to room temperature, formation of both β-Ti phase and intermetallic compounds may take place. Accordingly, decomposition of the β-Ti phase might have most likely proceeded via eutectoid solid-state transformation upon the cooling cycle of brazing. The eutectoid of $(Ti,Zr)_2Cu$, α-Ti and Ti-rich might therefore have had formed at room temperature in the earlier β-Ti grains of the brazed joint [5, 21, 22].Higher brazing temperature resulted possibly in higher volume fraction of the β-Ti in the joint. This process had greatly enhances the depletion rates of Cu, Ni, and Zr from the brazed melt into CP-Ti substrate during brazing. Because Cu, Ni, and Zr are all dissolved in the β-Ti, isothermal solidification of brazed melt during brazing resulted in formation of only β-Ti in the joint. Thus, the eutectic of $(Ti,Zr)_2Cu$, α-Ti and Ti-rich had most likely disappeared from the brazed zone. The β-Ti alloyed with Cu, Ni, and Zr was therefore most likely to have had transformed to fine eutectoid of $(Ti, Zr)_2Cu$, α-Ti and Ti-rich upon the subsequent cooling cycle of brazing. It is expected that the disappearance of coarse eutectic intermetallic compounds from the brazed zone is beneficial for enhancing the bond strength of the joint [23-27].

### 5.4.1.2 Ti/$Ti_{20}Zr_{20}Cu_{40}Ni_{20}$/Ti

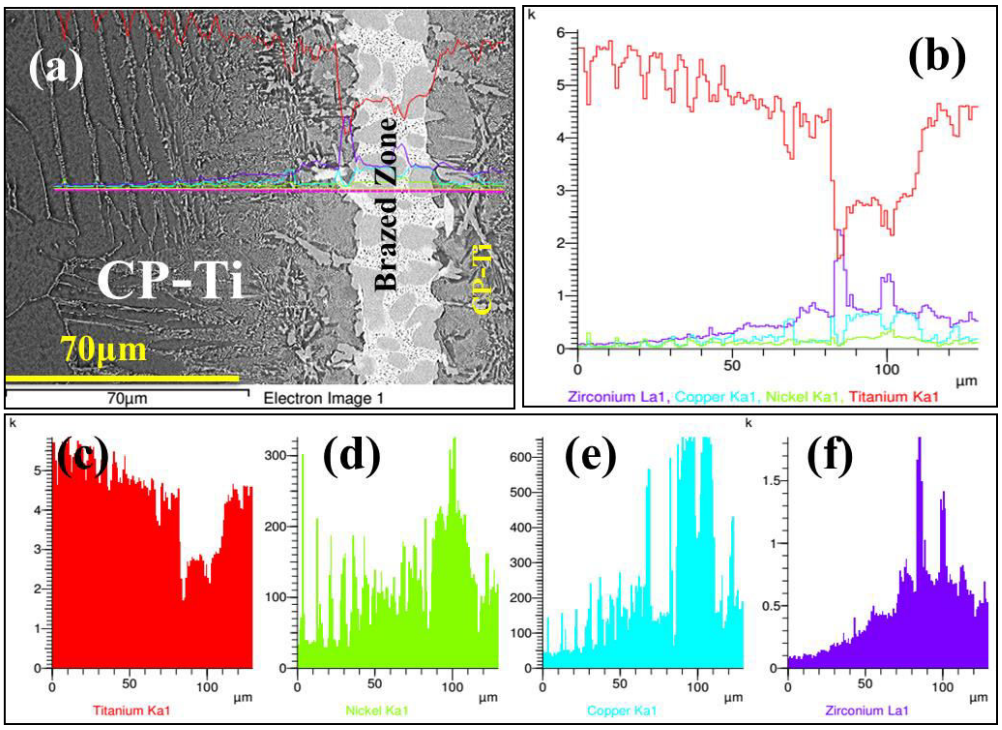


Fig. 5.6 FESEM analysis of Ti/ $Ti_{20}Zr_{20}Cu_{40}Ni_{20}$ /Ti composite joint brazed at 967°C for 10 min. (a) Cross sectional BSE Image (b) corresponding EDS based line scan analysis across 130 µm length comprising the CP-Ti pieces on both sides of brazed joint, corresponding concentration profiles of elements :(c)Ti, (d)Ni (e) Cu and (f) Zr.

Similar morphological phenomena and phase behaviours are also observed for the remaining four brazed joint metallic glasses from FESEM and EDX, which are shown in Figs.5.6-5.9. The corresponding elemental compositions are depicted in Table 5.3. The average thickness of the reaction layer appeared to be about 30µm.The corresponding EDX based line scan analysis across 130 µm length comprising of the CP-Ti pieces on both sides of brazed joint is indicated in Fig5.6 (b). Corresponding concentration profiles of Ti, Ni, Cu and Zr are given in Figs.5.6(c), (d), (e) and (f), respectively. Figs. 5.7 (a), (b), (c) and (d) represent the elemental mapping. In Fig5.6 (c) Ti-concentrationis low in brazen zone compared to base metal. At about 80 µm from the interface, the amount of Ti dropped to its minimum magnitude prior to going up further from this point onwards when reaching the interface on the opposite side.

The amounts of Ni (Figure 5.6d) and Cu (Figure 5.6e) were relatively smaller at the centre of the brazed joint (e.g., at about 50 μm from the interface on the left) but became highest at a point about 100 μm from the left and about 30 μm from the right side interface. Beyond this 100 μm distance, the amounts of both Ni (Figure 5.6d) and Cu (Figure 5.6d) decreased as the right side interface of the brazed joint is approached.

On the other hand, the amount of Zr (Figure 5.6f) appeared to be the minimum near the left interface. Its amount became the highest at about 85 μm from the interface on the left. Here also, beyond this 85 μm distance, the amount of Zr (Figure 5.6f) decreased as the right side interface of the brazed joint is approached. The inhomogeneous and non-uniform distribution of Ni, Cu and Zr across the interface hinted that by reducing the concentration in the filler, the diffusion of Zr, Cu and Ni atoms from filler into Ti substrate took place at the solid interface.

Ti-rich, NiTi2 rich, α-Ti and $Ti_2Cu$ phases are extracted from EDX spectra and given in Figs. 5.8 (a), (b), (c) and (d), respectively. The solubilities of Cu and Ni are maximum in the β-Ti phase at 26.5 and 17 at. %, respectively. In contrast, Cu and Ni are solubilized in α-Ti phase up to 2.4 and 0.4 at.%, respectively.

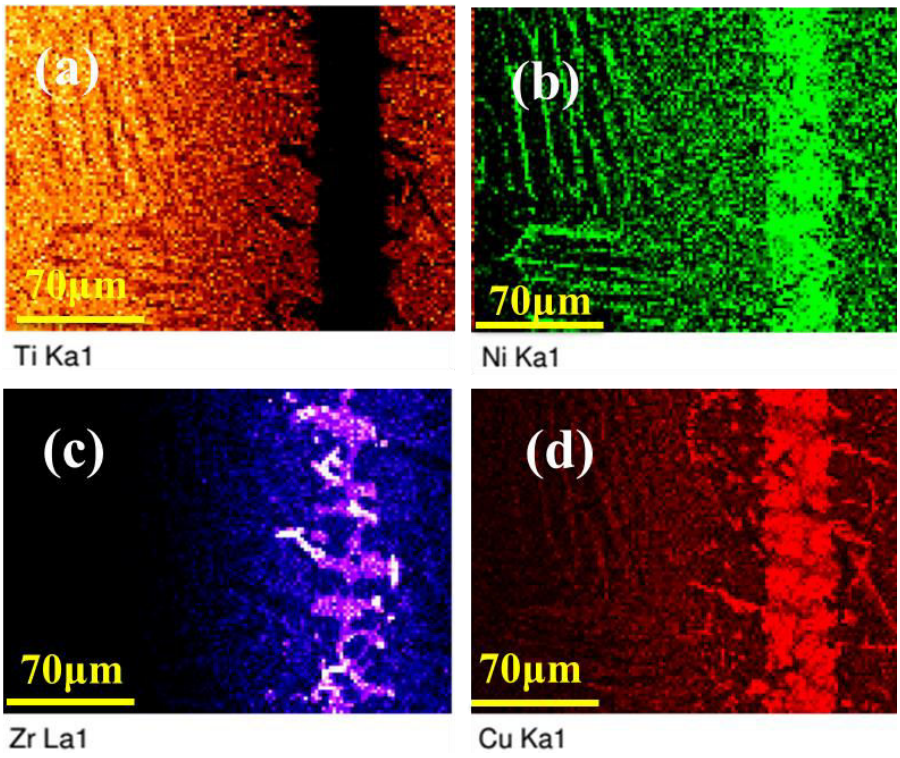


Fig. 5.7 FESEM analysis of Ti/ $Ti_{20}Zr_{20}Cu_{40}Ni_{20}$ /Ti composite joint brazed at 967°C for 10 min. EDX based X-ray Maps of the distribution of various elements across the brazed joint (a) Ti, (b) Ni, (c) Zr and (d) Cu.

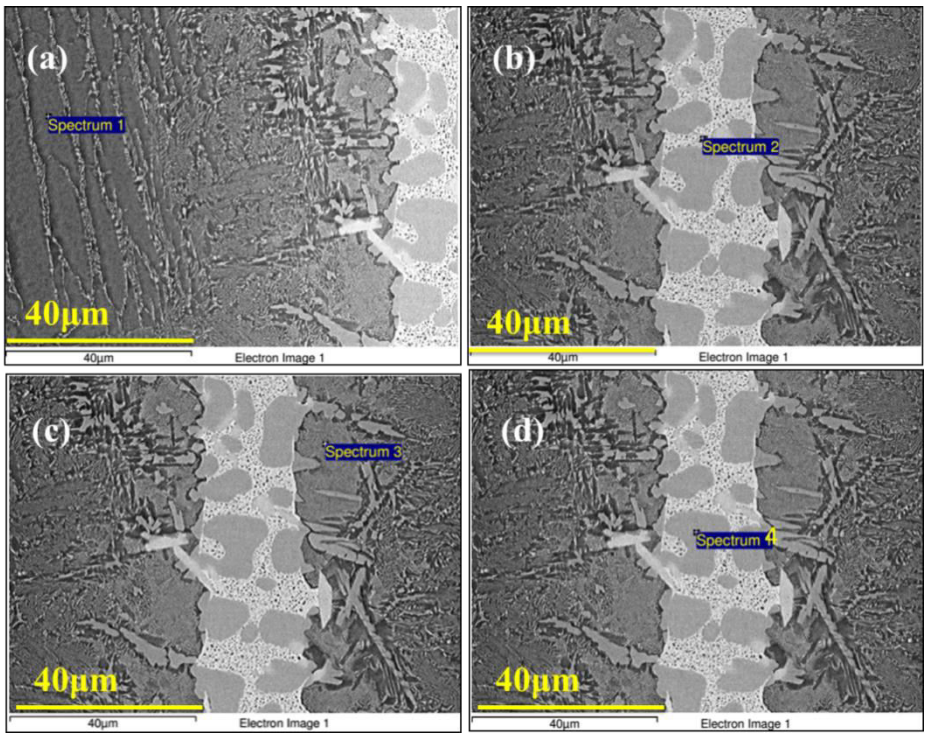


Fig.5.8 Further FESEM studies of the interface microstructures of Ti/ $Ti_{20}Zr_{20}Cu_{40}Ni_{20}$ /Ti composite joint brazed at 997°C for 10 min: (a) Diffusion zone 1 (b) diffusion zone 2, (c) discontinuous reaction zone and (d) central zone.

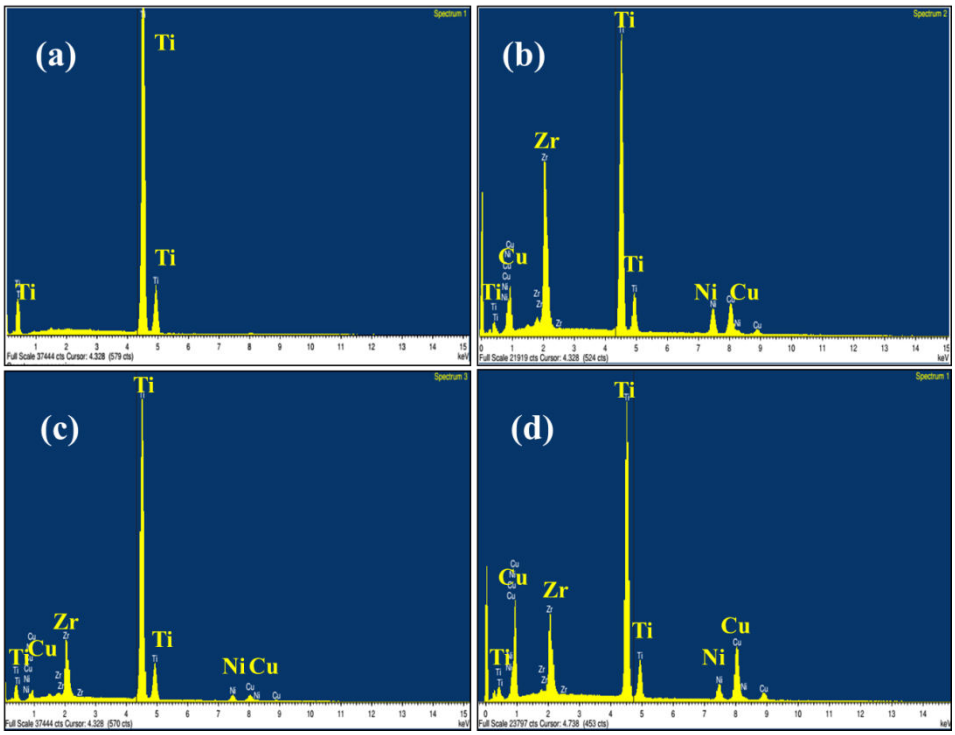


Figure 5.9 EDX spectra of the interface microstructures of Ti/ $Ti_{20}Zr_{20}Cu_{40}Ni_{20}$ /Ti composite brazed joint at 997°C for a period of 10 min.

Table 5.3 EDX analyses based elemental chemical composition analysis of interface microstructures of Ti/ $Ti_{20}Zr_{20}Cu_{40}Ni_{20}$/Ti composite brazing joint at 967°C

| Area | Elements (at. %) | | | | | |
|---|---|---|---|---|---|---|
| | Ti | Zr | Cu | Ni | Phases | |
| Spectrum 1 | 100.00 | --- | --- | --- | Ti-rich | |
| Spectrum 2 | 55.08 | 20.20 | 14.68 | 10.04 | $NiTi_2$ | Ref[4] |
| Spectrum 3 | 82.26 | 9.90 | 4.47 | 3.37 | α-Ti | Ref[3] |
| Spectrum 4 | 55.79 | 10.88 | 26.66 | 6.67 | $Ti_2Cu$ | Ref[3] |

### 5.4.1.3Ti/$Ti_{20}Zr_{20}Cu_{30}Ni_{30}$/Ti

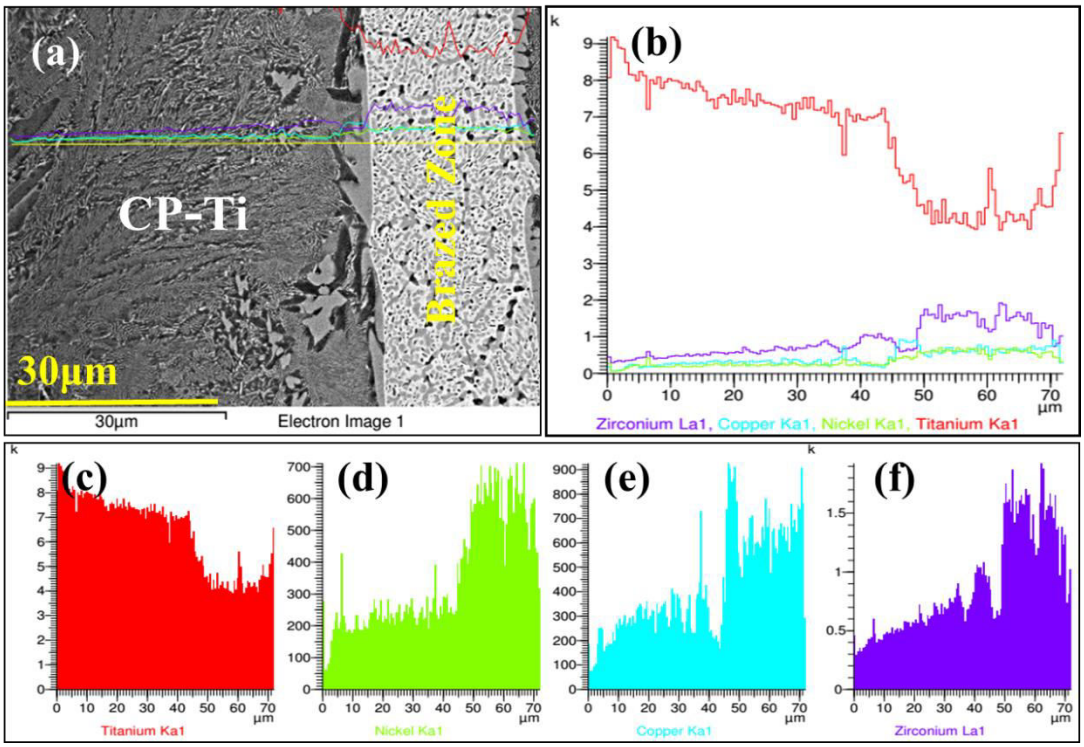


Fig. 5.10 FESEM analysis of Ti/ $Ti_{20}Zr_{20}Cu_{30}Ni_{30}$ /Ti composite joint brazed at 995°C for 10 min (a) Cross sectional BSE Image (b) corresponding EDS based line scan analysis across 30µm length comprising the CP-Ti pieces on both sides of brazed joint, corresponding concentration profiles of elements :(c)Ti, (d)Ni (e) Cu and (f) Zr.

The respective EDX based line scan analysis across 70µm length comprising of the CP-Ti pieces on both sides of brazed joint is shown in Fig.5.10 (b). The reaction layer appeared to have an average thickness of about 40µm. It shows that the amount of Ti was maximum at the left side interface of the joint and was minimum at about 50 to 65 mm from the same interface.Beyond this point the amount of Ti slightly increased as the right side interface of the joint was approached.

The corresponding elemental compositions are depicted in Table 5.4.Corresponding concentration profiles of Ti, Ni, Cu and Zr are given in Figs.5.10 (c), (d), (e) and (f), respectively. Figs. 5.11(a), (b), (c) and (d) represent the elemental mapping. Although Ti was throughout across the brazed joint, there was a relative increase near the left interface region where the reaction had initially started, Figure 5.10 (c).

The EDX spectra of $Ti_2Cu$, $(Ti,Zr)_2Ni$, α-Ti and Ti-rich phases are shown in Figs.5.12 (a), (b), (c) and (d), respectively. These EDX spectrawith corresponding elemental compositions are shown in Fig. 5.13 (a), (b), (c) and (d), respectively and given in Table 5.4.Amounts of Ni (Figure 5.10 d) and Cu (Figure 5.10e) were the minimum at the left interface and grew to their respective maximum positions at about 65 and 50 μm from the left interface. Similarly, the amount of Zr (Figure 5.10f) was the minimum at the left interface and grew to its maximum positions at about 55 to 60 μm from the left interface. The solubilities of Cu and Ni are maximum in the β-Ti phaseat 28.5 and 28 at.%, respectively. In contrast, Cu and Ni are dissolved in α-Ti up to 1.4 and 1.4 at.%, respectively. Thus, the eutectic of eutectoid of $Ti_2Cu$, $(Ti,Zr)_2Ni$, α-Ti and Ti-rich phases had most likely disappeared from the brazed zone. The β-Ti alloyed with Cu, Ni, and Zr was therefore most likely to have had transformed to fine eutectic of eutectoid of $Ti_2Cu$, $(Ti,Zr)_2Ni$, α-Ti and Ti-rich phases upon the subsequent cooling cycle of brazing.

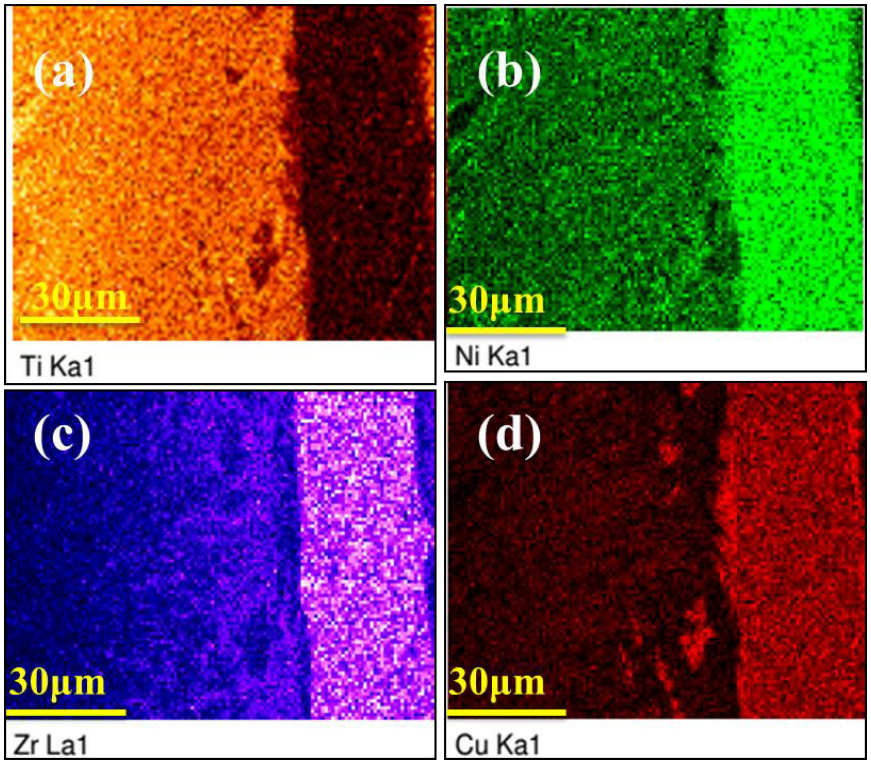


Fig. 5.11 FESEM analysis of Ti/ $Ti_{20}Zr_{20}Cu_{30}Ni_{30}$ /Ti composite joint brazed at 995°C for 10 min. EDX based X-ray Maps of the distribution of various elements across the brazed joint (a) Ti, (b)Ni, (c) Zr and (d) Cu.

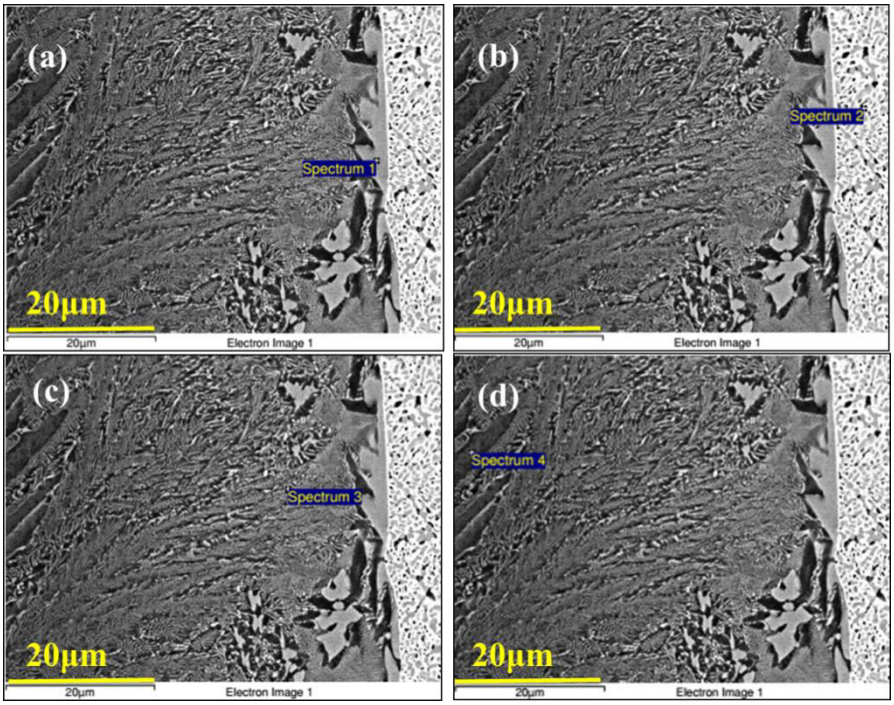


Fig.5.12 Further FESEM study of the interface microstructures of Ti/ $Ti_{20}Zr_{20}Cu_{30}Ni_{30}$ /Ti composite joint brazed at 995°C for 10 min: (a) Diffusion zone 1 (b) diffusion zone 2, (c) discontinuous reaction zone and (d) central zone.

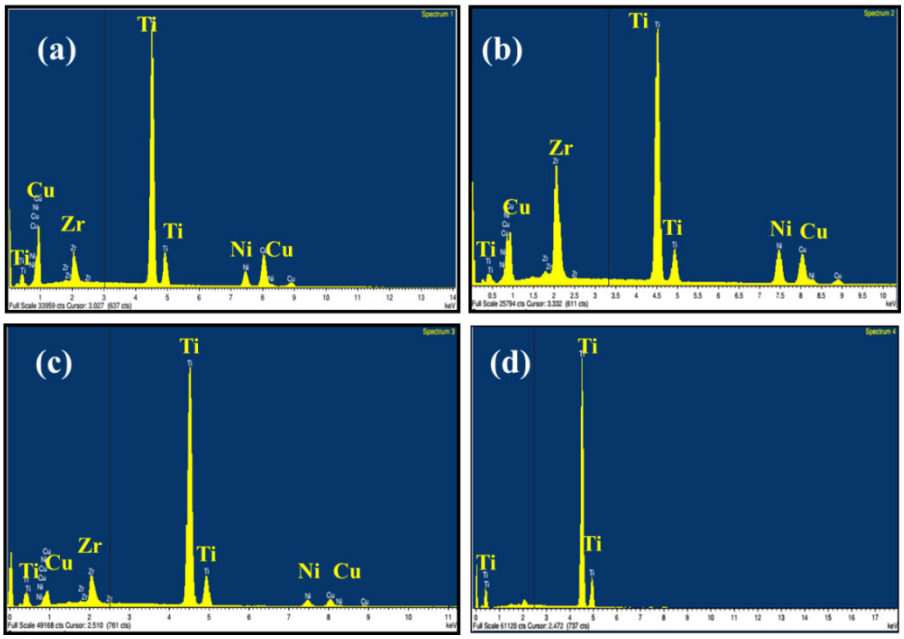


Fig 5.13 EDX spectra of the interface microstructures of Ti/ $Ti_{20}Zr_{20}Cu_{30}Ni_{30}$ /Ti composite joint brazed at 995°C for 10 min: (a) Spectrum 1 collected from Diffusion zone 1 shown in Figure 12 (a), (b) Spectrum 2 collected from Diffusion zone 2 shown in Figure 12 (b), (c) Spectrum 3 collected from discontinuous reaction zone shown in Figure 12(c) and (d) Spectrum 4 collected from central zone shown in Figure 12 (d).

Table 5.4 EDX analyses based elemental chemical composition analysis of interface microstructures of Ti/ $Ti_{20}Zr_{20}Cu_{30}Ni_{30}$ /Ti composite brazing joint at 995°C

| Area | Elements (at.%) | | | | | |
|---|---|---|---|---|---|---|
| | Ti | Zr | Cu | Ni | Phases | |
| Spectrum 1 | 64.45 | 5.61 | 21.61 | 8.33 | $Ti_2Cu$ | Ref[3] |
| Spectrum 2 | 52.48 | 16.09 | 16.22 | 15.21 | $(Ti, Zr)_2Ni$ | Ref[3] |
| Spectrum 3 | 82.24 | 6.27 | 6.60 | 4.90 | α-TiRef[3] | |
| Spectrum 4 | 100.00 | --- | --- | --- | Ti-rich | |

### 5.4.1.4Ti/$Ti_{20}Zr_{20}Cu_{20}Ni_{40}$/Ti

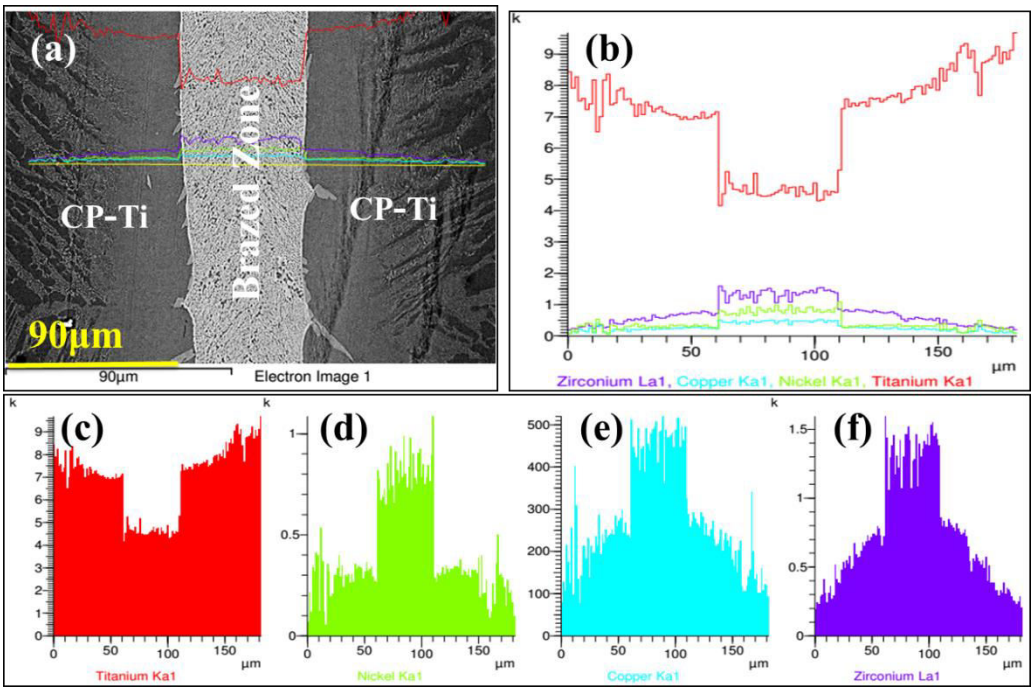


Fig. 5.14 FESEM analysis of Ti/ $Ti_{20}Zr_{20}Cu_{20}Ni_{40}$ /Ti composite joint brazed at 1004°C for 10 min (a) Cross sectional BSE Image (b) corresponding EDX based line scan analysis across 90 µm length comprising the CP-Ti pieces on both sides of brazed joint, corresponding concentration profiles of elements :(c)Ti, (d)Ni (e) Cu and (f) Zr.

The continuous and interfacial reaction layers (appeared to have an average thickness of about 40µm) formed at the interface between the brazing alloy and substrates are indicated in Fig5.14(a).The corresponding EDX based line scan analysis across 180 µm length comprising of the CP-Ti pieces on both sides of brazed joint is depicted in Fig 5.14(b). It shows that the amount of Ti was maximum at the vicinity of interface on both sides but it was minimum at the region from about 60 to 110 µm from the left interface.Similarly, the corresponding EDX based X-ray maps of the elemental distribution of Ti, Zr, Cu and Ni are shown in Figure 5.15(a), (b), (c) and (d), respectively. While the presence of Ti was throughout across the brazed joint, there was a relative increase near the interface region where the reaction had initially started, Fig5.14 (c). Similarly, the amounts of Ni (Fig5.14d), Cu (Fig5.14e) and Zr (Fig5.14f) were more at the centre of the brazed joint but became slightly lesser at the vicinity of the

interface.These observations are in good agreement with the X-ray map data of Ti, Zr, Cu and Ni (*cf*. Figs5.15 a-d). The EDX spectra of $NiTi_{2,}(Ti,Zr)_2Ni$, β-(Ti,Zr) and Ti-rich phases are shown in Figs.5.16 (a), (b), (c) and (d), respectively. These EDX spectrawith corresponding elemental compositions shown in Fig. 5.17 (a), (b), (c) and (d), respectively and given in Table 5.5.

The solubilities of Cu and Ni in the β-Ti phase aremaximum at 18.5 and 38 at.%, respectively. In contrast, Cu and Ni are dissolved in α-Ti up to 0.4 and 2.4at.%, respectively. Thus, the eutectic of $NiTi_2$, $(Ti,Zr)_2Ni$, β-(Ti,Zr) and Ti-rich phases had most likely disappeared from the brazed zone.

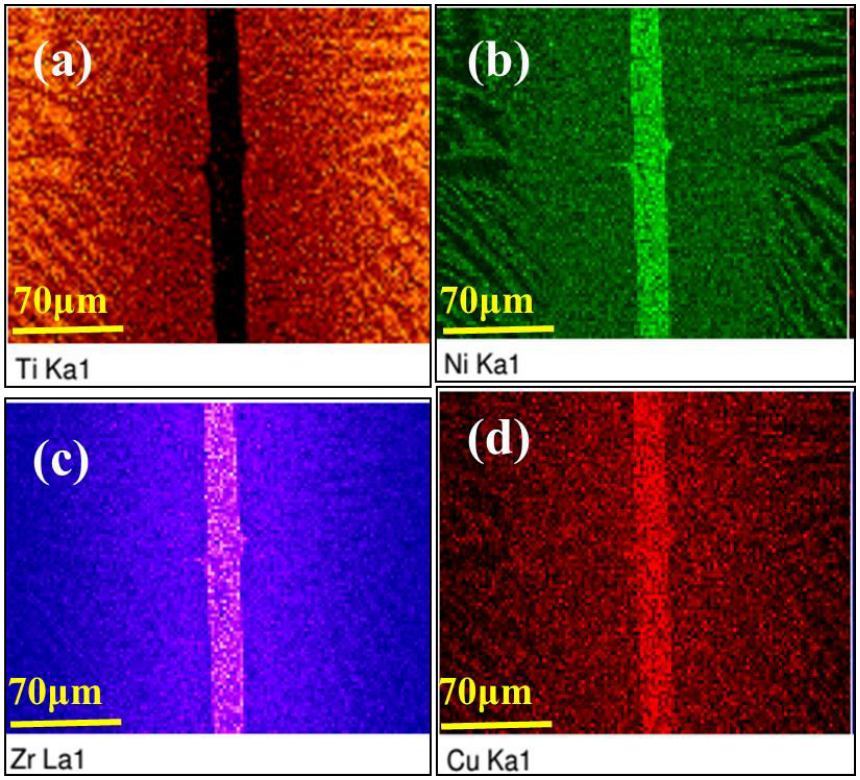


Fig. 5.15 FESEM analysis of Ti/ $Ti_{20}Zr_{20}Cu_{20}Ni_{40}$ /Ti composite joint brazed at 1004°C for 10 min. EDX based X-ray Maps of the distriution of various elements across the brazed joint (a) Ti, (b)Ni, (c) Zr and (d) Cu.

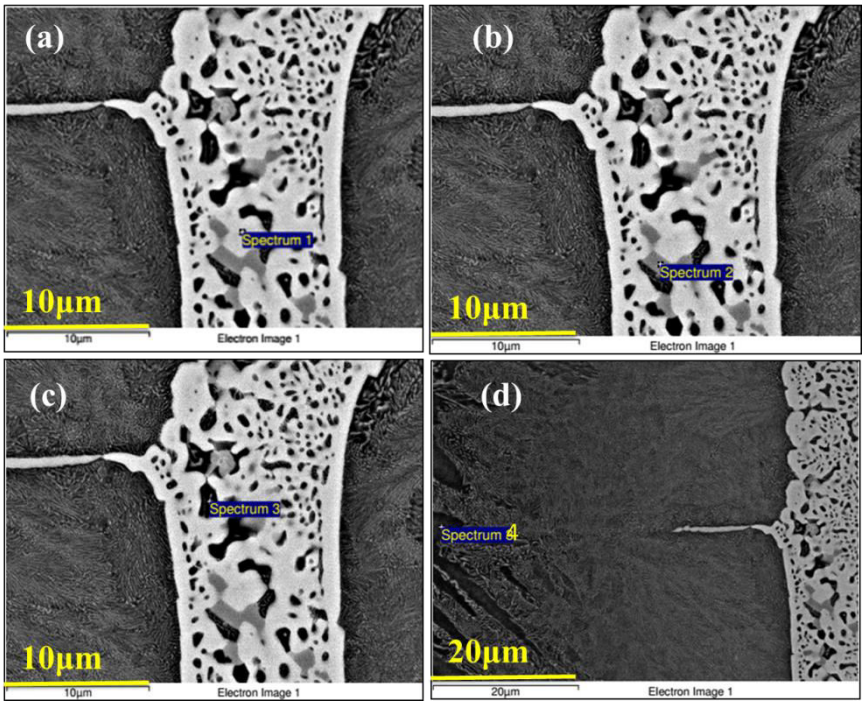


Fig.5.16 Further FESM study of the interface microstructures of Ti/ $Ti_{20}Zr_{20}Cu_{20}Ni_{40}$ /Ti composite joint brazed at 1004°C for 10 min: (a) Diffusion zone 1 (b) diffusion zone 2, (c) discontinuous reaction zone and (d) central zone.

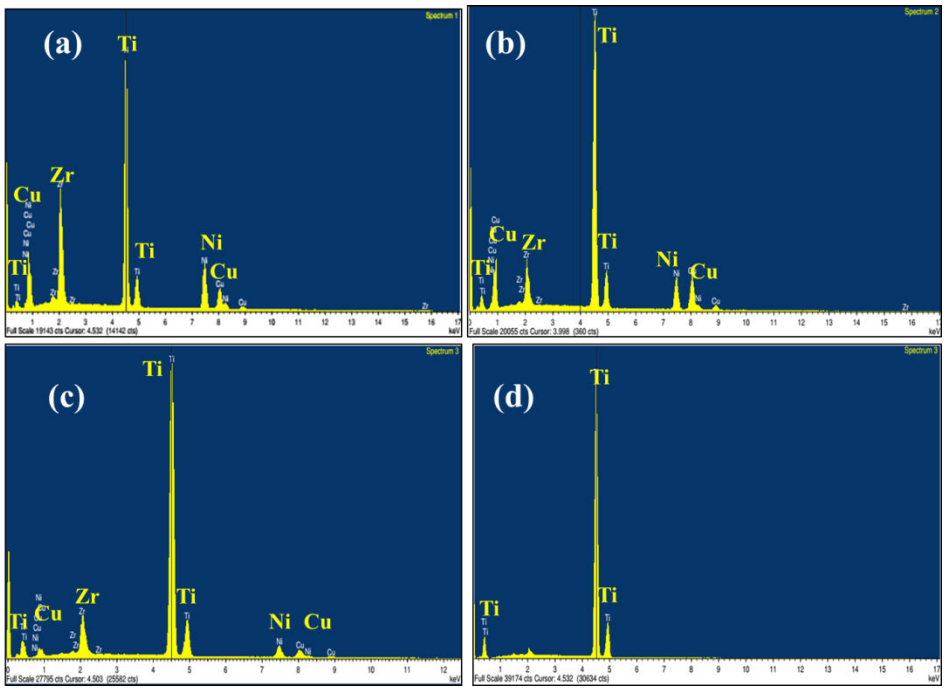


Fig 5.17 EDX spectra of the interface microstructures of Ti/ $Ti_{20}Zr_{20}Cu_{20}Ni_{40}$ /Ti composite joint brazed at 1004°C for 10 min: (a) Spectrum 1 collected from Diffusion zone 1 shown in Figure 5.17 (a), (b) Spectrum 2 collected from Diffusion zone 2 shown in Figure 5.16 (b), (c) Spectrum 3 collected from discontinuous reaction zone shown in Figure 5.16(c) and (d) Spectrum 4 collected from central zone shown in Figure 5.16(d).

Table 5.5 EDX analyses based elemental chemical composition analysis of interface microstructures of Ti/ $Ti_{20}Zr_{20}Cu_{20}Ni_{40}$ /Ti composite brazing joint at 1004°C

| Area | Elements (at. %) | | | | | |
|---|---|---|---|---|---|---|
| | Ti | Zr | Cu | Ni | Phases | |
| Spectrum 1 | 52.35 | 16.37 | 10.77 | 20.51 | $NiTi_2$ | Ref[4] |
| Spectrum 2 | 59.75 | 6.75 | 18.62 | 14.88 | $(Ti,Zr)_2Ni$ | Ref[4] |
| Spectrum 3 | 80.48 | 6.97 | 5.40 | 7.15 | β(Ti, Zr) | Ref[4] |
| Spectrum 4 | 100.00 | --- | --- | --- | Ti-rich | |

### 5.4.1.5 Ti/$Ti_{20}Zr_{20}Cu_{10}Ni_{50}$/Ti

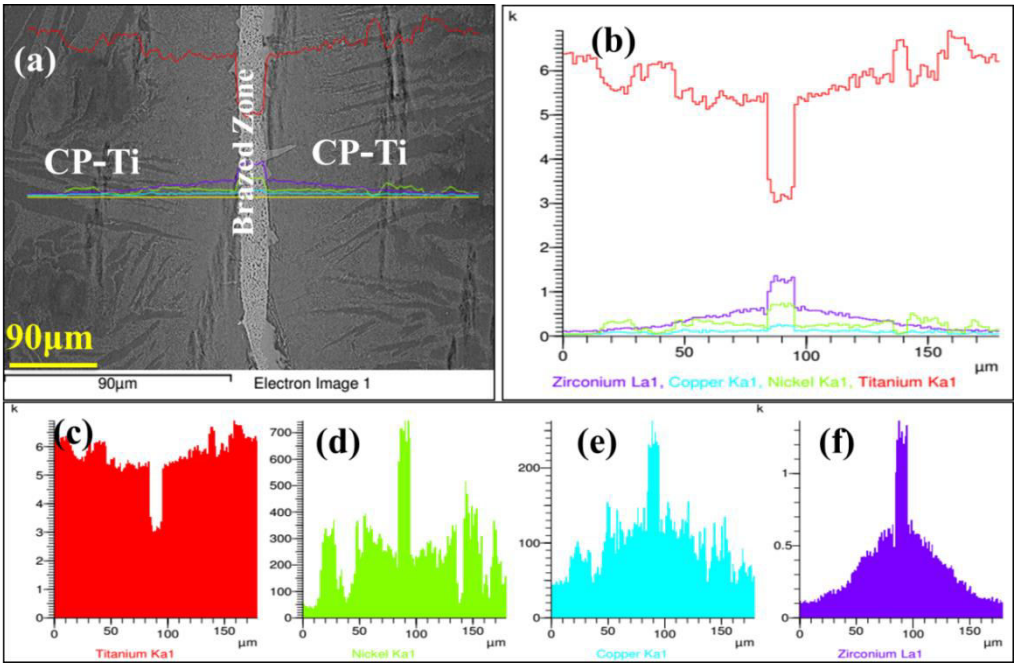


Fig. 5.18 FESEM analysis of Ti/ $Ti_{20}Zr_{20}Cu_{10}Ni_{50}$ /Ti composite joint brazed at 1006°C for 10 min (a) Cross sectional BSE Image (b) corresponding EDS based line scan analysis across 90 µm length comprising the CP-Ti pieces on both sides of brazed joint, corresponding concentration profiles of elements :(c)Ti, (d)Ni (e) Cu and (f) Zr.

Continuous and sound interfacial reaction layers (of thickness about 40 µm) are formed at the interface between the brazing alloy and the substrates. As earlier, both reaction layers were primarily composed of Ti,shown in Fig5.18 (a).The corresponding EDX based line scan analysis across 180 µm length comprising of the CP-Ti pieces on both sides of brazed joint is shown in Fig5.18(b).It shows that the amount of Ti was maximum at the vicinity of interface on both sides, but it was minimum at the region from about 85 to 95 µm from the left interface.Compared to that of Ti, the amounts of Ni, Cu and Zr were a little on the lower side. To elucidate the atomic behaviour at the solid/liquid interface, the distribution of the primary elements across the brazing seam was measured by EDX.

Thus, the corresponding concentration profiles of Ti, Ni, Cu and Zr are shown in Figs 5.18(c), (d), (e) and (f), respectively. Similarly, the corresponding EDX based X-ray maps of the elemental distribution of Ti, Zr, Cu and Ni are shown in Figs 5.19(a), (b), (c) and (d), respectively. While the presence of Ti was throughout across the brazed joint, there was a relative increase near the interface region where the reaction had initially started, Figure 5.18 (c). Similarly, the amounts of Ni (Figure 5.18d), Cu (Figure 5.18e) and Zr (Figure 5.18f) were more at the centre (e.g., at about 85 to 95 μm from the left interface) of the brazed joint but became slightly lesser at the vicinity of the interface. These observations are well corroborated by the X-ray map data of Ti, Zr, Cu and Ni as shown in Figs 5.19 (a), (b), (c) and (d), respectively. The Ti rich diffusion (4,5), discontinuous reaction (3) and central zones (1,2) are shown in Figs5.20 (a), (b), (c), (d) and (e), respectively. The EDX spectra of $NiTi_2$, $Cu_2(Ni,Zr)$, NiTi, α-Tiand Ti-rich phases shown in Fig. 5.21 (a), (b), (c), (d) and (e), respectively and the approximate average chemical compositions obtained from numerous such experiments are shown in Table 5.6.The solubilities of Cu and Ni in the β-Ti phase are maximum at 48.5 and 8 at.%, respectively. In contrast, Cu and Ni are dissolved in α-Ti phase up to 2.4 and 1.4 at. %, respectively.

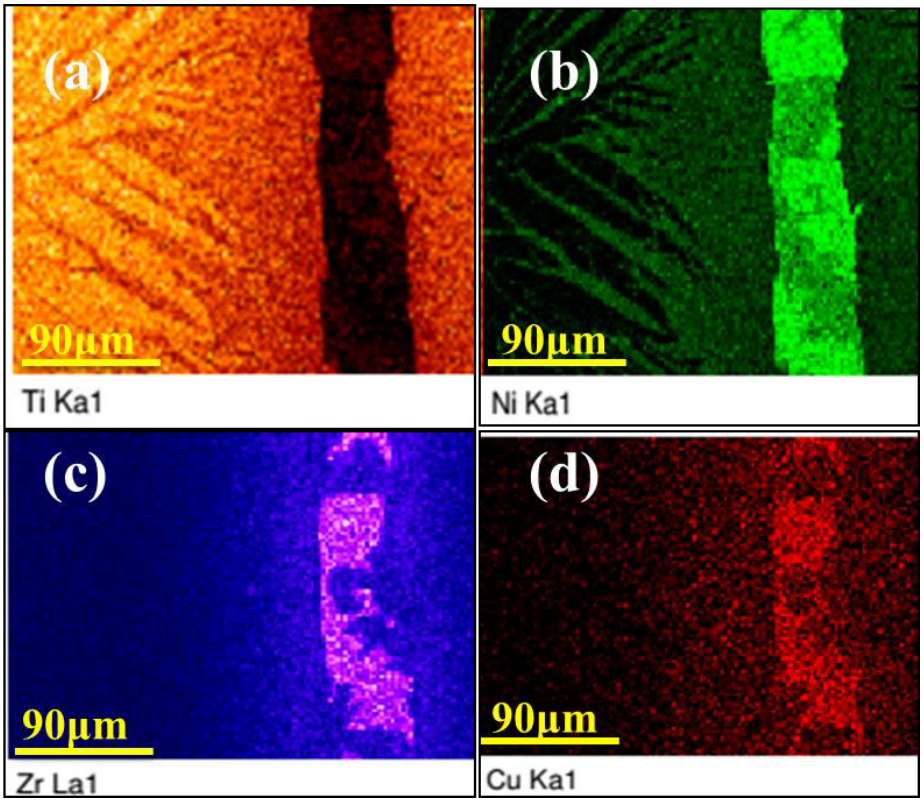


Fig. 5.19 FESEM analysis of Ti/ $Ti_{20}Zr_{20}Cu_{10}Ni_{50}$ /Ti composite joint brazed at 1006°C for 10 min. EDX based X-ray Maps of the distribution of various elements across the brazed joint (a) Ti, (b)Ni, (c) Zr and (d) Cu.

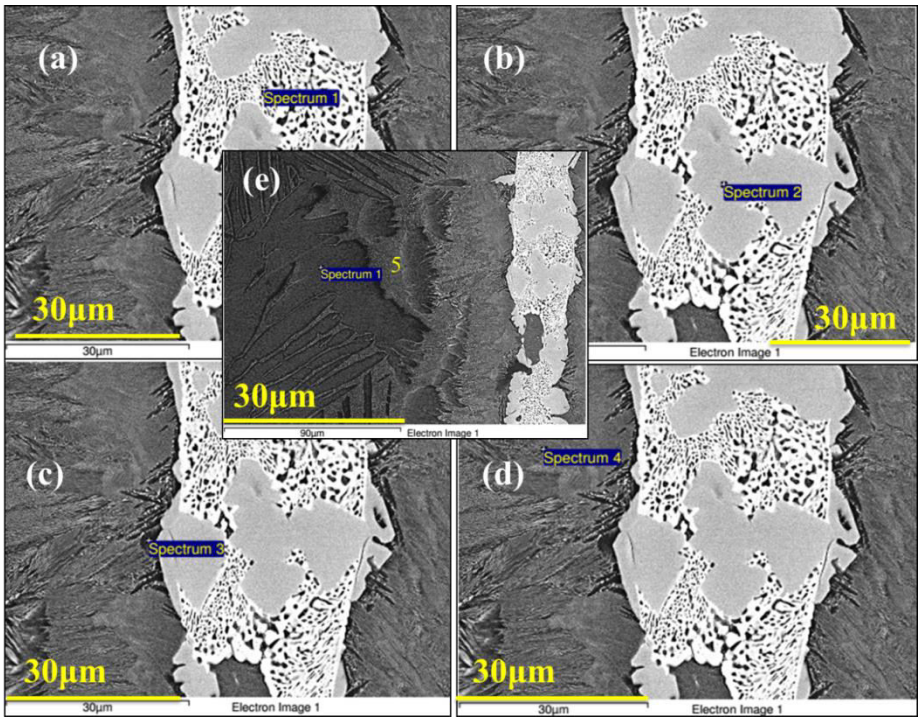


Fig 5.20 Further FESM study of the interface microstructures of Ti/ $Ti_{20}Zr_{20}Cu_{10}Ni_{50}$ /Ti composite joint brazed at 1006°C for 10 min: (a) Diffusion zone 1 (b) diffusion zone 2, (c) diffusion zone 3, (d) discontinuous reaction zone and (e) central zone.

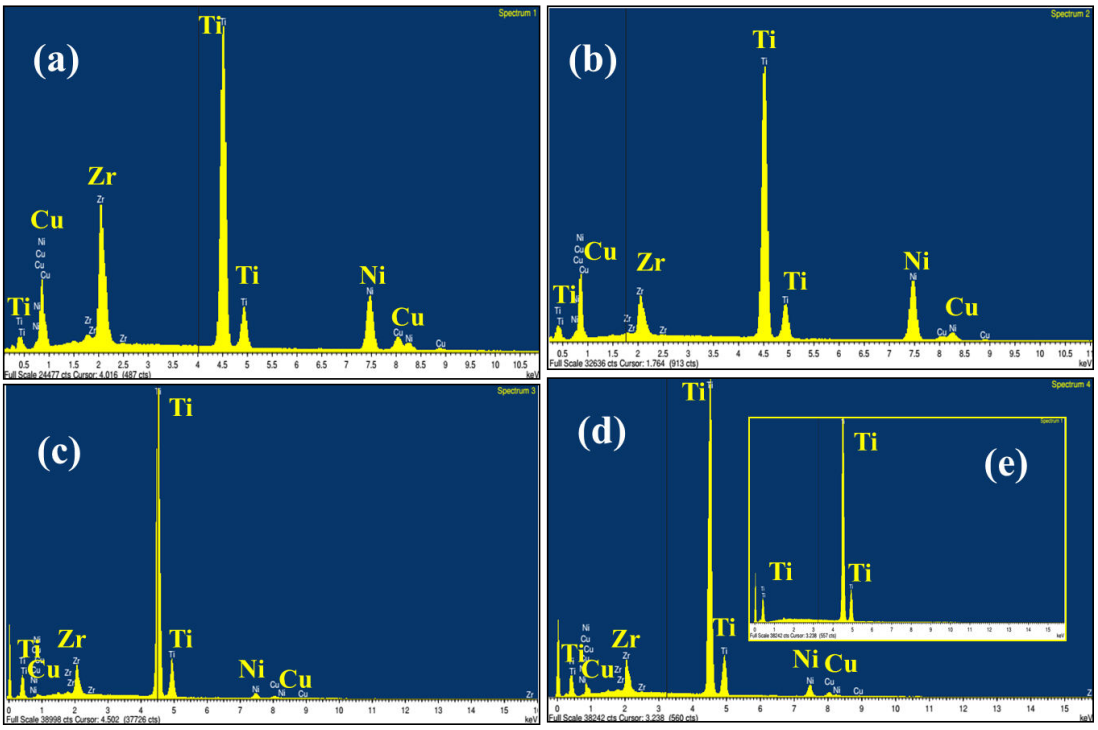


Fig 5.21 EDX spectra of the interface microstructures of Ti/$Ti_{20}Zr_{20}Cu_{10}Ni_{50}$/Ti composite joint brazed at 1006°C for 10 min: (a) Spectrum 1 collected from Diffusion zone 1 shown in Figure 5.20 (a), (b) Spectrum 2 collected from Diffusion zone 2 shown in Figure 5.21 (b), (c) Spectrum 3 collected from discontinuous reaction zone shown in Figure 5.21(c) and (d) Spectrum 4, 5 collected from central zone shown in Figure 5.21 (e).

Table 5.6 EDX analyses based elemental chemical composition analysis of interface microstructures of Ti/$Ti_{20}Zr_{20}Cu_{10}Ni_{50}$/Ticomposite brazing joint at 1004°C

| Area | Elements (at. %) | | | | |
|---|---|---|---|---|---|
| | Ti | Zr | Cu | Ni | Phases |
| Spectrum 1 | 56.69 | 16.50 | 5.86 | 20.95 | $NiTi_2$Ref[4] |
| Spectrum 2 | 60.91 | 6.37 | 2..16 | 30.57 | $Cu_2$(Ni, Zr) Ref[5] |
| Spectrum 3 | 89.55 | 5.51 | 1.58 | 3.36 | NiTiRef[4] |
| Spectrum 4 | 84.38 | 5.62 | 2.81 | 7.19 | α-Ti Ref[3] |
| Spectrum 5 | 100.00 | --- | --- | --- | Ti-rich |

**5.5 Conclusions**

The thermal and microstructural analyses for brazed joint samples of $Ti_{20}Zr_{20}Cu_{60-x}Ni_x$ (x=10, 20, 30, 40 and 50) metallic glasses with CP-Ti alloy were described in this Chapter. The DTA curve of the$Ti_{20}Zr_{20}Cu_{50}Ni_{10}$ metallic glass showed three peaks for first onset ($T_{m1}$), second onset ($T_{m1}$) and third onset ($T_{m1}$) melting points at 986, 1089 and 1117°C, respectively and similarly, three peaks found for first end set ($T_{m2}$), second end set ($T_{m2}$) and third end set ($T_{m2}$) melting points at 999, 1097 and 1127°C, respectively. The DTA curve of the$Ti_{20}Zr_{20}Cu_{40}Ni_{20}$ metallic glass showed one peak found for first onset ($T_{m1}$) melting point at 960°C and similarly one peak for first end set ($T_{m2}$) melting point at 975°C. The DTA curve of the$Ti_{20}Zr_{20}Cu_{30}Ni_{30}$ metallic glass showed one peak found first onset ($T_{m1}$) melting point at 989°C and similarly one peak found first end set ($T_{m2}$) melting point at 1002°C. The DTA curve of the$Ti_{20}Zr_{20}Cu_{20}Ni_{40}$ metallic glass showed one peak found for first onset ($T_{m1}$) melting point at 990°C and similarly one peak found for first end set ($T_{m2}$), melting point at 1010°C. The DTA curve of the$Ti_{20}Zr_{20}Cu_{10}Ni_{50}$ metallic glass showed one peak found for first onset ($T_{m1}$) melting point at 1000°C and similarly one peak for first end set ($T_{m2}$) melting points at 1011°C.

CP-Ti alloy pieces were respectively braze joined using metallic glass ribbon fillers of compositions (a) $Ti_{20}Zr_{20}Cu_{50}Ni_{10}$, (b) $Ti_{20}Zr_{20}Cu_{40}Ni_{20}$, (c) $Ti_{20}Zr_{20}Cu_{30}Ni_{30}$, (d) $Ti_{20}Zr_{20}Cu_{20}Ni_{40}$, and (e) $Ti_{20}Zr_{20}Cu_{10}Ni_{50}$ at 990, 967, 995, 1004 and 1006$^{o}$C for a period of 10 min. Based on extensive studies of FESEM, EDX line scans, EDX spectrum analysis and elemental X-ray mapping by EDX it was found that depending on the combination of filler composition, brazing condition and cooling cycle of the brazing processes the corresponding joints were characterized by microstructure formed

by fine lamellar eutectoids of (a) $(Ti,Zr)_2Cu$,Ti-rich, and α-Ti phases, (b) $NiTi_2$, $Ti_2Cu$ , α-Ti and Ti-rich phases, (c) $NiTi_2$, $Ti_2Cu$ , α-Ti and Ti-rich phases, (d) $NiTi_2$, $(Ti, Zr)_2Ni$, β(Ti, Zr) and Ti-rich phases and (e) $NiTi_2$, $Cu_2(Ni, Zr)$, NiTi ,α-Ti and Ti-rich phases in correspondence.

## References


1. Y. Zhao et al. Interfacial microstructure and mechanical properties of porous-Si3N4 ceramic and Ti-Al alloy joints vacuum brazed with Ag-Cu filler, Ceramics International 43 (2017) 9738–9745.
2. J. Cao, Xiangyu Dai, Jiaqi Liu, Xiaoqing Si, Jicai Feng, Relationship between microstructure and mechanical properties of TiAl/ Ti2AlNb joint brazed using Ti-27Co eutectic filler metal , Materials and Design 121 (2017) 176–184
3. Qiwen Qiu, Ying Wang, Zhenwen Yang, Xin Hu, Dongpo Wang, Microstructure and mechanical properties of TiAl alloy joints vacuum brazed with Ti–Zr–Ni–Cu brazing powder without and with Mo additive, Materials and Design 90 (2016) 650–659.
4. B.B. Medeiros et al. / Journal of Non-Crystalline Solids 425 (2015) 103–109.
5. M. Kazunari, I. Yuki, M. Hirotaka, and M. Hiroyuki: Scripta Mater, vol. 68, (2013), pp. 777–80.
6. X. L. Bian, G. Wang, K. C. Chan, J. L. Ren, Y. L. Gao, Appl. Phys. Lett. 103, 101907 (2013).
7. E. Ganjeh, H. Sarkhosh, M.E. Bajgholi, H. Khorsand, M.H. Ghaffari, Increasing Ti–6Al–4V brazed joint strength equal to the base metal by Ti and Zr amorphous filler alloys Materials characterization 71(2012)31-40.
8. Elrefaey A, Tillmann W. brazing of titanium to steel with different filler metals: analysis and comparison. J Mater Sci 45 (2010): 4332–8.

9. Lee JG, Choi YH, Lee JK, Lee GJ, Lee MK, Rhee CK. Low-temperature brazing of titanium by the application of a Zr–Ti–Ni–Cu–Be Bulk Metallic Glass (BMG) alloy as a filler. Intermetallics (2010); 18:70–3.

10. Y. Huang, Y.L. Chiu, J. Shen, J.J.J. Chen, J. Sun, Nanoindentation study of Ti-based metallic glasses, J. Alloys Compd. 479 (2009) 121–128.

11. Elrefaey A, Tillmann W. Correlation between microstructure, mechanical properties, and brazing temperature of steel to titanium joint. J Alloys Compd 487 (2009); 639–45.

12. N.K. Mukhopadhyay, A. Belger, P. Paufler, D.H. Kim, Nanoindentation studies on Cu–Ti–Zr–Ni–Si–Sn bulk metallic glasses, Mater. Sci. Eng. A 449–451 (2007) 954–957.

13. Y.J. Yang, F.W. Kang, D.W. Xing, J.F. Sun, Q.K. Shen, J. Shen, Formation and mechanical properties of bulk Cu–Ti–Zr–Ni metallic glasses with high glass forming ability, Trans. Nonferrous Met. Soc. China 17 (2007) 16–20.

14. Chang CT, Wu ZY, Shiue RK, Chang CS. Infrared brazing Ti–6Al–4V and SP-700 alloys using the Ti–20Zr–20Cu–20Nibraze alloy. Mater Lett (2007); 61:8425.

15. Materials Science International Team M. Ternary alloy systems: phase diagrams, crystallographic and thermodynamic data, V 11. Berlin, Germany: Springer; (2007).

16. Hong IT, Koo CH. Microstructural evolution and shears strength of brazing C103 and Ti–6Al–4V using Ti–20Cu–20Ni–20Zr (wt. %) filler metal. Int J Refract Met Hard Mater (2006); 24:247–52.

17. Doherty KJ, Tice JR, Szewczyk ST, Gilde GA. Titanium brazing for structures and survivability. Proceedings of the 3rdInternational Brazing and Soldering Conference; (2006). P. 268–73. San Antonio, Texas, USA.

18. N.K. Mukhopadhyay, P. Paufler, Micro- and nanoindentation techniques for a Mechanical characterization of materials, Int. Mater. Rev. 51 (2006) 209-245.

19. C.A. Schuh, T.G. Nieh, A survey of instrumented indentation studies on metallic glasses, J. Mater. Res. 19 (2004) 46–57.

20. W.C. Oliver, G.M. Pharr, Measurement of Hardness and Elastic Modulus by Instrumented Indentation: Advances in Understanding and Refinements to Methodology, J. Mater. Res. 19 (2004) 3-20.

21. Shiue RK, Wu SK, Chan CH. The interfacial reactions of infrared brazing Cu and Ti with two silver-based braze alloys.J Alloys Compd, 372, (2004); 148–57.

22. M. Calin, J. Eckert, L. Schultz, Improved mechanical behavior of Cu–Ti-based bulk metallic glass by in situ formation of nanoscale precipitates, Scr. Mater. 48 (2003) 653–658.

23. X.H. Lin, W.L. Johnson, Formation of Ti–Zr–Cu–Ni bulk metallic glasses, J. Appl. Phys. 78 (1995) 6514–6519.

24. H. Choi-Yim, R. Busch, W.L. Johnson, The effect of silicon on the glass forming ability of the Cu47Ti34Zr11Ni8 bulk metallic glass forming alloy during processing of composites, J. Appl. Phys. 83 (1998) 7993–7997.

25. M J Donachie. Titanium: a technical guide. 2 ed. USA: ASM; (2000).

26. Chang E, Chen CH. Low-melting-point titanium-base brazing alloys—part 2: characteristics of brazing Ti.21Ni–14Cu on Ti–6Al–4V substrate. JMEPEG (1997); 6:797–803.

27. Metals hand book, vol 3: alloy phase diagrams. ASM; (1992).

28. Schwartz MM. Brazing. 2 ed. USA: ASM; (2003).

29. Dieter GE. Mechanical metallurgy. 3 ed. USA: McGraw Hill; (2001).

30. Oliver W. C. and Pharr G. M., J. Mater. Res. 7 (1992) 1564.

31. JIS Z 3192. Methods for tension and shear tests for brazed joint; 1988.

32. Journal of Phase Equilibria and Diffusion, 35 (2014)2

33. Metallurgical and materials transactions A, 44A (2013)9.

34. Materials transactions Vol.49, No.6 (2008) Pp.1488.

# Chapter 6
# Mechanical Properties of Brazed Joints

## Introduction

The nanomechanical as well as the macro scale tensile strength properties of brazed joints are also discussed in this Chapter.

## 6.1 Nanoindentation for brazed samples

### 6.1.1 Nanohardness of Ti/$Ti_{20}Zr_{20}Cu_{50}Ni_{10}$/Ti joint brazed at 990°C for 10min.

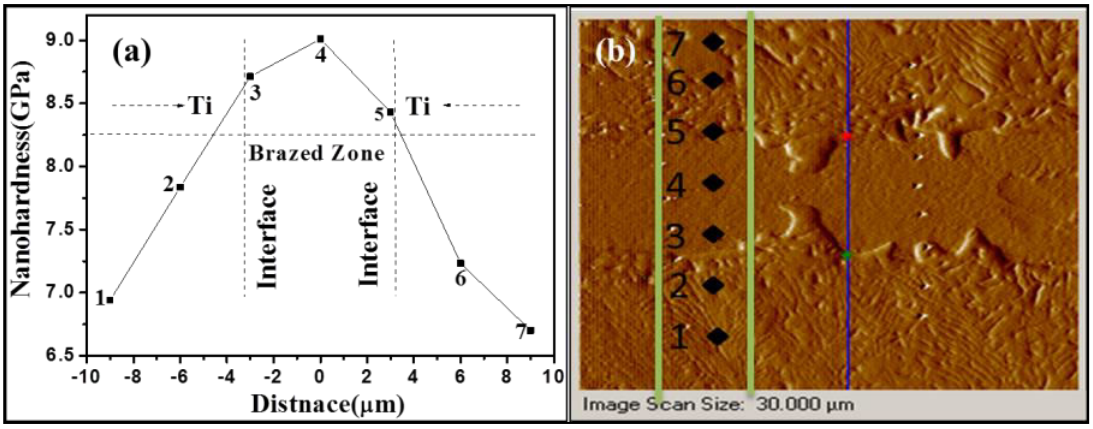


Fig.6.1 Nanohardness of Ti/$Ti_{20}Zr_{20}Cu_{50}Ni_{10}$/Ti joint brazed at 990°Cfor 10min: (a) Nanohardness profile as a function of distance from 10 μm on both sides of the microstructure through the brazed joint and (b) SPM images of the corresponding nanoindents at different regions of the microstructure of the brazed joint.

The appearance of a microstructure of $Ti_2Cu$ and $NiTi_2$ precipitations surrounded by $Ti_{20}Zr_{20}Cu_{50}Ni_{10}$ solid solution matrix was due to brazing at 990°C for 10 min. The corresponding nanohardness profile as a function of distance particularly from 10 μm on both sides of the microstructure during brazed joint and SPM images of the nanoindent at different regions of the microstructure of the brazed joint are indicated in Figs.6.1 (a) and (b), respectively. In Fig. 6.1 (b), the microstructure contained (Ti, $Zr)_2Cu$, $Ti_2Cu$ and $NiTi_2$ and Ti-rich portions marked as regions 3,4 and 5, respectively

[2-6]. However, the eutectoid phase rich portions are marked as regions 1, 2, 6 and 7 which are lying on outer side of the brazed joint.

Thus, the portions marked as regions 3, 4 and 5 in Figure 6.1(b) were inside the brazed joint. Out of these different regions the $Ti_2Cu$ and $NiTi_2$ intermetallic rich portion marked as region 4 had the highest nanohardness of 9 GPa, Fig. 6.1(a). The $(Ti, Zr)_2Cu$ rich portion marked as region 3 had the next highest nanohardness of about 8.7 GPa, as indicated in Fig. 6.1(a). The Ti-rich portion marked as region 5 had a nanohardness of about 8.2 GPa (see Fig.6.1a). Again, depending on the local eutectoid phase compositions as shown in Fig. 6.1(a); the nanohardness varied from as low as about 6.7 GPa in region 7 to as high as about 7.8 GPa in region 2.

### 6.1.2 Nanohardness of $Ti/Ti_{20}Zr_{20}Cu_{40}Ni_{20}/Ti$ joint brazed at 967 °C for 10 min

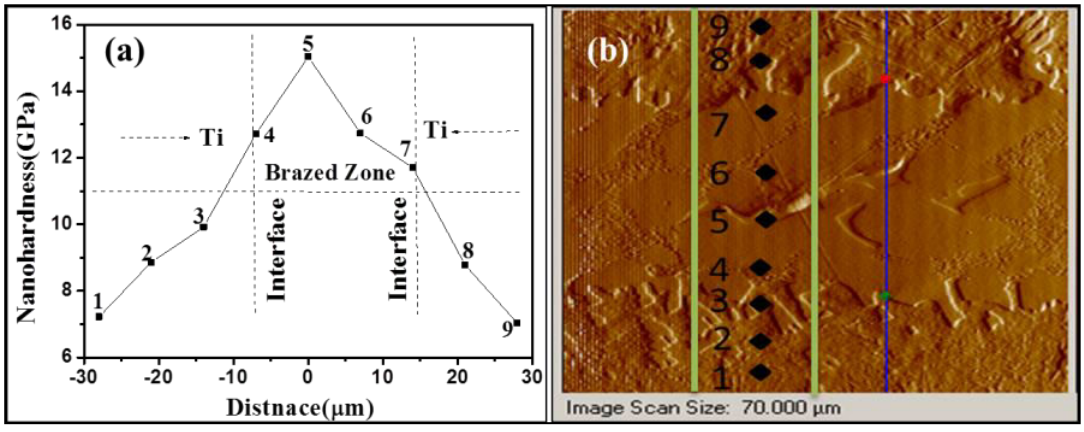


Fig.6.2 Nanohardness of $Ti/Ti_{20}Zr_{20}Cu_{40}Ni_{20}/Ti$ joint brazed at 967°Cfor 10min: (a) Nanohardness profile as a function of distance from 10 μm on both sides of the microstructure through the brazed joint and (b) SPM images of the corresponding nanoindent at different regions of the microstructure of the brazed joint.

In Fig. 6.2 (b), the microstructure obtained α-Ti, $Ti_2Cu$, $NiTi_2$ and β-Ti marked as regions 3, 4, (5 and 6) and 7, respectively, whereas Ti-rich portions are marked as regions 1,2, 8 and 9 lying outside the brazed joint. Thus, the portions marked as regions 3, 4 and 5 in Fig. 6.2 (b) were inside the brazed joint. Out of these different regions the $Ti_2Cu$ rich region 4 had the 3rd highest nanohardness of 12.6 GPa, the $NiTi_2$ rich region 5 had the highest nanohardness of 15 GPa, and the $Ti_2Cu$ rich region 6 had the 2nd highest nanohardness of 13.4 GPa. Further, the α-Ti rich region 3 had a slightly lower nanoharness of 10 GPa. Brazing developed a thin layer of β-Ti between the base metal and reaction layers. A slightly higher nanohardness of 11.8 GPa was recorded in the β-Ti-rich region 7. On the other hand, the Ti-rich regions 1, 2, 8 and 9 had much lower nanohardness of only about 6-8 GPa.

### 6.1.3 Nanohardness of $Ti/Ti_{20}Zr_{20}Cu_{30}Ni_{30}$ / Ti joint brazed at 995°C for 10min.

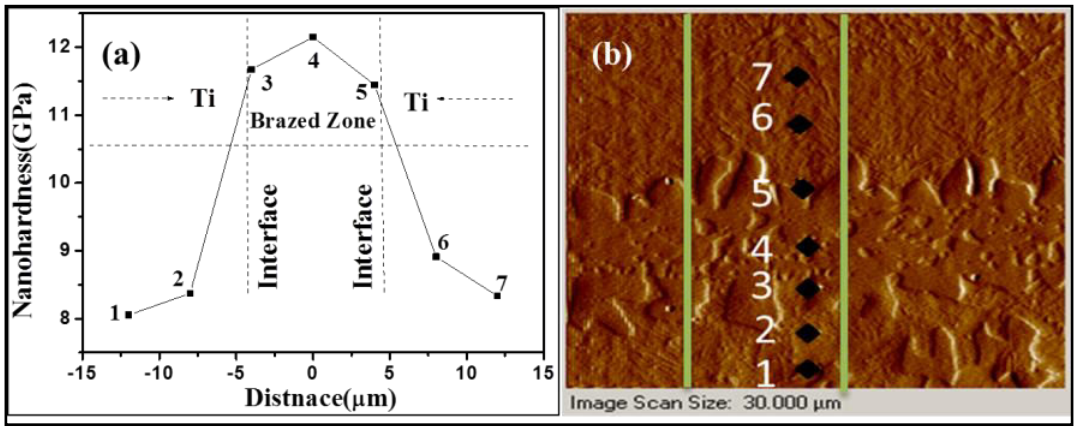


Fig.6.3 Nanohardness of $Ti/Ti_{20}Zr_{20}Cu_{30}Ni_{30}$/Ti joint brazed at 995°C for 10min: (a) Nanohardness profile as a function of distance from 10 μm on both sides of the microstructure through the brazed joint and (b) SPM images of the corresponding nanoindents at different regions of the microstructure of the brazed joint.

Similarly, in Fig 6.3 (b), the microstructure contained the Ti-rich portions are marked as regions 1, 2, 6 and 7 lying outside the brazing zones, the α-Ti, $Ti_2Cu$ and $(Ti,Zr)_2Ni$ rich portions are marked as regions 3,4 and 5, respectively, which are inside the brazing zones. Out of these different regions the $Ti_2Cu$ rich region 4 had the highest nanohardness of 12 GPa, the $(Ti,Zr)_2Ni$ rich region 5 had the 2nd highest nanohardness of 11.4 GPa, and the a-Ti rich region 3 had the 2nd highest nanohardness of 11GPa. On the other hand, the Ti rich regions 1, 2, 6 and 7 had much lower nanohardness of only about 8 GPa.

### 6.1.4 Nanohardness of $Ti/Ti_{20}Zr_{20}Cu_{20}Ni_{40}$ / Ti joint brazed at 1004°C for10min.

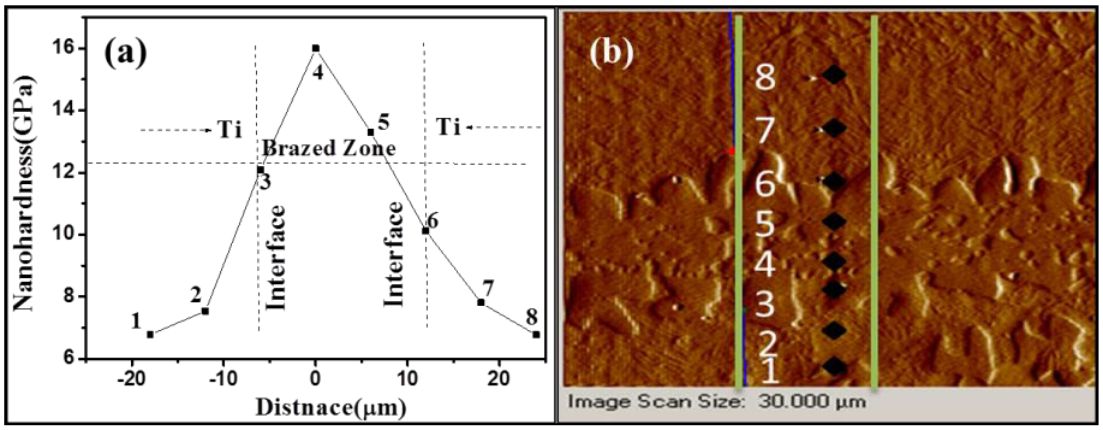


Fig.6.4 Nanohardness of $Ti/Ti_{20}Zr_{20}Cu_{20}Ni_{40}/Ti$ joint brazed at 1004°C for 10min: (a) Nanohardness profile as a function of distance from 10 μm on both sides of the microstructure through the brazed joint and (b) SPM images of the corresponding nanoindents at different regions of the microstructure of the brazed joint.

In Fig 6.4 (b), the microstructure contained the Ti-rich portions are marked as regions 1, 2, 7 and 8 lying outside the brazing zones, the β (Ti, Zr), $NiTi_2$ and $(Ti, Zr)_2Ni$ rich portions are marked as regions 3,4 and 5, respectively, which are inside the brazing zones, while the Ti-rich region 6 is outside the brazing zone. Out of these different

regions the $NiTi_2$ rich region 4 had the highest nanohardness of 16 GPa, the $(Ti, Zr)_2Ni$ rich region 5 had the 2nd highest nanohardness of 13GPa, and the β (Ti, Zr) rich region 3 had the 3rd highest nanohardness of 12 GPa. On the other hand, the Ti rich regions 1, 2, 6 and 7 had much lower nanohardness of only about 6-7 GPa.

### 6.1.5 Nanohardness of $Ti/Ti_{20}Zr_{20}Cu_{10}Ni_{50}/Ti$ joint brazed at 1006°C for 10min.

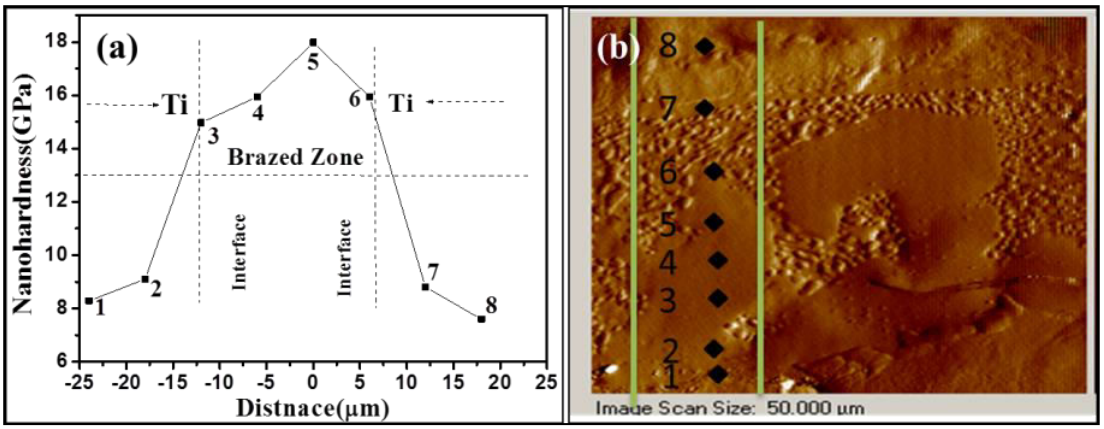


Fig.6.5 Nanohardness of $Ti/Ti_{20}Zr_{20}Cu_{10}Ni_{50}/Ti$ joint brazed at 1006°C for 10 min: (a) Nanohardness profile as a function of distance from 10 μm on both sides of the microstructure through the brazed joint and (b) SPM images of the corresponding nanoindents at different regions of the microstructure of the brazed joint.

The similar trend has also been observed in $Ti/Ti_{20}Zr_{20}Cu_{10}Ni_{50}/Ti$ brazed joint metallic glass (Fig 6.5 (b)). In Fig 6.5 (b), the microstructures of the Ti rich portions are marked as regions 1, 2, 7 and 8 lying outside the brazing zone, the α–Ti, NiTi, $NiTi_2$ and $Cu_2(Ni, Zr)$ rich portions are marked as regions 3, 4, 5 and 6, respectively, which are inside the brazing zones. Out of these different regions the $NiTi_2$ rich region 5 had the highest nanohardness of 17 GPa, the $Cu_2(Ni,Zr)$ rich region 6 and the NiTi rich region 4 had the 2nd highest nanohardness of 15.8 GPa, and the α-Ti rich region 3 had the 3rd

highest nanohardness of 14.8 GPa. On the other hand, the Ti rich regions 1, 2, 7 and 8 had much lower nanohardness of only about 7-8 GPa [7-12].

### 6.2 Butt-lap joints tensile strength characterization

The 1.5 mm thick commercial pure Ti was used in this work, which has been transformed to β-phase after furnace cooling from 990$^{o}$C. The chemical composition (wt.%) of the base metal *viz*., C, O, Fe, N, H and Ti are 0.1, 0.2, 0.08, 0.15, 0.01 and balance amount, respectively [ 13-15]. The parent metal pieces were polished first with SiC papers up to 600-1200 grade and cleaned subsequently by an ultrasonic bath with acetone for 20 min at 50$^{o}$C prior to insertion in the furnace for brazing. After cleaning the brazing foils with acetone and afterwards they were sandwiched between the merging areas of the native metals. The first lap shear metal specimen of 8.16 and 14.18 mm width and length, respectively with decreased cross-section was brazed with 4.5 mm overlapping using wire cutting machine (electrical discharge machine EDM, model JISZ 3192 [1] ). Furthermore, the microstructure fractured analysis has been made during butt-lap joint which was cut into 10 mm x 15 mm.

### 6.2.1 Tensile Strength of Ti/$Ti_{20}Zr_{20}Cu_{50}Ni_{10}$/Ti joint brazed at 990°C for 10min.

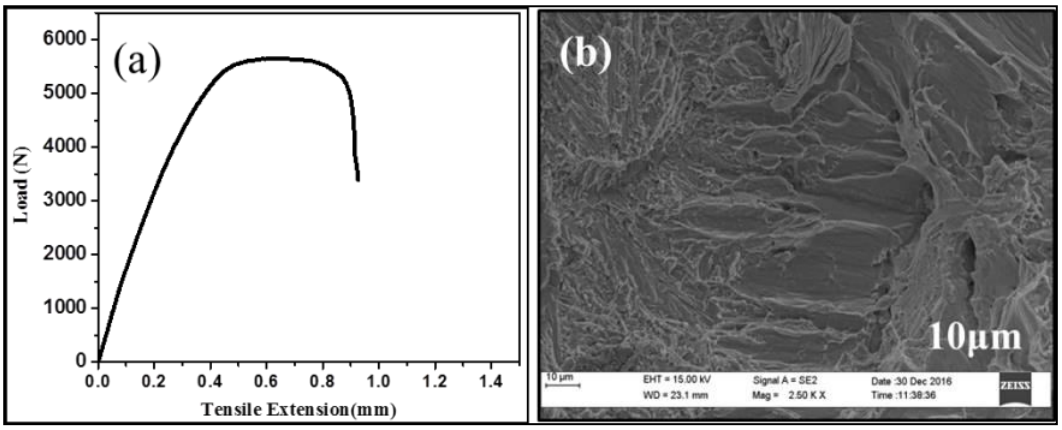


Fig.6.6 Tensile test data of Ti/$Ti_{20}Zr_{20}Cu_{50}Ni_{10}$/Ti brazed joint at 990°C for a period of 10 min: (a) Load versus tensile extension plot and (b) FESEM image of fracture surface. Each test is conducted two times under identical test conditions.

During the tensile strength experiment of the Ti/$Ti_{20}Zr_{20}Cu_{50}Ni_{10}$/Ti brazed joint at 990°C for 10 min in butt-lap joint, the load against tensile extension plot and FESEM fracture surface image are indicated in Figs. 6.6 (a) and (b), respectively [16]. True stress at maximum load was only 50.97 MPa because it had a low yield strength corresponding to a low nanohardness of 9 GPa. This was due to the microstructure of $Ti_2Cu$ and $NiTi_2$ complex formation around the solid solution matrix of $Ti_{20}Zr_{20}Cu_{50}Ni_{10}$. Fig.6.6 (b) demonstrates a typical brittle rupture, which was characterized by the cleavage of high facets with river markings. Similar observations were made in all the metallic glasses (Figs 6.7b-6.10b).

Similarly, the behaviours of tensile extension plot and FESEM images of Ti/$Ti_{20}Zr_{20}Cu_{40}Ni_{20}$/Ti, Ti/$Ti_{20}Zr_{20}Cu_{30}Ni_{30}$/Ti, Ti/$Ti_{20}Zr_{20}Cu_{20}Ni_{40}$/Ti and Ti/$Ti_{20}Zr_{20}Cu_{10}Ni_{50}$/Ti brazed joints at different temperatures for a period of 10 min are given in Figs. 6.7-6.10, respectively. The corresponding true stresses at maximum load

for the above brazing joints are given in Table 6.1. The corresponding higher yield strengths are due to higher nanohardness, which are 9, 15, 12, 16 and 17 GPa for the five brazed joint metallic glasses mentioned above. The microstructures are due to the complex formation around above mentioned brazed joint glasses of the solid solution matrices. It is interesting to note that among five different glasses, the $Ti_{20}Zr_{20}Cu_{10}Ni_{50}$ has the highest yield strength of 17 GPa, which is mainly due to $NiTi_2$ phase [19].

Table 6.1 The tensile test results for brazed joint samples

| Composition | Brazed Temp.(°C) | Maximum Load (N) | True stress at Maximum Load (MPa) |
|---|---|---|---|
| $Ti_{20}$ $Zr_{20}$ $Cu_{50}$ $Ni_{10}$ | 990 | 5.6 | 50.97±0.17 |
| $Ti_{20}$ $Zr_{20}$ $Cu_{40}$ $Ni_{20}$ | 967 | 6.4 | 63.84±0.95 |
| $Ti_{20}$ $Zr_{20}$ $Cu_{30}$ $Ni_{30}$ | 995 | 6.6 | 60.01±0.75 |
| $Ti_{20}$ $Zr_{20}$ $Cu_{20}$ $Ni_{40}$ | 1004 | 5.3 | 50.61±0.15 |
| $Ti_{20}$ $Zr_{20}$ $Cu_{10}$ $Ni_{50}$ | 1006 | 6.3 | 65.87±0.98 |

### 6.2.2 Tensile Strength of Ti/$Ti_{20}Zr_{20}Cu_{40}Ni_{20}$/Ti joint brazed at 967°Cfor 10min

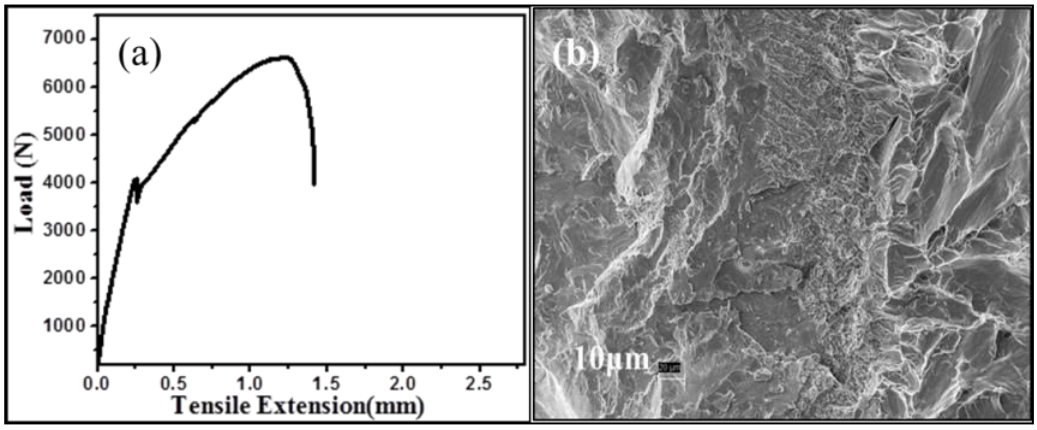


Fig.6.7 Tensile test data of Ti/$Ti_{20}Zr_{20}Cu_{40}Ni_{20}$/Ti brazed joint at 967°C for a period of 10 min: (a) Load versus tensile extension plot and (b) FESEM image of fracture surface. Each test is conducted two times under identical test conditions.

### 6.2.3 Tensile Strength of Ti/$Ti_{20}Zr_{20}Cu_{30}Ni_{30}$/Ti joint brazed at 995°Cfor 10min

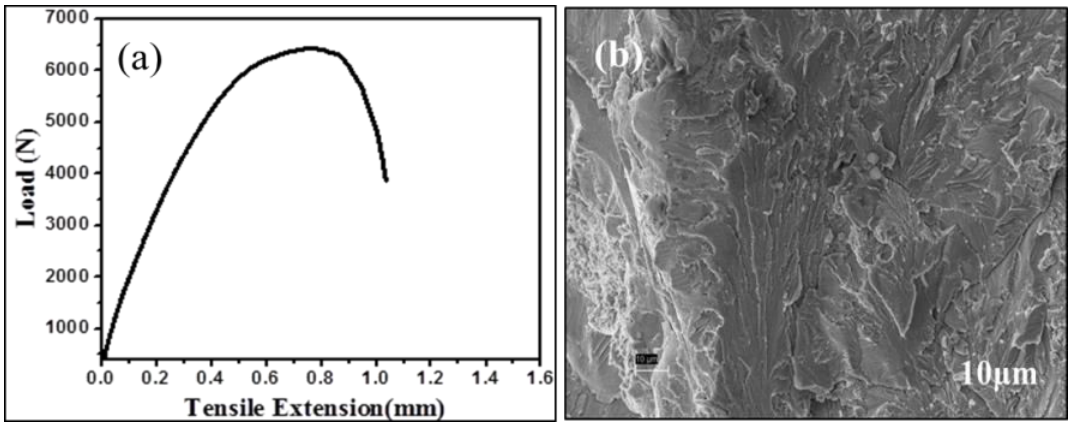


Fig.6.8 Tensile test data of Ti/$Ti_{20}Zr_{20}Cu_{30}Ni_{30}$/Ti brazed joint at 995°C for a period of 10 min: (a) Load versus tensile extension plot and (b) FESEM image of fracture surface. Each test is conducted two times under identical test conditions.

### 6.2.4 Tensile Strength of Ti/$Ti_{20}Zr_{20}Cu_{20}Ni_{40}$/Ti joint brazed at 1004°Cfor 10min.

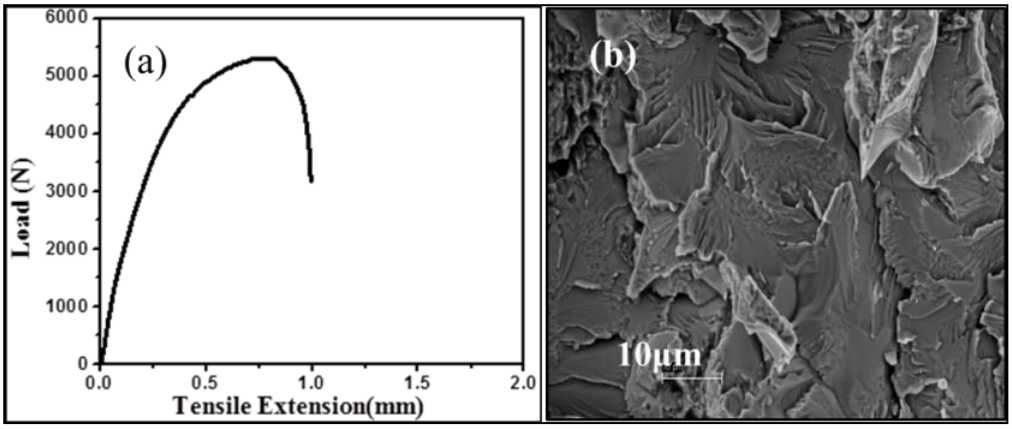


Fig.6.9 Tensile test data of Ti/$Ti_{20}Zr_{20}Cu_{20}Ni_{40}$/Ti brazed joint at 1004°C for a period of 10 min: (a) Load versus tensile extension plot and (b) FESEM image of fracture surface. Each test is conducted two times under identical test conditions.

### 6.2.5 Tensile Strength of Ti/$Ti_{20}Zr_{20}Cu_{10}Ni_{50}$/Ti joint brazed at 1006°Cfor 10min.

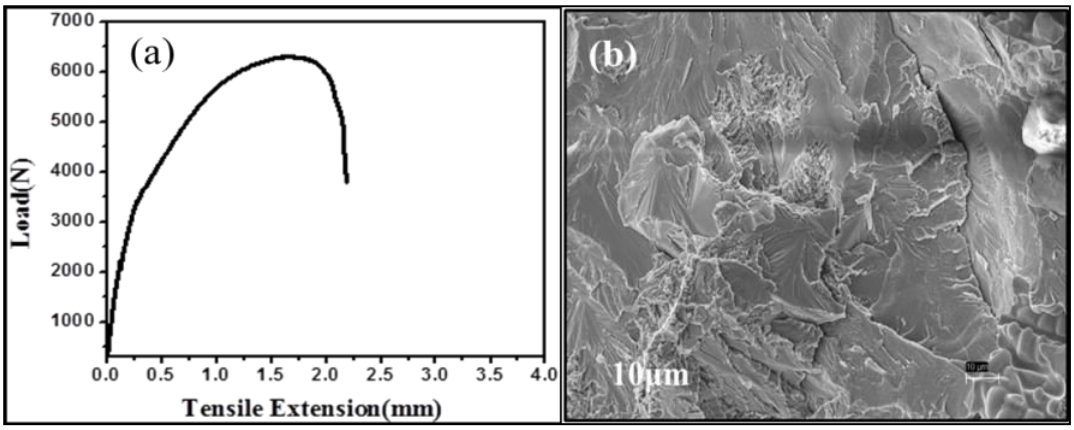


Fig.6.10 Tensile test data of Ti/$Ti_{20}Zr_{20}Cu_{10}Ni_{50}$/Ti brazed joint at 1006°C for a period of 10 min: (a) Load versus tensile extension plot and (b) FESEM image of fracture surface. Each test is conducted two times under identical test conditions.

The cracks were developed due to the brittle nature of the $Ti_2Cu$ which shown by arrows in Figs 6.6b-6.10b. Fig.6.2b and 6.4b showed that quasi-cleavage fracture appearance in the Ti-Ti matrix phase followed by brittle $Ti_2Cu$ phase. Fig. 6.10 (b) indicated the quasi-cleavage major fractures of Ti included in the $Ti_2Cu$ phase. Therefore, the fracture owing to quasi-cleavage is beneficial for the strength of the joint. The appearance of brittle fracture caused upon reduction of the strength of a bonded joint due to the formation of the intermetallic compound at the Ti/braze interface [17, 18, 19]. The main reasons for the crack initiation are the formation of the hard and brittle intermetallic compounds *viz*., $Ti_2Cu$, $Ti_2Ni$ and/or $Cu_2$ (Ni, Zr) at Ti interface. Generally, the propagation of the cracks prefer at the brittle intermetallic compounds, which can spread easily through them during application of stress in tensile experiment. The reduction of the strength of the joints and fracture behaviour upon propagation of the crack, which shows the morphological cleavage including

facets characteristics. The measure of tensile strength and fracture behaviours demonstrated the appearance of the $NiTi_2/Ti_2Cu/NiTi/Cu_2$ (Ni, Zr)/ $(Ti, Zr)_2Ni$ and β(Ti, Zr) phases in the braze joints, which were detrimental and hence, they must be ignored in order to obtain a sound joint.

## 6.3 Conclusions

The nanomechanicals analysis for brazed samples of $Ti_{20}Zr_{20}Cu_{60-x-}Ni_x$ (x=10, 20, 30, 40 and 50) metallic glasses with CP-Ti alloy were done in this Chapter. CP-Ti alloy pieces were respectively braze joined using metallic glass ribbon fillers of compositions (a) $Ti_{20}Zr_{20}Cu_{50}Ni_{10}$, (b) $Ti_{20}Zr_{20}Cu_{40}Ni_{20}$, (c) $Ti_{20}Zr_{20}Cu_{30}Ni_{30}$, (d) $Ti_{20}Zr_{20}Cu_{20}Ni_{40}$, and (e) $Ti_{20}Zr_{20}Cu_{10}Ni_{50}$ at 990, 967,995, 1004 and 1006$^oC$ for a period of 10 min. (a) $(Ti, Zr)_2Cu$,Ti-rich, and α-Ti phases, (b) $NiTi_2$, $Ti_2Cu$ , α-Ti and Ti-rich phases, (c) $NiTi_2$, $Ti_2Cu$ , α-Ti and Ti-rich phases, (d) $NiTi_2$, $(Ti, Zr)_2Ni$ ,β (Ti, Zr) and Ti-rich phases and (e) $NiTi_2$, $Cu_2(Ni, Zr)$, NiTi ,α-Ti and Ti-rich phases in correspondence.

## References


1. JIS Z 3192. Methods for tension and shear tests for brazed joint; 1988.
2. Q. Qiu et al. / Materials and Design 90 (2016) 650–659
3. E. Ganjeh et al. / Materials characterization 71(2012)31-40.
4. MjDonachie. Titanium: a technical guide. 2 ed. USA: ASM; 2000.
5. Lutjering G, Williams JC. Titanium. 2 ed. Berlin: Springer; 2007.
6. Chang CT, Wu ZY, Shiue RK, Chang CS. Infrared brazingTi–6Al–4V and SP-700 alloys using the Ti–20Zr–20Cu–20Nibraze alloy. Mater Lett 2007;61: 8425.
7. Hong IT, Koo CH. Microstructural evolution and shearstrength of brazing C103 and Ti–6Al–4V usingTi–20Cu–20Ni–20Zr (wt.%) filler metal. Int J Refract Met Hard Mater 2006; 24:247–52.
8. Chang E, Chen CH. Low-melting-point titanium-base brazingalloys—part 2: characteristics of brazing Ti.21Ni–14Cu onTi–6Al–4V substrate. JMEPEG 1997; 6 :797–803.
9. Doherty KJ, Tice JR, Szewczyk ST, Gilde GA. Titanium brazingfor structures and survivability. Proceedings of the 3rdInternational Brazing and Soldering Conference; 2006. P. 268–73. San Antonio, Texas, USA.
10. Metals hand book, vol 3: alloy phase diagrams. ASM; 1992.
11. Schwartz MM. Brazing. 2 ed. USA: ASM; 2003.
12. Lee JG, Choi YH, Lee JK, Lee GJ, Lee MK, Rhee CK.Low-temperature brazing of titanium by the application of aZr–Ti–Ni–Cu–Be Bulk Metallic Glass (BMG) alloy as a filler. Intermetallics (2010);18:70–3.
13. Dieter GE. Mechanical metallurgy. 3 ed. USA: McGraw Hill; 2001.
14. Materials Science International Team M. Ternary alloysystems: phase diagrams, crystallographic andthermodynamic data, volume 11. Berlin, Germany: Springer; 2007.

15. Shiue RK, Wu SK, Chan CH. The interfacial reactions ofinfrared brazing Cu and Ti with two silver-based braze alloys.J Alloys Compd, 372, (2004);:148–57.
16. Elrefaey A, Tillmann W. Correlation between microstructure, mechanical properties, and brazing temperature of steel totitanium joint. J Alloys Compd 487 (2009); 639–45.
17. Elrefaey A, Tillmann W. brazing of titanium to steel withdifferent filler metals: analysis and comparison. J Mater Sci 45 (2010): 4332–8.
18. M. Kazunari, I. Yuki, M. Hirotaka, and M. Hiroyuki: Scripta Mater, vol. 68, (2013), pp. 777–80.
19. Y. Zhao et al. Interfacial microstructure and mechanical properties of porous-$Si_3N_4$ ceramic and TiAl alloy joints vacuum brazed with AgCu filler, Ceramics International 43 (2017) 9738–9745

# Chapter 7
# Summary and Conclusions

The work was devoted to understand the "microstructural, mechanical, thermal and physical properties correlation in Ti-alloy brazed joint with Ti-Zr-Cu-Ni metallic glasses". Important inferences from the investigation are the following: As an outcome of the thesis work exists in different kind of glassy of metals. Not only the improvement of the glass forming ability take place, but also the thermal stability of Ni-based alloys enhanced, which is more advantageous in different applications. Interestingly, the addition of Ni improves the super cooled region and thereby thermal stability. In this thesis, the structural changes in metallic glasses upon devitrification, element addition and deformation were characterized by using DSC-DTA, XRD, FESEM and TEM techniques. Moreover, the compression test and Nanoindentation techniques were employed in order to understand the influence of the structural modifications on the mechanical and electrical behaviours. Based on the origin of these structural changes and brazing studies in metallic glasses, the results and discussion section was splitted into four main chapters (Chapters 3-6). For the sake of simplicity, the major conclusions are given below:

- Structural properties of the following metallic glasses were investigated: $Ti_{20}Zr_{20}Cu_{60-x}Ni_x$ (x= 10,20,30,40 and 50) alloy, the phase transformation kinetics of the $Ti_{20-}Zr_{20-}Cu_{60-x-}Ni_x$ (x= 10,20,30,40 and 50) metallic glasses have been performed by using various theoretical models and the following conclusions has been obtained.

- All the metallic glasses in the present investigation (except $Ti_{20}Zr_{20}Cu_{50}Ni_{10}$ glass) show a single crystallization peak, which substantiates the homogeneous behaviour of the metallic glasses.

- The $Ti_{20}Zr_{20}Cu_{50}Ni_{10}$ glass shows three crystallization peaks, which correspond two phases, which was due to micro-heterogeneous behaviour. Using Kissinger, Augis-Bennett and Ozawa method, the activation energy ($E_c$) for the first crystallization was determined. The results of XRD show that all the metallic glassy samples are amorphous in nature.

- FESEM has been used to study surface topography of the $Ti_{20}Zr_{20}Cu_{60-x}Ni_x$ (x= 10, 20, 30, 40 and 50) metallic glasses. All the metallic glasses show amorphous behaviour. The corresponding EDX data along with the typical elemental composition are given in Figs. 3.11(b)-3.15(b).
- The AFM images were taken in order to understand the actual topography of the surface of the metallic glasses to look at particularly roughness as well as surface topography of both shiny and dull sides of the metallic glass ribbons.
- The annealed X-rd for the different metallic glasses annealed for a period of 30 min are shown in Figs. 3.17-3.21 where the following crystalline phases are appeared: $Ni_4Ti_3$, $Cu_{51}Zr_{14}$, $Ni_2Ti$ and $NiTi_2$ in $Ti_{20}Zr_{20}Cu_{50}Ni_{10}$ metallic glass ribbon (annealed at 753 K); $NiTi_2$, NiTi, $Ni_4Ti_3$, $CuNi_2Ti$, $Ni_2Ti$ and $Cu_8Zr_3$in the $Ti_{20}Zr_{20}Cu_{40}Ni_{20}$ metallic glass ribbon (annealed at 756K); NiTi, $NiTi_2$, $Ni_4Ti_3$, $CuNi_2Ti$, and $Ni_2Ti$, $NiTi_{0.8}Zr_{0.2}$ in the $Ti_{20}Zr_{20}Cu_{30}Ni_{30}$ metallic glass ribbon (annealed at 758K); NiTi, $NiTi_2$, $Ni_2Ti$, $Cu_8Zr_3$, $Ni_4Ti_3$, $CuNi_2Ti$, $Ni_2Ti$, and $NiTi_{0.8}Zr_{0.2}$ in the $Ti_{20}Zr_{20}Cu_{20}Ni_{40}$ metallic glass ribbon (annealed at 778K)

and $NiTi_2$, $Ni_2Ti$, NiTi, $Ni_4Ti_3$, and $CuNi_2Ti$ in the $Ti_{20}Zr_{20}Cu_{10}Ni_{50}$ metallic glass ribbons (annealed at 783K), respectively.

- TEM Characterization have been done for the phase identification and microstructure analysis of the $Ti_{20}Zr_{20}Cu_{60-x}Ni_x$ (x= 10, 20, 30, 40 and 50) metallic glasses. Similarly, from TEM studies the following crystalline phases were observed for the various annealed metallic glasses for a period of 30 min: NiTi and $NiTi_2$ in the $Ti_{20}Zr_{20}Cu_{50}Ni_{10}$ metallic glass ribbon (annealed at 753 K): $Ni_2Ti$ and $NiTi_2$ in the $Ti_{20}Zr_{20}Cu_{40}Ni_{20}$ metallic glass ribbon (annealed at 756 K): NiTi in the $Ti_{20}Zr_{20}Cu_{30}Ni_{30}$ metallic glass ribbon (annealed at 758 K). $NiTi_2$ in the $Ti_{20}Zr_{20}Cu_{20}Ni_{40}$ metallic glass ribbon (annealed at 778 K) and $NiTi_2$ in the $Ti_{20}Zr_{20}Cu_{10}Ni_{50}$ metallic glass ribbon (annealed at 783 K), respectively.
- The uniform (homogeneous) distributions of the various nanocrystalline phases has been observed in the amorphous matrix. Existence of these nanocrystalline phases were also confirmed from both the XRD and the compositional analysis data obtained from the TEM studies.
- The typical representative plots of P-h obtained under 5000μN load for the following metallic glasses: (a) $Ti_{20}Zr_{20}Cu_{50}Ni_{10,}$ (b) $Ti_{20}Zr_{20}Cu_{40}Ni_{20,}$ (c) $Ti_{20}Zr_{20}Cu_{30}Ni_{30,}$ (d) $Ti_{20}Zr_{20}Cu_{20}Ni_{40,}$ and (e) $Ti_{20}Zr_{20}Cu_{10}Ni_{50.}$ To the best of our understanding, this is the first experimental work, which has been observed in the case of density and nanoindentation.
- The magnitudes of room temperature resistivity ($\rho_{RT}$) (i.e., 300K) were measured to be 61, 60, 62, 63 and 64 Ω-cm, respectively for $Ti_{20}Zr_{20}Cu_{50}Ni_{10}$, $Ti_{20}Zr_{20}Cu_{40}Ni_{20}$, $Ti_{20}Zr_{20}Cu_{30}Ni_{30}$, $Ti_{20}Zr_{20}Cu_{20}Ni_{40}$ and $Ti_{20}Zr_{20}Cu_{10}Ni_{50}$ metallic glass ribbons.

- The thermal and microstructural analyses for brazed joint samples of $Ti_{20}Zr_{20}Cu_{60-x}Ni_x$ (x=10, 20, 30, 40 and 50) metallic glasses with CP-Ti alloy were described in this Chapter. The DTA curve of the$Ti_{20}Zr_{20}Cu_{50}Ni_{10}$ metallic glass showed three peaks for first onset ($T_{m1}$), second onset ($T_{m1}$) and third onset ($T_{m1}$) melting points at 986, 1089 and 1117°C, respectively and similarly, three peaks found for first end set ($T_{m2}$), second end set ($T_{m2}$) and third end set ($T_{m2}$) melting points at 999, 1097 and 1127°C, respectively.
- The DTA curve of the$Ti_{20}Zr_{20}Cu_{40}Ni_{20}$ metallic glass showed one peak found for first onset ($T_{m1}$) melting point at 960°C and similarly one peak for first end set ($T_{m2}$) melting point at 975°C. The DTA curve of the$Ti_{20}Zr_{20}Cu_{30}Ni_{30}$ metallic glass showed one peak found first onset ($T_{m1}$) melting point at 989°C and similarly one peak found first end set ($T_{m2}$) melting point at 1002°C. The DTA curve of the$Ti_{20}Zr_{20}Cu_{20}Ni_{40}$ metallic glass showed one peak found for first onset ($T_{m1}$) melting point at 990°C and similarly one peak found for first end set ($T_{m2}$), melting point at 1010°C. The DTA curve of the$Ti_{20}Zr_{20}Cu_{10}Ni_{50}$ metallic glass showed one peak found for first onset ($T_{m1}$) melting point at 1000°C and similarly one peak for first end set ($T_{m2}$) melting points at 1011°C. CP-Ti alloy pieces were respectively braze joined using metallic glass ribbon fillers of compositions: (a)$Ti_{20}Zr_{20}Cu_{50}Ni_{10}$,(b)$Ti_{20}Zr_{20}Cu_{40}Ni_{20}$,(c)$Ti_{20}Zr_{20}Cu_{30}Ni_{30}$,(d)$Ti_{20}Zr_{20}Cu_{20}Ni_4$ and (e) $Ti_{20}Zr_{20}Cu_{10}Ni_{50}$ at 990 , 967, 995, 1004 and 1006$^oC$ for a period of 10 min.
- Based on extensive studies of FESEM, EDX line scans, EDX spectrum analysis and Elemental X-Ray Mapping by EDX it was found that depending on the combination of filler composition, brazing condition and cooling cycle of the

brazing processes the corresponding joints were characterized by microstructure formed by fine lamellar eutectoids of (a) $(Ti,Zr)_2Cu$,Ti-rich, and α-Ti phases, (b) $NiTi_2$, $Ti_2Cu$ , α-Ti and Ti-rich phases, (c) $NiTi_2$, $Ti_2Cu$ , α-Ti and Ti-rich phases, (d) $NiTi_2$, $(Ti, Zr)_2Ni$, β(Ti, Zr) and Ti-rich phases and (e) $NiTi_2$, $Cu_2(Ni, Zr)$, NiTi ,α-Ti and Ti-rich phases.

- The nanomechanical analyses for brazed joint samples of $Ti_{20}Zr_{20}Cu_{60-x-}Ni_x$ (x=10, 20, 30, 40 and 50) metallic glasses with commercial pure Ti-alloy were made. Commercial pure Ti-alloy pieces were respectively braze joined using metallic glass ribbon fillers of compositions for a period of 10 min: (a) $Ti_{20}Zr_{20}Cu_{50}Ni_{10}$, (b) $Ti_{20}Zr_{20}Cu_{40}Ni_{20}$, (c) $Ti_{20}Zr_{20}Cu_{30}Ni_{30}$, (d) $Ti_{20}Zr_{20}Cu_{20}Ni_{40}$ and (e) $Ti_{20}Zr_{20}Cu_{10}Ni_{50}$ at 990, 967, 995, 1004 and 1006$^oC$. (a) $(Ti, Zr)_2Cu$,Ti-rich, and α-Ti phases, (b) $NiTi_2$, $Ti_2Cu$ , α-Ti and Ti-rich phases, (c) $NiTi_2$, $Ti_2Cu$ , α-Ti and Ti-rich phases, (d) $NiTi_2$, $(Ti, Zr)_2Ni$ ,β(Ti, Zr) and Ti-rich phases and (e) $NiTi_2$, $Cu_2(Ni, Zr)$, NiTi ,α-Ti and Ti-rich phases in correspondence.

# Chapter 8
# Future scope of work

- The present work can be extended where the friction brazing of other different combinations with industrially relevant and potentiality in replacing the present alloys and metals. Ti and its alloys, composites and bulk metallic glasses for some examples, which can be attempted during post brazing and heat treatment upon friction welded samples.
- In the case of friction welding, the effect of cryogenic behaviour could be another choice in future research. The study on the effect of mechanical properties by utilising the pattern of interlayers of the following combinations would be more meaningful area of research: (a) compatibility with one of the metals, (b) compatibility with respect to both metals and (c) incompatibility in terms of both the metals.
- In most of the research works, the attention so far has not been paid on the effect of the rotational speed (which had been kept constant) on the mechanical properties Therefore, the effect of the rotational speed on the mechanical behaviour would be investigated.
- The effect of change in diameter on the friction welding ability can also be a viable option. Hence, this research can be explored by using various D/d ratios (where, D is the diameter of one metal and d is the diameter of other metal).
- As most of the research works have been made by using dissimilar metal combinations, and hence, the dissimilar polymers, ceramics or combined ceramic and polymer could be studied in future.